Modelling the turbulent transport of angular momentum in tokamak plasmas - A quasi-linear gyrokinetic approach

Pierre Cottier

Thèse de doctorat

Graduate School de l'Ecole Polytechnique

Spécialité : Physique des Plasmas

Modélisation du transport turbulent de moment angulaire dans les plasmas de tokamak

Une approche gyrocinétique quasi-linéaire

par

Pierre Cottier

Thèse soutenue publiquement le 28 octobre 2013 devant :

Dr. Clemente Angioni	Rapporteur
Dr. Clarisse Bourdelle	Responsable CEA
Dr. Yann Camenen	Examinateur
Dr. Özgür Gürcan	Examinateur
Dr. Pascale Hennequin	Directrice de thèse
Pr. Patrick Mora	Examinateur
Dr. Gary Staebler	Rapporteur

Acknowledgements

During the course of my PhD thesis work I have come across a lot of inspiring people. Surely, I am in their debt and without them the work presented hereafter would not have been carried out to its end.

First of all, I would like to acknowledge the invaluable contribution of my thesis supervisor, Clarisse Bourdelle. Her availability, pedagogy and great insight into plasma physics made this journey possible. I will obviously remember her generosity and her open mind, making the PhD student life easier to endure. I would like to thank my PhD director, Pascale Hennequin, for her attention to my work and the quality of her advices on more general matters. I am grateful to Clemente Angioni and Gary Staebler for having accepted to review the manuscript. Their enlighten comments and questions improved significantly its clarity, precision and completeness. I shall also acknowledge the major contributions of Özgür Gürcan and Yann Camenen whose reflexions and inputs on more technical aspects were either inspiring or decisive. I warmly thank Patrick Mora for having accepted to preside the jury of my defence and for the interest he manifested to this work.

I am thankful to Alain Bécoulet and Xavier Litaudon for having accepted me as a PhD student at the Research Institute for Magnetic Confinement Fusion (IRFM in French) in the Service for Heating and Confinement of the Plasma (SCCP also in French). I would like to acknowledge also the very pleasant working conditions I have encountered within the Group on Support to Experiments and Modelling (GSEM) headed by Frédéric Imbeaux.

I wish to acknowledge some very fruitful discussions and collaborations especially with Jonathan Citrin, Francis Casson, Xavier Garbet and Yanick Sarazin.

I also wish to acknowledge all PhD students, post-doctorate fellows and researchers with whom I add a lot of different chats on very different topics. Among them I would like to cite (in alphabetical order): Les deux Antoine, Dany, Didier, François, Grégoire, Guilhem,

Jérémie, Manu, Mélanie, Nico, Rémi, Sophie, Stéphanie, Thimothée, Thomas, Vanessa and Yue.

I also had the chance to participate in the organisation of Cadarache PhD student association. It was a nice complement to the scientific part of the PhD work. I am particularly grateful to Adrien, Agathe, Bertrand, Gaëlle, Gigi, Julien, Lise, Névénick, Nicolas, Simon and Vincent for all the work put together and the beautiful moments shared together.

In addition to those recent and invaluable connections, older influences (in my history not theiri were decisive in the choices that brought me here. Among them and at the top lie my parents, my brother, some great teachers (Maîtres Patelin et Vignal, M. Paul Roux, Prof. Philippe Pernod and Christophe Laux) and Patrice et Josiane.

Merci à tous et bonne lecture.

Pierre

Contents

1

Controlling nuclear fusion for cleaner energy

1.1 The global energetic context

Over the past two centuries, human kind managed to improve his standard of living like never before in his history in such a short time [Lucas, 2004]. This was made possible by the unfolding of modern science which led – among other things – to the development of modern medicine and the industrial revolution. But this has a cost in term a human footprint especially from the energetic point of view.

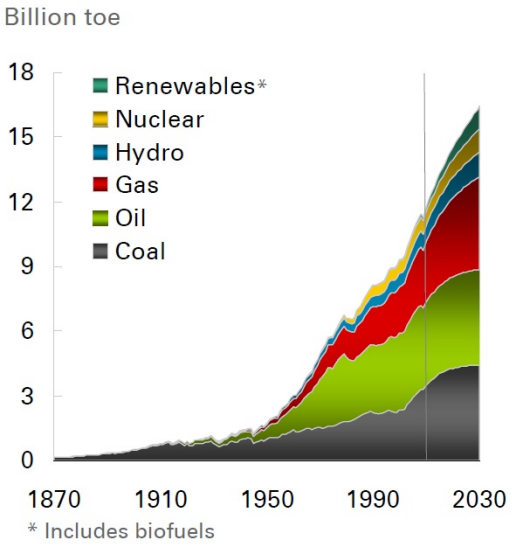

Figure 1.1: Evolution of the global energy consumption between 1870 and 2010 and forecast up to 2030. Adapted from [BP, 2013a]

As shown on Figure 1.1 from BP's Statistical Review of World Energy [BP, 2013a], the global energy consumption went from $\sim 3.10^{18}$ J ($\sim$ 0.1 billion tonnes equivalent oil (TOE)) in 1870 to more than 500.10^{18} J (more than 10 billion TOE) in 2010. Energy consumption has been stabilized in the past few years in most of the so-called developed countries. On the contrary, developing countries are increasing their demand in energy, supporting the growth of the energy consumption worldwide. In recent studies [Brown et al., 2011], it has been shown that raising the global average standard of living to that of the current US one would imply to multiple the global energy use 5 times, without taking into account any foreseeable population growth. Indeed, a strong correlation between gross domestic product (GDP) per capita and energy consumption per capita with a 0.76 exponent is shown in Brown et al. [2011]. Based on this observation, an analogy with animal metabolism is drawn in this paper: for animals, the metabolic rate increases with the body mass with a $^3/_4$ exponent factor. This means that considerable amount of energy have to be found to sustain a global improvement of the standard of living.

Up to now, the energy humankind consumes has been extracted mostly from oil, coal and natural gas. But using this kind of resources raises two major issues. First, the available quantities are limited. Conventional oil resources are estimated to last 50 years, gas resources 60 years and coal approximately 150 years with the current energy mix [BP, 2013b]. Secondly, burning these resources produces a significant amount of greenhouse gases. The symbolic milestone of 400 ppm of CO_2 was surpassed at the Mauna Loa Observatory in Hawaii in early May 2013. As displayed on Figure 1.2, this value is twice above the mean value of CO_2 atmospheric concentration over 800,000 years. Moreover, Earth experienced an over 100 ppm increase of its CO_2 atmospheric concentration over the last two centuries. Such a rapid and large rise was not seen for at least 800,000 years and is likely caused by human activities [Monastersky, 2013]. The concentration values reached in 2013 are widely acknowledged to be responsible for a substantial climate deregulation [Ahmed et al., 2013].

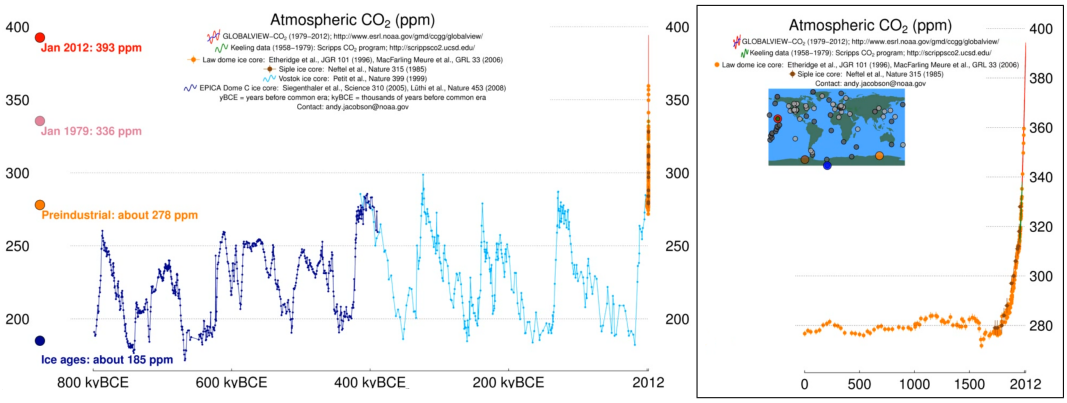

Figure 1.2: CO_2 atmospheric concentration over the last 800,000 year. In box, the last 2000 years. Adapted from [National Oceanic & Atmospheric Administration, Global Monitoring Division, 2013]

Facing these issues, one can look for alternative ways of extracting energy from the environment. For domestic use a combination of wind, solar and geothermal power can be adequate, but for industries they are not concentrated nor robust enough at present status to be the main source of energy. In contrast, nuclear energy is both reliable and concentrated. For example, one kilogram of ^{235}U can theoretically produce $\sim$ 2000 TOE. The issue of limited available reserves of uranium could be tackled by the construction of fast breeders. Super Phoenix, the industrial demonstrator in activity from 1986 to 1997, demonstrated the industrial relevance of this technology. As robust as fission is for energy production, the chain reaction mechanism constitutes at the same time its greatest strength and its largest weakness. Producing energy is facilitated by the self-amplification of the reaction but this means that the process is unstable in the eventuality of a problem in the moderation loop as dramatically illustrated by the major nuclear accident in Chernobyl in 1986. Due to the intrinsic activity of the fuel mix, heat exhaust is equally important and a failure of the system represents a serious threat to nuclear safety as reminded by Fukushima Daiichi nuclear accident. Safer-and-safer fission reactors are built (EPR being built in Normandy and Finland); however associated with ever-increasing costs.

There is another way for nuclear energy, as illustrated by the binding energy curve (see Figure 1.3). The binding energy corresponds to the potential energy that can be collected either by splitting heavy nuclei such as Uranium (this is nuclear fission) or by merging light nuclei such as Hydrogen: this is nuclear fusion. From Figure 1.3, the per nucleon energy liberated by the fusion of light elements is larger than that of the fission of heavy elements such as ^{235}U, making it a more concentrated source of energy. For example, one kilogram of deuterium-tritium mix can theoretically produce $\sim$ 8000 TOE. Thus, why nuclear fusion is not used today to produce energy? What are the issues faced on the way towards its industrial reality?

1.2 Controlling nuclear fusion

1.2.1 The possible fusion reactions

Before going any further, a fusion reaction must be chosen along the various available options. In an industrial view, the best option will be a trade off between the most probable, the most energetic reaction and the one taking place at most standard conditions. Table 1.1 summarizes the most likely reactions, associating the energy carried by the products for each reaction, the temperature which must be reached for fusion to occur and the associated cross section, measuring the probability of the reaction to happen. Given the high energy concentration of all the reaction presented, the liberated energy will not impact the choice of the reaction. The deuterium-tritium (D-T) reaction is thought to be the best candidate for nuclear fusion due to its highest probability and happening at most standard conditions. In theory, it would be a net improvement to have no neutrons as reaction products, minimising

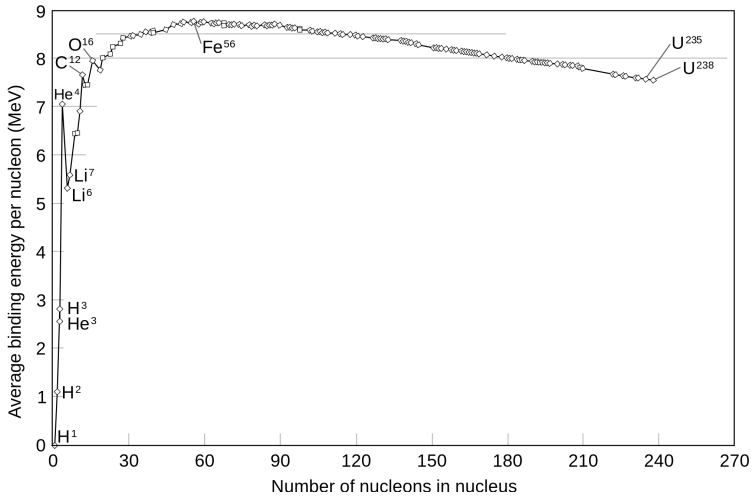

Figure 1.3: Binding energy per nucleon characterizing the stability of nuclei. The most stable is ^{56}Fe. Energy can be gained by merging very light nuclei or splitting heavy ones

Reactions	T[keV]	$\langle\sigma v\rangle/T^2[\mathrm{m^3 s^{-1} keV^{-2}}]$
^{2}H + ^{3}H → ^{4}He (3.5 MeV) + n (14.1 MeV)	13.6	$1.24\mathrm{E}^{-24}$
^{2}H + ^{2}H → ^{3}He (0.82 MeV) + n (2.45 MeV)	15	$1.28\mathrm{E}^{-26}$
→ ^{3}H (1.01 MeV) + p^+ (3.02 MeV)		
^{2}H + ^{3}He → ^{4}He (3.6 MeV) + p^+ (14.7 MeV)	58	$2.24\mathrm{E}^{-26}$
^{3}He + ^{6}Li → 2 ^{4}He + p^+ (16.9 MeV)	66	$1.46\mathrm{E}^{-27}$
p^+ + ^{11}B → 3 ^{4}He (2.7 MeV)	123	$3.01\mathrm{E}^{-27}$

Table 1.1: Most likely fusion reactions for energy production

damages and activation of the machine walls. Moreover, in reactions such as D-T where most of the energy is carried away by neutrons, a thermal cycle is needed to extract their energy by boiling water, decreasing the global efficiency of the plant. For aneutronic fusion, reactions implying ^{3}He are not considered due to its very weak presence on Earth and its cost to produce. The last reaction involving boron, in contrast, is thought as the best option for aneutronic fusion [Nevins, 1998]. But, the temperature needed to reach fusion conditions and the weak likelihood of the reaction make this source of energy unreachable for current technology. Indeed, the amplification factor Q of a reaction *i.e.* the ratio between the input power needed to sustain fusion conditions and the power that can be produced from fusion, depends on the density, the temperature and the energy losses from the medium. This energy loss is measured by the confinement time τ_E defined by the ratio of thermal stored energy over the power losses: $\tau_E = W_{th}/P_{loss}$. The power balance of a reaction is known as the Lawson criterion:

$$nT\tau_e = f(Q) \tag{1.1}$$

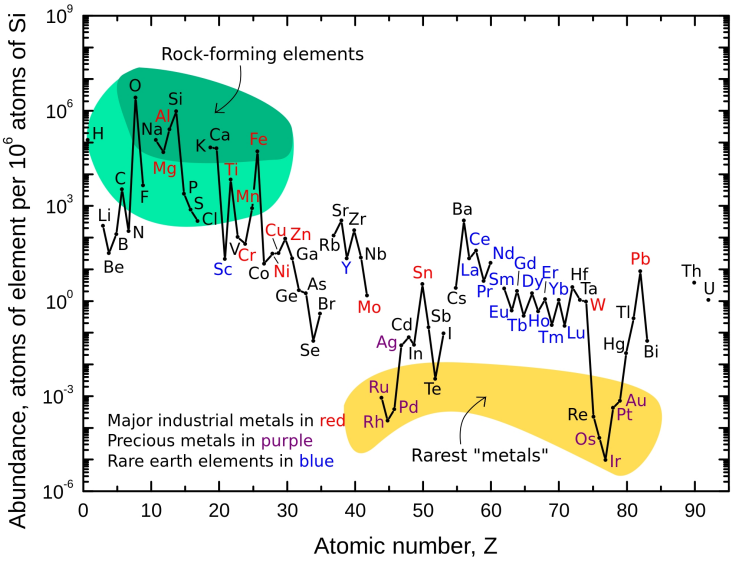

Figure 1.4: Most abundant elements in Earth upper crust[Haxel et al., 2002]

An economically viable reactor would have to satisfy $Q > 40$ requiring that $nT\tau_E > 3.10^{21}\mathrm{m}^{-3}$.keV.s for D-T reaction while it seems impossible to achieve such an amplification factor for Hydrogen-Boron reaction at present knowledge[Rider, 1997, Son and Fisch, 2004].

For now, neutronic fusion and Deuterium-Tritium reactions is therefore the only viable path. Why is there no industrial demonstrator of a Deuterium-Tritium fusion plant? Is it a resource issue? The known available resources of Deuterium are almost unlimited at mankind scale representing 0.015% of the total Hydrogen (75% of the baryonic matter in the Universe). Tritium needs to be produced because it is not stable. The best candidate for its production is lithium, present in Earth crust at concentration varying from 20 to 70 ppm by weight. Figure 1.4 compares its abundance in the Earth crust against other elements. It is found to be the 25^{th} most abundant element. Its concentration is, for example, two orders of magnitude higher than that of Uranium. The reaction to produce Tritium from Lithium is exothermic:

$$^{6}\mathrm{Li} + n \quad \rightarrow \quad ^{4}\mathrm{He} + {}^{3}\mathrm{H} \tag{1.2}$$

and used in current atomic weapons. Thus, natural resources are not the issue preventing Deuterium-Tritium fusion to be an economic reality. The issue is getting the $Q = 40$ amplification factor.

1.2.2 The possible technologies for fusion

According to Lawson criterion, 3 parameters can be varied to obtain the desired amplification factor Q: the density n, the temperature T and the confinement time τ_E. In fact, the temperature is fixed by the D-T reaction, its maximum efficiency being at $T \sim 10$ keV as indicated in Table 1.1. In addition, increasing the reaction temperature has a technological cost since accessing this range of temperatures is not an easy task (see Sec.1.3). 2 degrees of freedom remains in the parameter space: the density and the energy confinement time.

A first solution called *inertial confinement* consists in operating at high density $n \sim 10^{31}$ m^{-3} and short confinement time $\tau_E \sim 10^{-11}$ s. This principle is applied in thermonuclear weapons where the density and temperature characteristics are obtained through the explosion of a nuclear fission bomb and the resulting X-ray flux. In current experiments of inertial confinement, either powerful lasers e.g. at the National Ignition Facility or the future Laser Méga Joule, or massive electrical current – for Sandia National Laboratories Z-pinch machine – replace nuclear fission explosives. Although this concept has shown that nuclear fusion could be realized by mankind in weapons, its control to produce usable energy from this intrinsically transient source has not been achieved yet [see Glenzer et al., 2012, Figure 11].

The other solution, called *magnetic confinement*, is to use magnetic fields to confine the matter at high temperature and protect the machine walls from the interaction with energetic particles. Confinement times are of the order of the second and the density is limited to $n \sim 10^{20}$ m^{-3} [Wesson, J., 1997]. This solution uses the property that matter is progressively ionized with increasing temperature to form a plasma state globally neutral but where every particle is electrically charged (except the neutrons resulting from fusion) thus sensitive to electromagnetic fields. If high Z impurities penetrate the plasma, they can exhaust a lot of energy from the plasma due to electron relaxation/recombination radiation. Thus, it is contained inside vacuum vessels which materials are optimized to handle large heat flux and limit the plasma contamination simultaneously.

There are various configurations able to confine the plasma with comparable performances. Among them, the *stellarator* has the specificity to produce the helical magnetic field only with external coils. The drawbacks of this configuration are the necessity of complex 3D coils for optimised performances, the existence of unconfined regions and higher radial heat flux due to geometrical effects than in other configurations limiting its performances. Nevertheless, this configuration has regained interest in the scientific community [IPP, 2013] due to its intrinsic ability to operate continuously and the absence of large current-induced instabilities known as disruptions [Reux, 2010]. The other major configuration is the *tokamak*. All the studies in this thesis are made in this framework since this is the current magnetic configuration closest to produce energy from controlled nuclear fusion. This is the configuration used for ITER, the international experiment being built in the South of France

with the aim to demonstrate that usable energy can be produced by controlled nuclear fusion [IO, 2013].

1.3 The tokamak configuration

We said in the previous section that a particularity of the stellarator is to produce its helical magnetic field with only external coils. Before seeing how and why it is not the case in tokamaks, let us explain quickly why an helical magnetic field is needed.

1.3.1 Confinement of charged particles in magnetic fields

Applying Newton's second law in the terrestrial frame of reference, supposedly inertial, to a charge particle in a rectilinear magnetic field of strength B, one finds that the charge particle will describe a helix of radius $\rho_c = \frac{mv_\perp}{eB}$ with a uniform motion in the direction parallel to the magnetic field. $mv_\perp$ is the particle momentum in the direction perpendicular to the magnetic field and e is its charge. This corresponds to the situation in a solenoid. In the early days of the research on fusion, various geometries were tested [Teller, E., 1958]. Since then, it has been acknowledged that a linear device cannot magnetically confine particles sufficiently well to achieve a significant fusion rate [Wesson, J., 1997]. In contrast, a torus enables the particles to have a free toroidal movement thus solving the issue of closing the magnetic bottle. The curvature of the torus changes the dynamic of the charged particles. Ampere's law directly expresses that the magnetic field strength is inversely proportional to the major radius R due to the volume expansion with R. The particle cyclotron motion will be altered, the particle Larmor radius ρ_c being larger at outer radii and shorter at inner radii. This and its secular effects are illustrated on a cartoon Figure 1.5, the secular effect being a vertical drift of the particles. As explained in more details in the next chapter, another drift comes from the curvature of the magnetic field itself. Moreover, in fusion devices, both ions and electrons coexist. The vertical drift is responsible for a charge separation. An electric field is then created to counterbalance the charge separation. It is responsible for an additional drift [Sarazin, 2008]. Overall, because of these drifts and without the introduction of another magnetic field, the energy confinement time is limited to $\tau_E \sim 10^{-3}$ s which is well shorter than the estimated $\tau_E \sim 1$ s necessary to reach fusion conditions [Hennequin, 2007].

1.3.2 Inducing a poloidal magnetic field

In order to correctly confine the plasma, a poloidal magnetic field is needed. Contrary to the stellarator case, it is not created by the tokamak coils. Instead, a toroidal current is induced in the plasma through transformer effect by a stack of coils placed in the torus centre called central solenoid. As a reaction to this imposed circular current, a poloidal magnetic field

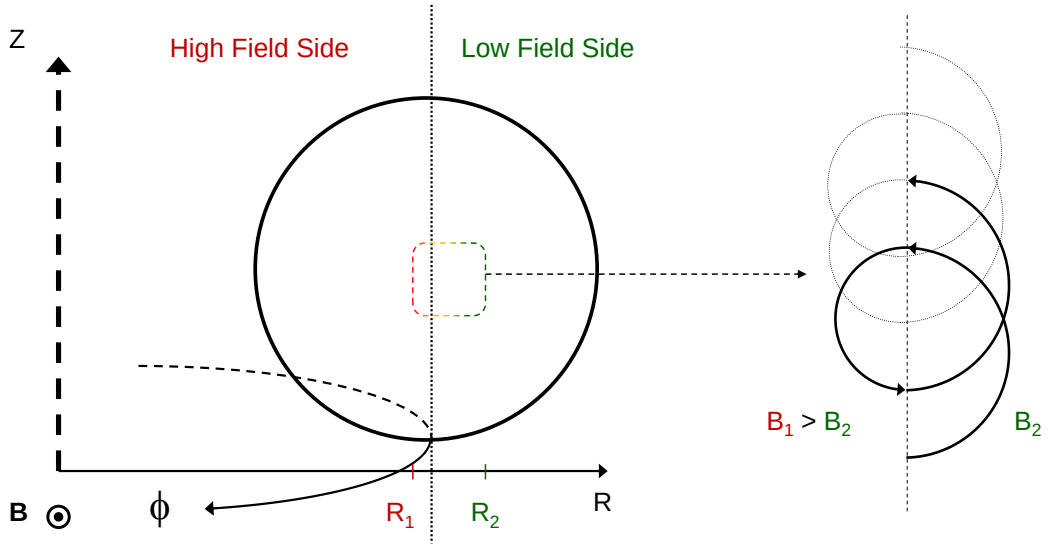

Figure 1.5: Cartoon of the vertical drift due to the curvature of the magnetic configuration

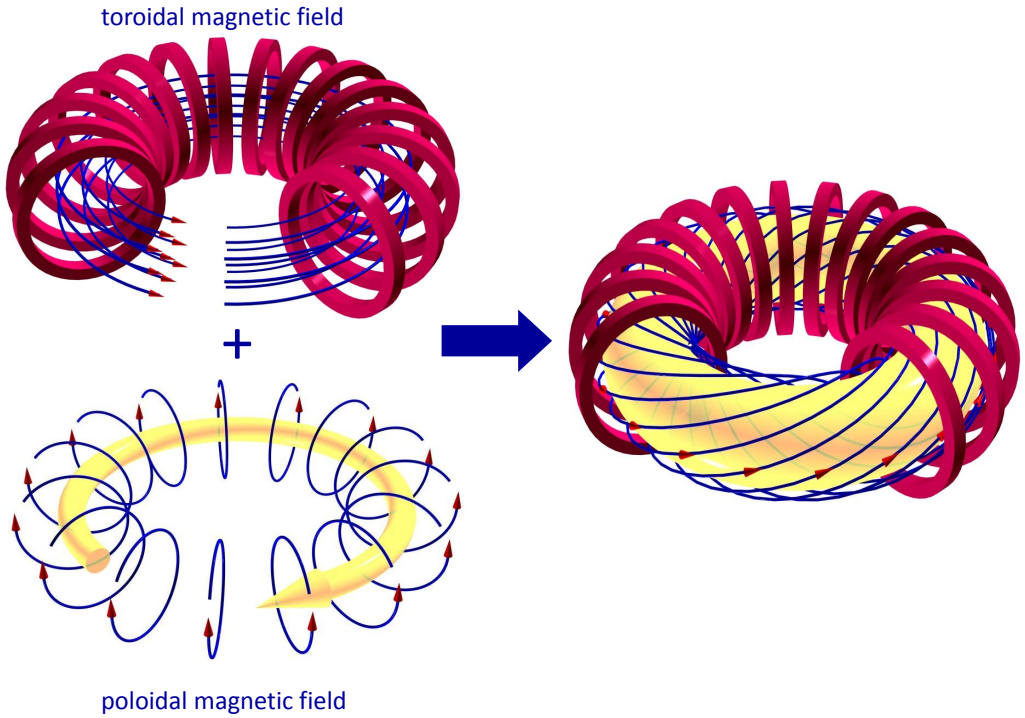

Figure 1.6: Cartoon of the magnetic field in a tokamak. The toroidal magnetic field is created by the external coils (in red). The poloidal magnetic field is created by the plasma in reaction to an electric current forcing (yellow arrow).

is created. As illustrated by Figure 1.6, the resulting magnetic field lines are spirals rolled around a torus. This has the effect to transform the radial drifts just exposed into parallel drifts sorting this issue. The transformer effect needs a variation of current in the central solenoid to work. As a *continuous* poloidal magnetic field is required to confine the plasma, a *linear* current ramp has to be applied. This implies that, in the absence of any other current source, the tokamak cannot work continuously. What explains the success of the tokamak configuration is the good confinement obtained with coils somewhat simpler than those needed in stellarators for example and the possibility for ohmic heating.

1.3.3 Heating methods and additional current drive

Inducing an electric current in the plasma to confine it has the side benefit to heat it due to its electric resistance, this is called *ohmic heating*. Moving along the torus, electrons collide with ions transferring part of their momentum to the later. However, with higher energy, the particles acquire larger momentum, the cross section of the collisions decreases. Macroscopically, this translates into a decrease of the electric resistance. Thus, ohmic heating brings the plasma up to ~ 1 keV. To access higher temperatures, non-inductive heating systems are required. [Wesson, J., 1997]

- *Neutral Beam Injection* (NBI) consists in injecting energetic deuterium atoms in the plasma. The neutral particles then thermalise (in most cases) onto ions by collisions.
- The other heating systems use the different plasma resonance frequencies. Two frequencies correspond to the ion and electron fast motion around the field line: the cyclotron motion. They are called *Ion Cyclotron Radio-frequency Heating* (ICRH) and *Electron Cyclotron Radio-frequency Heating* (ECRH). ICRH are the low frequency waves ranging from 10 to 50 MHz whereas ECRH are high frequency wave at $\sim$ 100 GHz. In between them, 3 to 5 GHz, another resonance frequency is used, the *Lower Hybrid* (LH).

As electric current induction heats the plasma, non-inductive heating systems can drive electric current. Due to the interaction between energetic particles and ions, Neutral Beam Injection can drive a fast ion current [Wesson, J., 1997, § 3.13]. This is done by rotating the NBI away from the perpendicular to the torus giving a preferred direction to the beam. For current drive by ECRF, the same technique is employed, producing a finite parallel wave number. The waves then exchange energy with the electrons via Landau damping, accelerating them in the parallel direction. For current drive by ICRF and LH, the straps are asymmetrically phased such that a finite parallel wave number is produced by the wave-interaction in front of the antennas, before propagation and absorption by Landau damping. Due their reduced efficiency with increasing trapped particle fraction, ECRF and ICRF are used for on-axis current drive [ITER and Editors, 1999]. In contrast, LH is mainly used for off-axis current generation due to penetration issues up to the plasma centre. Its

larger parallel electric field ($E_\parallel$) makes LH the most efficient way to drive current with RF $\eta_{LHCD} \sim 0.3 10^{20} \mathrm{A.W^{-1}.m^{-2}}$ versus $\eta < 0.1 10^{20} \mathrm{A.W^{-1}.m^{-2}}$ in current experiments for ECRF-ICRF induced current-drive. However the efficiency of ECCD is expected to be close to $0.3 10^{20} \mathrm{A.W^{-1}.m^{-2}}$ in ITER [ITER and Editors, 1999]. The combined low efficiency of LH heating and good efficiency of LHCD compared to other RF systems leads to the fact that the Lower Hybrid is essentially used for current drive in current experiments [Saoutic et al., 2011].

With all these current sources, it is possible to extend the operation of the tokamak way beyond the solenoid current ramp limitations. For example in Tore Supra, the tokamak operated at CEA Cadarache since 1988, the longest shot is 6 min long [van Houtte et al., 2004] whereas the average duration of a shot without additional current drive (ohmic discharge) is of the order of tens of seconds depending on the density.

1.4 Context of this work and outline

Fusion of light nuclei appears to be an attractive way to produce energy. Among the possible reactions, the deuterium-tritium reaction is the only realistic option with today's technology. The major issue faced when attempting to fuse nuclei is the required high energies. The reactants are in a specific state called *plasma*. The plasma and the wall need to interact as little as possible, in order to protect the wall and limit the contamination of the plasma. In tokamaks, this is ensured by a toroidal magnetic nest induced by coils and the generation of an electric current in the plasma.

To date, with this technology, an amplification factor of $Q \sim 0.7$ was reached in the Joint European Torus (JET) in Culham, Oxfordshire [JET Team, 1999] with 16 MW of fusion power. Extrapolations from D-D experiments in JT-60U in Japan indicate that an equivalent amplification factor $Q_{\mathrm{eq}} = 1.25$ would have been achieved if it had been operated with D-T [Fujita et al., 1999]. Shots longer than 6 minutes were achieved in Tore Supra and recently in EAST [Wan and Collaborators, 2009] thanks to superconducting coils. However these long discharges exhibit a very low amplification factor.

A larger tokamak with superconducting coils, ITER, is under construction in southern France with the goal to achieve $Q = 10$ during 1000 s which would demonstrate the experimental practicability of producing energy in steady state (at a plasma level) with thermonuclear fusion. A larger machine is indeed needed in order to achieve amplification factors significantly larger than unity because of the turbulence developing in the tokamak plasmas due to the injection of large amounts of energy. Taking turbulence into account in the design of ITER led to the conclusion that an 800 $\mathrm{m^3}$ vacuum vessel is needed whereas the largest one at present day is 80 $\mathrm{m^3}$ in JET.

Nevertheless, even if long discharges with significant amplification factor are managed in ITER, major issues remain to be solved before the industrial viability of fusion as an energy

source. How the plasma will self-organise in the presence of alpha particles is largely unknown. What damages will be induced in the tokamak coils and structure by the production of highly energetics neutrons remain an open question as well. The production of tritium in-situ remains to be tackled and remote handling operations are technological challenges. Therefore, fusion is still a long-term solution of the Energy challenge: the technology for a fusion power plant is thought to be mature enough by the 2050's [Romanelli et al., 2012]. In the meantime, other alternatives to oil, coal and gas must be explored: solar energy (both thermal and photovoltaic), wind and marine current power, geothermal energy, Gen IV fission reactors.

Reaching the D-T fusion conditions in the centre of the plasma involves the injection of a large amount of power into it. This brings the matter out of thermodynamic equilibrium. This implies relaxation mechanisms. Relaxation can occur by means of large intermittent events. Among them, the so-called *sawteeth* can be present in the centre of the plasma. The so-called *Edge Localized Modes* (ELMs) are present at the outermost confined region of the plasma in case of strong pressure gradients. These processes are out of the scope of this work. They occur on a much longer time scale than the micro-turbulence studied in this thesis. Moreover these events transport a significant amount of the energy stored in the plasma. Therefore, the perturbative methods developed in this work for micro-turbulence cannot be applied to study them.

Micro-turbulence limits the performances of the tokamaks by inducing a radial heat transport, thus limiting the energy confinement time and responsible for the inability of current fusion experiments to achieve large amplification factors. It is therefore essential to understand its principle with the aim of reducing it. Micro-turbulence corresponds to small scale events compared to the size of the machine that individually bear a small quantity of energy compared to the total stored energy on time scale much shorter than the energy confinement time. From a macroscopic point of view, the mechanisms at hand thus appear more continuous than the macro-turbulence mentioned above.

The radial heat transport — exhibiting a typical diffusivity of $1\mathrm{m}^2.\mathrm{s}^{-}1$ in current machines — can be reduced by the creation of mean flows which pump out the energy from the turbulence thus reducing the induced radial heat flux. This mechanism is studied in detail in Chapters 3 and 4 with a quasi-linear gyro-kinetic approach. If mastered, the turbulence suppression could significantly reduce the required size of a fusion power plant, reducing the associated cost.

Moreover, with larger machines, the experimental cost is larger. Therefore, the predictive capabilities of numerical simulations need to be perfected to improve the success rate of experiments. Integrated simulations modelling (heat, particle and momentum) sources and transport together with the magnetic equilibrium are needed. The code extended in this work, QuaLiKiz is part of this framework as detailed in Chapter 3: the transport due to the electro-static micro-turbulence is calculated in QuaLiKiz.

In Chapter 2, the main physical mechanisms causing the development of the micro-turbulence are discussed. Only the mechanisms involving the fluctuations of the electrostatic potential are studied since they are the largest contributors to the micro-turbulence-induced transport. The theoretical base of this work is reviewed later on. The particle trajectories are studied in details. Resulting from this analysis, a necessary simplification of the problem complexity appears possible. This is the gyro-kinetic approximation presented in § 2.2.2. The electro-neutrality condition used as the corner stone of the work presented in this thesis is derived in the gyro-kinetic framework.

In Chapter 3, the equations behind the numerical model developed for this work are derived. The choice of the equilibrium distribution function function is first explained. The eigenvalue/eigenfunction equation deriving from the electro-neutrality condition is presented later on, illustrating the influence of the equilibrium distribution function. The eigenfunctions used in QuaLiKiz are derived next. The influence of the mean flows on the linear modes is then studied.

In Chapter 4, the quasi-linear model, as used in QuaLiKiz is presented and its validity studied after a brief review on the achievements of such models. In particular, the construction of the saturated potential is explained in details. The gyro-kinetic quasi-linear momentum flux is derived later on. The mean flow impact on the heat, particle and momentum fluxes is reviewed in details. QuaLiKiz's predictions for the fluxes in presence of $\mathbf{E} \times \mathbf{B}$ shear and sheared parallel velocity are compared to non-linear gyro-kinetic simulations.

Finally, in Chapter 5, the experimental point of view of the topic is given and torque modulation experiments allowing to experimentally evaluate the diffusive and convective terms of the momentum flux are compared to QuaLiKiz's predictions.

2

Micro instabilities in tokamak plasmas

Describing all the instabilities that can develop inside a tokamak plasma is a task far beyond the scope of this thesis. Nonetheless in this chapter some flavour of the main mechanisms are given. We recall that a tokamak plasma is basically a system out of equilibrium that tends to relax to a more stable state. However it is forced to stay out of equilibrium by the injection of great amounts of energy through NBI or RF heating. This can lead to the development of macro instabilities that modify strongly the confinement properties of the magnetic nest and cause a strong intermittent transport of energy towards the cooler regions *i.e.* outer regions. If not controlled, they can cause a confinement collapse. Here, we do not address this issue.

Once the main macro-instabilities are avoided, the confinement time is determined mostly by the micro-instability activity hence the need to understand them in order to optimize the tokamak performance. As for macro-scale events, two main classes of micro-instabilities can be identified: *pressure*-driven instabilities and *current*-driven instabilities. Although the latter class of instabilities has important consequences in tokamak plasmas, setting for example limits on the plasma current and pressure, it will be not be treated in this thesis. Indeed, in the work presented hereafter, the magnetic equilibrium is supposed fixed and the pressure-driven instabilities decoupled from the evolution of the macroscopic magnetic field. For that matter, no fluctuations of the magnetic field will be considered since only pressure-driven instabilities are studied. This is called the electrostatic (or low-β) limit.

First, the main electrostatic instabilities are explained, then the gyro-kinetic approximation is presented and derived in the action-variable framework.

2.1 Physics of the micro-instabilities

In this first section, a general overview of the main electrostatic instabilities driving turbulent transport in magnetically confined plasmas is given. This is intended as a qualitative description of the main physical mechanisms at play which are modelled and quantitatively examined later on the course of this thesis. We isolate three different electrostatic mechanisms that can drive turbulent transport:

- The interchange instability induced by the co-linearity of pressure and magnetic field gradients analogous to the hydrodynamic Rayleigh-Bénard instability;
- The drift-wave instability which arises from a phase shift between electrostatic and density fluctuations;
- The parallel velocity gradient instability caused by a strong gradient of the parallel velocity like Kelvin-Helmholtz instability in fluid dynamics.

The later is rarely unstable linearly in tokamaks actual conditions. It is mostly expected as a secondary instability *i.e.* linearly stable but non-linearly destabilized by another one.

2.1.1 The interchange instability

Tokamak plasmas being successfully forced out of equilibrium, large gradients of density and temperature develop inside the confined region. Combined with the toroidal geometry of tokamaks, this induces an *interchange* instability, that is: interchanging flux tubes is energetically favourable. Figure 2.1 details the conditions of (in)stability and illustrates how this instability operates.

Assuming that some fluctuation of the electrostatic potential ϕ exists is a preliminary condition to the study of any electrostatic instability. We suppose the existence of small convection cells *i.e.*closed contour lines of constant ϕ at the equatorial mid-plane on the low field side of the tokamak as indicated by Figure 2.1. As indicated in the previous chapter, the particles undergo velocity drift perpendicular to the magnetic field direction in their motion around the torus. In the configuration of Figure 2.1, the electric drift $\mathbf{v}_E$ is inward in-between the two cells and is outward on top and at the bottom of the cartoon. The curvature and ∇B drifts — responsible for the charge separation — are vertical: upward for the electrons (blue array arrow) and downward for the ion (red array arrow). For a formal derivation of the drift frequencies, please report to the next section: § 2.2.1.2.

The condition of instability of the interchange mechanism is that the temperature gradient and the magnetic field gradient point in the same direction which is the case in the low field side of tokamaks. This is reminiscent of the condition of instability of Rayleigh-Bénard convection cells with the magnetic field gradient playing the role of gravity. In fact, a

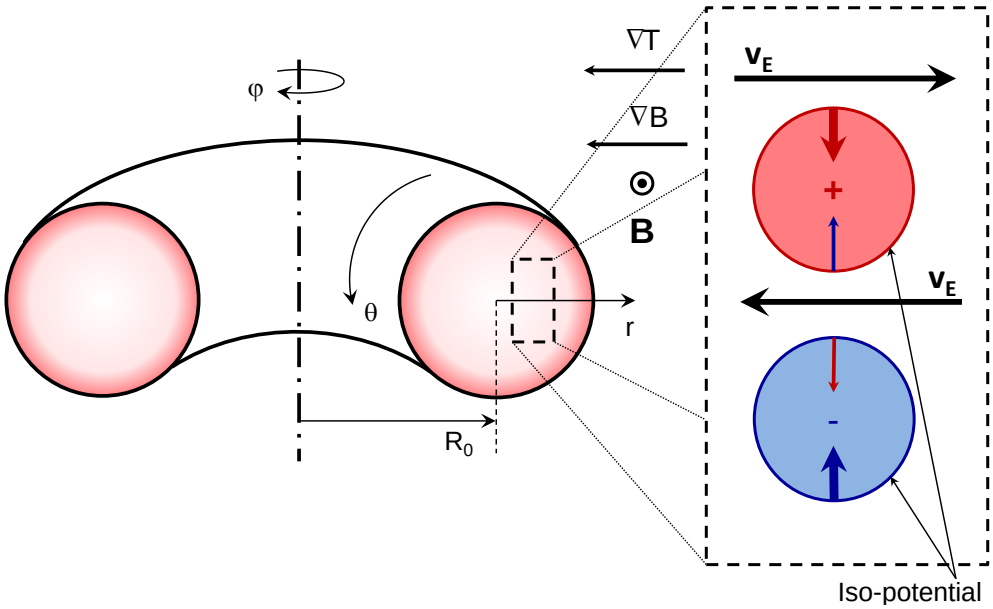

Figure 2.1: Cartoon of a tokamak plasma illustrating the physical mechanisms of the interchange instability after Sarazin [2008]

formal analogy between interchange and Rayleigh-Bénard instabilities can be demonstrated [Sarazin, 2008].

In the interchange case, the particles present at the mid-plane move inward (in Figure 2.1 simple cartoon) due the electric drift. The ions then drift downward, alimenting the negatively charged cell, whereas the electrons drift up, toward the positively charged cell. However, the situation is opposite at the top of the positive cell and at the bottom of the negative one: the electrons drift toward the negative cell and the ions drift towards the positive cell. This reversed situation is due to an inversion of the poloidal electric field inducing an inversion of the electric drift; whereas the vertical drift caused by the curvature and the magnetic field inhomogeneity stays unchanged.

On the low field side, the latter situation brings more particles into the convective cells due to a higher mobility of the particle (because the temperature is higher at the centre) since the phenomenon studied here is instrically transitory. This amplifies the inhomogeneity of the electrostatic potential making the interchange unstable. On the high field side, the temperature gradient is reversed so the former scenario brings less particles. The electrostatic potential inhomogeneities are then resorbed naturally stabilizing the interchange mechanism. Since the particles travel around the torus essentially following the twisted field lines illustrated in Figure 1.6, they experience both stable and unstable regions[1]. Nonetheless, the rapidity of the unstable processes entails an interchange instability on the low field

[1]Some particles do not have enough energy to complete a torus revolution due to the inhomogeneities of the magnetic field (see § 2.2.1.3 for a clarification)

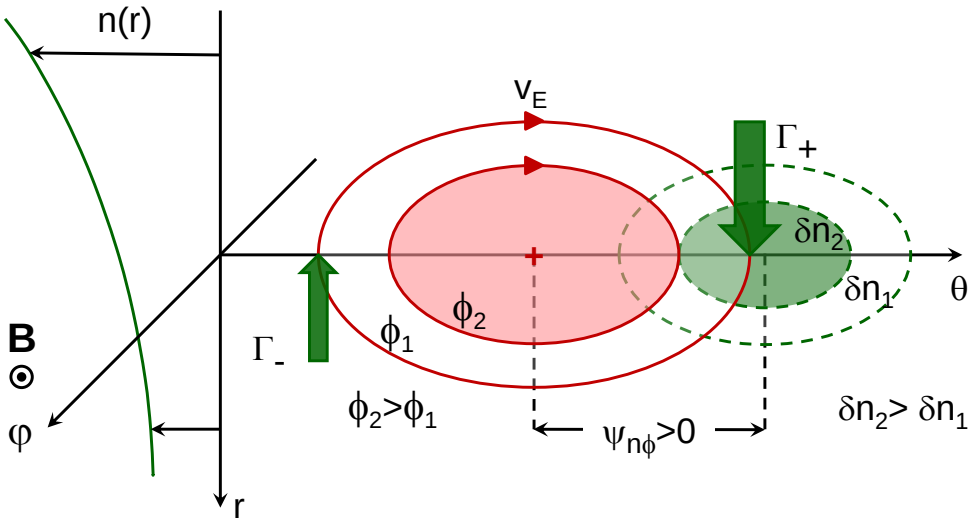

Figure 2.2: Schematic representation of the drift wave instability after [Horton, 1999]

side. Beside, there are also particles trapped on the low field side, which enhance the overall instability. The interchange instability induces a radial transport as illustrated in chapter 4. The effect of the parallel resistivity will not be discussed in the following since the parallel current $j_{\|}$ is not taken into account. The parallel resistivity increases the efficiency of the interchange instability since it tends to decouple stable and unstable regions but is significant only at the very edge where the collisionality is significant enough.

2.1.2 The drift-wave instability

The drift wave corresponds to the drift of a perturbation of electrostatic potential as illustrated in Figure 2.2. The perturbation of the electrostatic potential (in red) creates an electric field in the θ-direction. Due to their low inertia, the electrons may be considered to respond instantly to any change of the electric potential. The fluctuations of electron density (in green) and electric potential are then in phase (which is obviously not the case in Figure 2.2). The electrons are then pulled out of the high density, low potential regions toward the low density, high potential regions. This causes an oscillation of the electric potential perturbation but no instability.

A phase shift between the electron density and the electric potential is now considered. If the phase between the electron density and the electric potential is negative (which is the case presented on Figure 2.2), more electrons come in the super-density region than come out due to the strong density gradient. This causes the electron perturbation to build up as illustrated by Figure 2.2. In case of a positive phase, the situation is reversed and the density inhomogeneity is resorbed by the $\mathbf{E} \times \mathbf{B}$ advection.

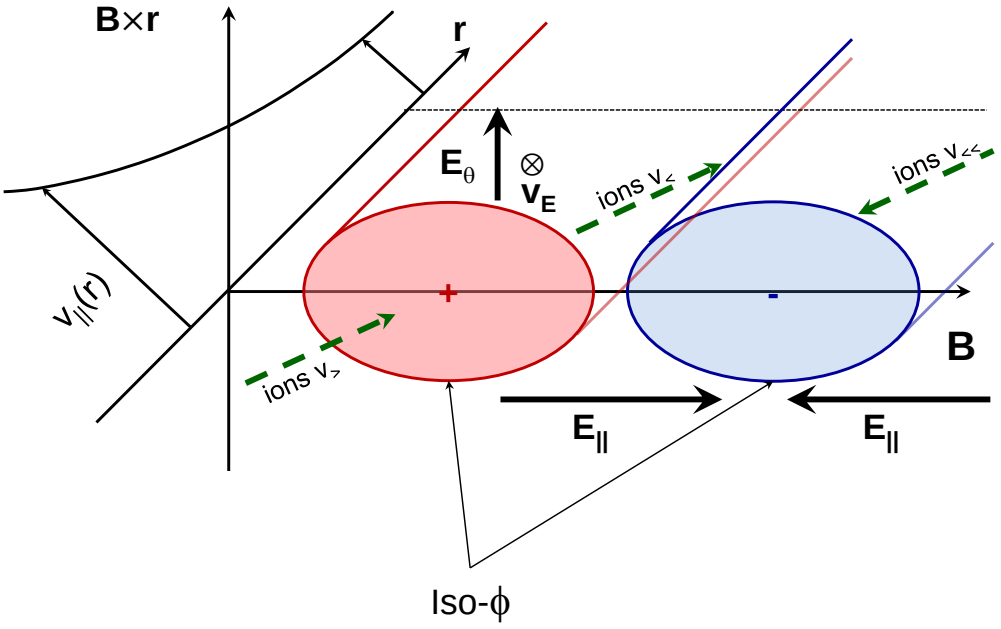

Figure 2.3: Cartoon of the parallel velocity gradient instability after [Catto et al., 1973]

We talked about density gradients and density fluctuations to explain the *interchange* and *drift wave* mechanisms. In fact, the quantity to consider is the pressure. Thus the mechanisms previously presented are still at play in the absence of a density gradient as long as there is a temperature gradient. This precision is worth noticing since in tokamaks plasmas the normalized density gradients are much smaller than the temperature gradients.

2.1.3 The parallel velocity gradient instability

In tokamak plasmas, large parallel flows can develop since the direction of the magnetic field is mostly unconstrained[2]. Moreover, the additional heating systems — predominantly neutral beam injection — produce very energetic particles that acquire large velocities. The parallel velocity gradient instability redistributes this reservoir of free energy by increasing the vorticity in the parallel direction. The mechanisms operating this redistribution are illustrated by Figure 2.3.

Considering again a fluctuation of the electric potential, let us focus on its parallel dynamics. Ions from the region of increased potential will by accelerated by the parallel electric field. At the same time they experience an outward $\mathbf{E} \times \mathbf{B}$ drift in the radial direction. Due to the radial gradient of the parallel velocity, the initial ions are replaced

[2]The direction of motion of the electrons is actually forced by the electric current. In the presence of a significant toroidal variation of the toroidal magnetic field (ripple), the toroidal rotation is fixed by the force balance equation but remains substantial.

by other ions with larger velocities. This situation is stable due an acceleration of the fluid velocity by both effects.

Considering now the ions from the region of decreased potential, they are slowed down by a parallel electric field in the opposite direction inducing an inward $\mathbf{E} \times \mathbf{B}$ drift. The interaction of both mechanisms creates a region of increased vorticity where the ions are slowed down and a region of low vorticity where the ions are accelerated. The structure created is then similar to the hydrodynamic Kelvin-Helmholtz pattern observed sometimes in the clouds.

For the mechanism to be unstable, the parallel velocity gradient must be larger than the parallel wave number of the potential fluctuation. This mechanism is enhanced by previous instabilities which develop electric potential fluctuations towards larger scales (lower wave numbers). This simple picture is confirmed by quantitative discussion in chapter 3 where the linear coupling between interchange instability and parallel velocity gradient is studied. This *linear* interplay is however different from the secondary instability paradigm which is described here in a simplistic way. Indeed only the linear growth rate of the pressure driven instabilities are studied in chapter 3 without any assumption on the turbulent state.

2.2 Simplifying the complexity of the particle motion equation

Now that the main physical mechanisms studied in the course of this thesis have been qualitatively presented, let us introduce the general background of this work with a more formal description starting with the particle trajectories and the scale separation that is possible to performed in strongly magnetized tokamak plasmas. Then the so-called *gyro-kinetic* theory is introduced and its associated invariants. Within this framework a linearised (gyro-kinetic) electro-neutrality equation is derived using a variable system making use of the symmetries of the system *i.e.*the invariants of motion.

2.2.1 Geometry and particle trajectories

2.2.1.1 Magnetic geometry in tokamak plasmas

As outlined in the previous chapter, the magnetic geometry of tokamaks consists in a series of closed nested surfaces. The toroidal magnetic field is created by external coils while the poloidal magnetic field results from the plasma self-organised response to the induction of a toroidal current. The resulting magnetic field can be expressed by the relation:

$$\mathbf{B} = I(\psi)\nabla\varphi + \nabla\psi \times \nabla\varphi \tag{2.1}$$

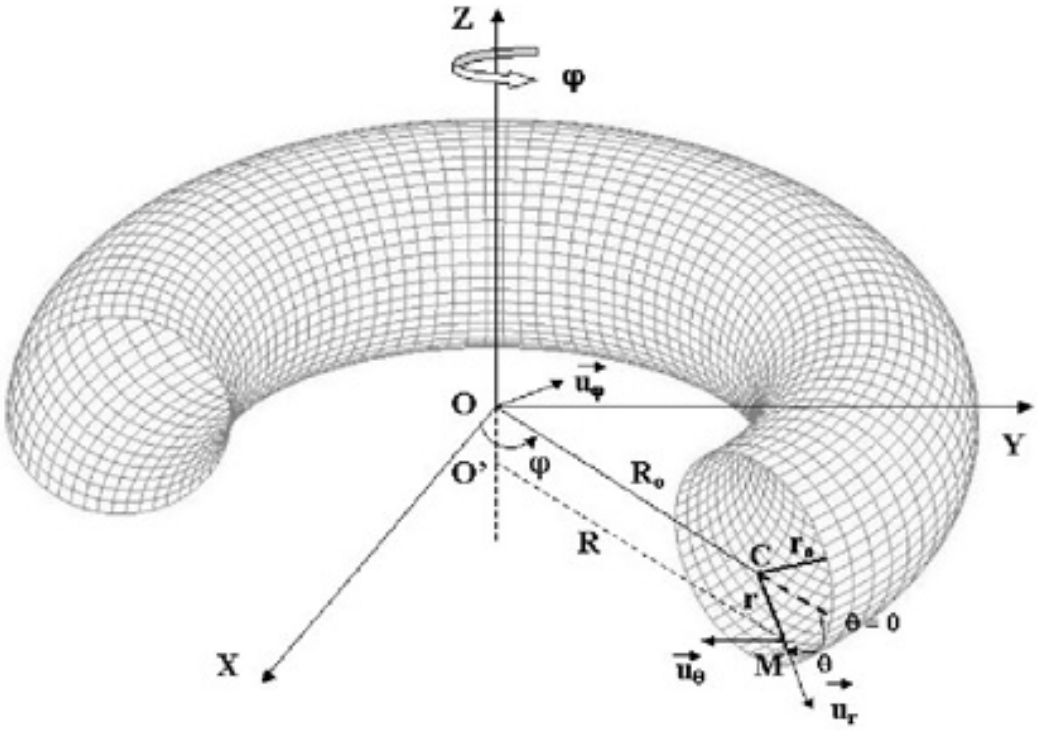

Figure 2.4: Parametrization of the tokamak geometry. The example given is the simplified circular geometry used in this work where ψ can be identified to r

In (2.1) ψ is the magnetic poloidal flux normalised to 2π.φ stands for the toroidal angle as indicated in Figure 2.4 and I is a flux function related to the poloidal current circulating inside a magnetic surface in the plasma. The quantity that measures the winding rate of the magnetic field lines or equivalently the rotational transforms that enables an efficient confinement of particles is q defined by

$$q(\psi) = \frac{1}{2\pi}\int_0^{2\pi} \frac{\mathbf{B}\cdot\nabla\varphi}{\mathbf{B}\cdot\nabla\theta}\mathrm{d}\theta \tag{2.2}$$

q can be understood as the number of toroidal (φ) revolutions performed by a field line for one poloidal (θ) revolution. An adequate system of coordinates can then be defined by (ψ,θ,φ). In the simplified geometry presented in Figure 2.4, the field lines label ψ can be identified to the small radius r. However, the centre of the nested radii labelling the field lines is evolving with R due to a change in the ratio between the magnetic pressure ($P_{\mathrm{mag}} = B^2/2\mu_0$) and the plasma pressure ($P = nT$) represented by the α parameter: $\alpha = q^2\beta R\nabla P/P$. β is the ratio of the plasma pressure to the magnetic pressure. A field-aligned coordinate system (ψ,θ,ζ) can also be defined by using the new variable $\xi = \varphi - q(\psi)\theta$ [Beer, 1995]. In this system, the θ variable corresponds both to the poloidal angle at fixed φ and a parametrization of the distance along the field line at fixed ζ. This systems reveals powerful for numerical simulations since it embeds the natural tendency of the plasma structures to follow the field

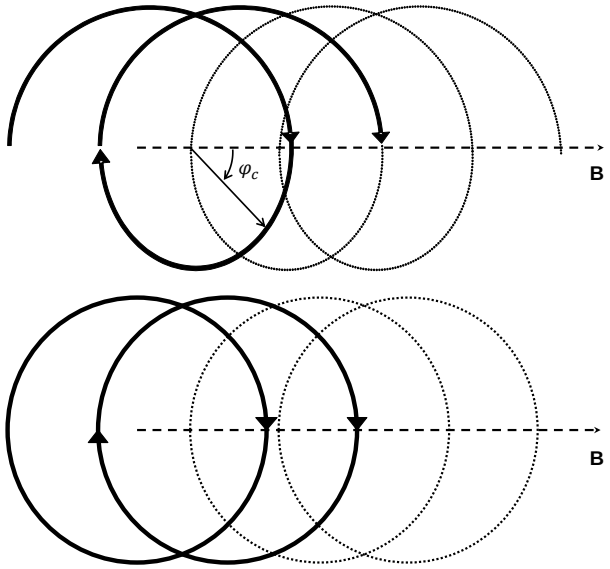

Figure 2.5: Top: Particle motion along a field line (neglecting the drifts) Bottom: Representation of the same motion within the adiabatic theory. The fast motion is embedded in the circles. The slow motion corresponds to the shift of the circles along **B**

lines. More comments on this are given when studying the structure of the electrostatic fluctuations in § 3.2.

2.2.1.2 Guiding centre motion and particle drifts

As explained in the previous chapter, the charged particles move helically along the magnetic field lines in an homogeneous magnetic field. In strong magnetic fields such as tokamaks environment, the temporal evolution of the electromagnetic fields **E** and **B** can be considered slow compared to the cyclotron frequency $\omega_c = |e_s B/m_s|$. A complete scale separation is possible in the framework of the *adiabatic theory* which describes cases where the spatial scale of the magnetic field evolution is larger than the Larmor radius $\rho_c = m_s v_\perp / e_s B$:

$$\rho_c \left| \frac{\nabla \mathbf{B}}{\mathbf{B}} \right| \ll 1 \tag{2.3}$$

In a typical tokamak magnetic field (~ 3T), the cyclotron frequency is about 100GHz for the electrons and 50MHz for the ions. If one recalls the frequencies at hand for RF heating of the plasma — of the order of the ion cyclotron frequency or larger — one easily deduces that RF heating cannot be treated within the adiabatic theory. But for the turbulence study, the frequencies involved are much smaller than the cyclotron frequencies, hence the scale separation can be carried out.

The scale separation allowed by the adiabatic theory is a very powerful tool to characterize the particle motion in tokamaks. A cartoon illustrating the simplification brought by this scale separation is given in Figure 2.5. The characterisation of the particle motion is much simplified, as derived in the following. Two scales are considered:

- the fast dynamics $\tilde{\mathbf{v}}$ (of gyro-phase φ_c, typical frequency ω_c and typical spatial scale ρ_c) corresponds to the smallest scales;
- the slow evolution of the quantities averaged over the cyclotron motion $\langle \mathbf{v} \rangle = \oint \mathbf{v} \mathrm{d}\varphi_c/(2\pi)$ corresponds the largest scales.

When assuming a strongly magnetized plasma, the Coulomb force can be considered much weaker than the Lorentz force. Moreover, the amplitude of the fast variations of the magnetic field $\tilde{\mathbf{B}}$ is much smaller than $\mathbf{B}$ according to (2.3). In that case, the fast motion comes down to the fast cyclotron motion:

$$\tilde{\mathbf{v}} = \rho_{\mathbf{c}} \times \omega_{\mathbf{c}} \tag{2.4}$$

Let us focus now on the centre-guide motion *i.e.* the particle motion averaged over the gyro-motion, described by:

$$m_s \mathrm{d}_t \langle \mathbf{v} \rangle = e_s \left(\langle \mathbf{E} \rangle + \langle \mathbf{v} \rangle \times \mathbf{B}_G + \langle \tilde{\mathbf{v}} \times \tilde{\mathbf{B}} \rangle \right) \tag{2.5}$$

In (2.5), $\tilde{\mathbf{B}}$ remains to be characterized. At lowest order, $\tilde{\mathbf{B}}$ is approximated by the first term of its Taylor expansion $\tilde{\mathbf{B}} = (\rho_{\mathbf{c}} \cdot \nabla) \mathbf{B}_G$, $\mathbf{B}_G$ being the magnetic field at the centre-guide position. Using (2.4) to explicit the cross-product $\langle \tilde{\mathbf{v}} \times \tilde{\mathbf{B}} \rangle$ involves a little tensorial algebra:

$$\langle \tilde{\mathbf{v}} \times \tilde{\mathbf{B}} \rangle = \frac{\omega_c \rho_c^2}{2} \left(\mathbf{B} (\nabla_\perp \cdot \mathbf{B}_\perp)/B - \nabla_\perp B \right) \tag{2.6}$$

(2.6) can be simplified by recalling that $\mathbf{B}$ is divergence-free such that $\nabla_\perp \cdot \mathbf{B}_\perp = -\nabla_\parallel \cdot \mathbf{B}$. In the end [see Sarazin, 2008, for details], (2.5) can be written as

$$m_s \mathrm{d}_t \langle \mathbf{v} \rangle = e_s \left(\langle \mathbf{E} \rangle + \langle \mathbf{v} \rangle \times \mathbf{B}_G \right) - \mu_s \nabla B_G \tag{2.7}$$

where the adiabatic invariant is defined as $\mu_s = e_s \omega_c \rho_c^2/2$.

Let us recall that presenting the expression of the velocity drifts motivated the derivation of (2.7). The drifts correspond to $\mathbf{v}_G = \langle \mathbf{v} \rangle_\perp - v_\parallel \mathbf{B}/B$. The expression of $\mathbf{v}_G$ is accessible by multiplying (2.7) by $\times \mathbf{B}/B_G^2$. The perpendicular direction is constrained by the magnetic field, whereas the parallel direction is essentially free. Under such conditions, the derivative of the drift term $\langle v \rangle_\perp = \mathbf{v}_{G\perp}$ is treated as a perturbation and neglected at leading order. This simplifies greatly the treatment of (2.7). The parallel velocity experiences a centrifugal force due to the curvature of the magnetic field resulting in a drift:

$$\mathrm{d}_t v_\parallel \Big|_\perp = v_\parallel^2 \nabla_\parallel \mathbf{B}/B = v_\parallel^2 \frac{\mathbf{N}}{R} \tag{2.8}$$

according to the definition of the normal $\mathbf{N}$ of a curve (since $\mathbf{B}$ is obviously tangent to the field line). R is the curvature radius. It also corresponds to the major radius of the tokamak.

The other drifts come from the inhomogeneity of the magnetic field ∇B and from the mean electric field $\langle E \rangle$:

$$\mathbf{v}_{G\perp} = \mathbf{v}_E + \mathbf{v}_{ds} = \frac{\langle E \rangle \times \mathbf{B}}{B^2} + \frac{\mathbf{B}}{e_s B^2} \times \left(\mu_s \nabla B + m_s v_\parallel^2 \frac{\mathbf{N}}{R} \right) \tag{2.9}$$

The three drifts mechanisms briefly described in the first chapter are recovered in (2.9). The curvature and ∇B drifts are responsible for a charge separation as indicated by "e_s" in the second term in the RHS of (2.9) and illustrated by Figure 1.5. This charge separation is then responsible for the emergence of mean electric field which causes a species independent drift.

We shall verify that neglecting the term "$\mathrm{d}_t \mathbf{v}_{G\perp}$" in (2.7) is consistent with the expression for $\mathbf{v}_{G\perp}$. The dominant term in $\mathbf{v}_{G\perp}$ being the electric drift velocity, the ratio

$$\frac{\mathrm{d}_t \mathbf{v}_{G\perp}}{e_s/m_s \mathbf{v}_{G\perp} \times \mathbf{B}_G} \approx \frac{\omega}{\omega_c} \tag{2.10}$$

is much smaller than unity according to the adiabatic theory, validating the consistence of (2.9) with the approximations performed for its derivation.

Additionally, in the adiabatic limit and when the electromagnetic field is constant in time, the particle motion is characterized by three invariants:

- the total energy $h_0 = m_s v^2/2 + e_s \phi$ or equivalently $E = m_s v_{G\parallel}^2 + \mu_s B + e_s \phi$;
- the magnetic moment $\mu_s = m_s v_\perp^2/(2B_G)$ already presented as the adiabatic invariant;
- the toroidal kinetic momentum $p_\varphi = e_s \phi + m_s R v_\varphi$.

The total energy and the toroidal momentum are exact invariants whereas the magnetic moment is conserved only in the adiabatic limit. It is worth noticing that the toroidal momentum p_φ is only an exact invariant under the assumption that a tokamak is axisymmetric in the φ direction. In reality, this is not the case due to the finite number of coils. This causes additional drifts and constrains the radial electric field, hence the toroidal velocity. However important, this symmetry breaking will not be treated in this work due to its cost in time for numerical simulations (essential in this work as explained in Chapter 3). For now, this effect is foreseen to be implemented as a source of angular momentum in integrated simulations.

2.2.1.3 Trapped particles and banana orbits

In tokamaks, all particles do not complete the revolution around the torus. The particles which possess a smaller parallel velocity compared to their perpendicular velocity are trapped on the low field side of the machine as illustrated in Figure 2.6. Their trajectory is called *bananas*. This trapping occurs because of the combination of a gradient of the toroidal magnetic field with the magnetic field lines winding. At a given flux surface label (the minor radius in circular geometry), the magnetic field lines describe a spiral around the torus, covering alternatively larger major radius regions and smaller major radius regions. Due to the torus curvature and spatial expansion, the magnetic field is larger at smaller major radius. In the circular geometry illustrated in Figure 2.4, the expression of the toroidal magnetic field as a function of r is: $B = B_0/(1 + \epsilon\cos\theta)$ where $\epsilon = r/R$ is the inverse aspect ratio[3].

The total energy $E = mv^2/2 + e\phi$ of a particle being conserved[4] and the magnetic moment being an adiabatic invariant, the trapping condition is $v_\parallel^2 \leq 0$. Expressing the parallel and perpendicular components of v: $v^2 = v_\parallel^2 + v_\perp^2 = v_\parallel^2 + 2\mu B/m$ leads to the following trapping condition:

$$v_{\parallel\max}^2(r) \leq \frac{2}{m}(E - e\phi(r,\pi) - \frac{\mu B_0}{1+\epsilon}) \tag{2.11}$$

Since tokamak plasmas are strongly magnetized ($\mu B \gg e\phi$) one can assume as a first estimate that the variation of ϕ is negligible. Then the trapping condition reduces to:

$$v_{\parallel\max}^2(r) = v_\parallel^2(r,0) \leq \frac{2\mu B_0}{m}\frac{2\epsilon}{(1+\epsilon)(1-\epsilon)} = v_\perp^2(r,0)\frac{2\epsilon}{1-\epsilon} \tag{2.12}$$

This defines the *trapping cone*. The variation of ϕ is in fact negligible because ϕ does not vary over a flux surface in the absence of strong parallel flow. In the case of a strong parallel flow, the density is not a flux function due to centrifugal force effects as explained in Casson et al. [2010]. The variations of the potential ϕ follow the density variations as $n_e = e\phi/T_e$. In that case, the variations of ϕ are substantial and widen the trapping cone[see Casson et al., 2010, Figure 3].

2.2.2 Introduction to gyro-kinetic theory

As explained in the previous paragraph, the particle motion can be simplified under the *adiabatic theory* assumptions. However, when dealing with the entire plasma, the number of coupled equations — the Klimontovitch equations – to track all particles is completely intractable.

[3] Applying Ampere's law over circle in the equatorial plane of the tokamak gives $B(R) = B_0R_0/R = B_0/(1 + r/R_0\cos\theta$ in the circular geometry where θ is the poloidal angle

[4] The conservation of the total energy of a particle derives from the fundamental law of dynamics applied to a charged particle. Taking the scalar product with $\mathbf{v}$ leads to: $\mathrm{d}_t(m_sv^2) = -e_s\mathbf{v}\cdot\nabla\phi$. For static fields $\mathrm{d}_t = \mathbf{v}\cdot\nabla\phi$

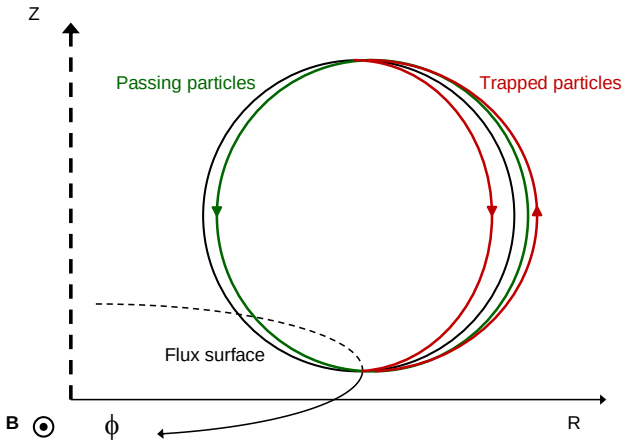

Figure 2.6: Poloidal cut of a tokamak plasma. In green, a sketch of a passing particle trajectory; in red, of a trapped particle

To overcome this issue, the *kinetic* theory enables the reduction of the problem dimension to 6 dimensions by considering a phase space composed of the positions $\mathbf{q}$ (3 dimensions) and the momenta $\mathbf{p}$ (3 other dimensions). The statistical information over the spatial localisation of all the particles and their momentum is then represented by a single six-dimensional function: the probability distribution function (PDF). The PDF corresponds to the probability to find a particle at a given position $\mathbf{q}$ with a given momentum $\mathbf{p}$. However complete and somewhat more tractable than the Klimontovitch equation, a kinetic description of tokamak plasmas is still too costly in terms of computational time. Indeed, due to the strong magnetisation of the plasma, the time scales to treat range from a fraction of the electron cyclotron time ($\sim 10^{-11}$s) to the energy confinement time ($\sim$ 1s) and the spatial scales range from a fraction of the electron Larmor radius ($\sim 10^{-5}$m) to the small radius of the machine ($\sim$ 1m).

For micro-turbulence studies in tokamak plasmas, the interest is on frequencies larger than the cyclotron frequencies since the frequency of the drifts previously introduced are well above the cyclotron frequency, as explained in the following. The reduction of scales is done in the same manner as for the simplification of the particle motion study of § 2.2.1.2 by averaging over the cyclotron motion. Only the "slow" gyro-centre motion is then studied. Thereby the 6D model can be reduced to a 5D model provided that certain orderings are respected. These orderings are based on experimental observations of tokamaks micro-turbulence.

2.2.2.1 Gyro-kinetics orderings

The key dimensionless parameter of the gyro-kinetic ordering is: $\rho_{*s} = \rho_c/a$ the thermal Larmor radius normalized to the tokamak minor radius. In tokamaks, the normalized Larmor radius is a small quantity: for electrons $\rho_{*e} < 10^{-4}$ and for ions $\rho_{*i} < 10^{-2}$ for $T = 1$ keV and $a = 1$ m. ρ_{*i} defines the parameter $\varepsilon \ll 1$. The gyro-kinetic approximation is based on the assumption of three frequency scales:

- the fast cyclotron motion of typical frequency ω_c;
- an intermediate frequency typical of the turbulent fluctuation dynamics $\omega \sim \frac{v_{Ts}}{L} \sim \varepsilon\omega_c$;
- a long time scale characteristic of the macroscopic transport $\omega_{\text{tr}} \sim \varepsilon\omega$.

In practice L stands for the shortest gradient length: $T/\left|\nabla_r T\right|$ since it is a spatial scale of greater importance than the tokamak minor radius for transport processes.

The intrinsic anisotropy of the tokamak geometry is also taken into account. Since the direction parallel to the magnetic field is essentially a free direction of motion whereas the perpendicular direction is much constrained by the magnetic nest, the structures that develop in tokamak plasmas are much more elongated in the parallel direction. In mathematical terms this translates to: $k_\parallel \ll k_\perp$ where $k_\parallel$ is the component of the wave vector parallel to the field lines and $k_\perp$ is the perpendicular component of the wave vector of the structures at hand.

Assumptions on the fluctuation amplitudes are also made. Namely:

- the fluctuations of the potential energy $e_s\tilde{\phi}$ is much smaller than the kinetic energy: $e_s\tilde{\phi} \sim \varepsilon T$;
- the density perturbations are much smaller than the equilibrium density $\tilde{n_s} \sim \varepsilon n_s$;
- the magnetic field fluctuations are much smaller than the equilibrium field $\delta B \sim \varepsilon B_0$.

In the following additional approximations will be made. Among them, the ratio β of the kinetic pressure to the magnetic pressure is supposed much smaller than unity: in conventional tokamak plasmas it is of the order of a few percent. The magnetic fluctuations are therefore neglected even if this simplification can be subject to debates for core plasma simulations (in particular for high-β conditions and is inappropriate for edge plasma simulations[Snyder and Hammett, 2001, Pueschel, 2009, Citrin et al., 2013].

2.2.2.2 The gyro-kinetic approximation

With the orderings of § 2.2.2.1, the low frequency perturbations affect only the guiding centre dynamics while the magnetic moment is an adiabatic invariant. A scale separation is

therefore possible between the fast gyro-motion and the slower dynamics of guiding centre. The position of the guiding centre is however a function of the particle velocity. Thus, there is no direct coordinate transform that connects the particle position with the guiding centre position nor their velocities.

In these new coordinates, the perturbed Hamiltonian corresponds to the energy of the gyro-centres [Brizard and Hahm, 2007, Garbet et al., 2010]:

$$h_s = \frac{1}{2} m_s v_{G\parallel}^2 + \mu_s B + e_s \phi + \mathcal{O}(\rho_{*s}^2) \tag{2.13}$$

At this point the Hamiltonian still depends on the gyro-angle φ_c. An average over φ_c is then performed corresponding to the sketch presented in Figure 2.5. The magnetic moment is considered as an exact invariant rather than an adiabatic invariant. At lowest order in ρ_*, the expression of the gyro-kinetic magnetic moment $\bar{\mu}$ is the same as μ_s but corrections at higher orders can be added to verify more accurately that $\mathrm{d}_t \bar{\mu} = 0$. For reasons explained in the next chapter this is not done here. The gyro-kinetic Hamiltonian then reads:

$$\bar{h}_s = \frac{1}{2} m_s v_{G\parallel}^2 + \mu_s B + e_s J_0 \cdot \phi \tag{2.14}$$

where the gyro-average operator J_0 is defined by $J_0 \cdot \phi = \oint \phi \mathrm{d}\varphi_c / 2\pi$. We stress that the gyro-average operator does not suppress the information about the variation of the fields at the Larmor radius scale. The gyro-centre is therefore to be understood as a current ring of the size of the Larmor radius rather than a pseudo-particle travelling at the guiding centre position [Abiteboul, 2012].

The equation governing the evolution of gyro-centre distribution function ($\bar{f}_s$) is therefore a 5D equation which can be expressed in the Hamiltonian formalism:

$$\mathrm{d}_t \bar{f}_s = \partial_t \bar{f}_s + \left[\bar{f}_s, \bar{h}_s\right] = \mathcal{C}\left(\bar{f}_s\right) \tag{2.15}$$

where $[\cdot, \cdot]$ is the Poisson bracket in the gyro-centre coordinates which is expressed in § 2.2.3 with action-angle variables. The RHS of (2.15) represents the gyro-averaged collision operator. Electron-ion collisions are especially important for the correct treatment of the trapped electrons dynamics. The ion-ion collisions have a smaller effect due to their lower frequency. The details of the collision operator implementation in QuaLiKiz are given in the next chapter § 3.3. For now, this term is neglected for simplicity since it does not change the discussion to come on invariants.

2.2.2.3 Electro-neutrality in gyro-kinetics

In (2.15), the system must be closed by an additional equation for the electric potential. In the general case, in the low-β limit, ϕ is obtained by Poisson equation:

$$\nabla^2 \phi = -\frac{1}{\epsilon_0} \sum_s e_s n_s \tag{2.16}$$

where ϵ_0 is the vacuum permittivity. Using the electron Debye length: $\lambda_{De} = \sqrt{\epsilon_0 T_e/(e^2 n_0)}$, (2.16) reads:

$$\lambda_{De}^2 \nabla^2 \left(\frac{e\phi}{T_e} \right) = -\frac{1}{n_0} \sum_s e_s n_s \tag{2.17}$$

In fusion plasmas, the electron Debye length is orders of magnitude lower the ion Larmor radius. Considering the orderings previously presented and the gyro-average performed to obtain (2.15), the left hand side of (2.17) is negligible. As a result, the plasma can be considered *quasi-neutral* at the scales considered by the gyro-kinetic model. This is consistent with the usual interpretation of the Debye length corresponding to the characteristic scale at which the charges of the particles are shielded. Poisson equation is therefore replaced by the quasi-neutrality condition:

$$\sum_s e_s n_s = 0 \tag{2.18}$$

2.2.3 Linearised gyro-kinetics in action-angle variables

In the previous sections the general form of the gyro-kinetic equation was introduced. For the sake of clarity and concision no more details will be given on the general case and the curious reader is referred to reviews[Brizard and Hahm, 2007, Garbet et al., 2010] and PhD thesis [Abiteboul, 2012] on the subject. Instead, the simplified case of the linearised gyro-kinetic equation used in the following is derived here.

2.2.3.1 The linearised gyro-kinetic equation in angle-action variable

Let us start by reminding the expression for the *guiding-centre* Hamiltonian in the low-β (or equivalently the electrostatic) limit:

$$h_s = \frac{1}{2} m_s v_{g\parallel}^2 + \mu_s B + e_s \phi \tag{2.19}$$

Hamilton's equations

Since there are three motion invariants (μ_s,E,p_φ), a system of variables can be constructed such that Hamilton's equations are expressed as:

$$\begin{aligned} \mathrm{d}_t \mathbf{J} &= -\partial_{\boldsymbol{\alpha}} h = 0 \\ \mathrm{d}_t \boldsymbol{\alpha} &= \partial_{\mathbf{J}} h = \boldsymbol{\Omega}_{\mathbf{J}} \end{aligned} \tag{2.20}$$

where ($\boldsymbol{\alpha}$,$\mathbf{J}$) is the angle-action system. The three actions J_i correspond to the normalized invariants:

$$J_1 = -\frac{m_s \mu_s}{e_s} = \frac{m_s^2 v_\perp^2}{2 e_s B_G} \tag{2.21a}$$

$$J_2 \equiv E = \frac{1}{2} m_s v_{G\parallel}^2 + \mu_s B + e_s \phi \tag{2.21b}$$

$$J_3 = M = e_s \psi + m_s R v_{G\varphi} \tag{2.21c}$$

Derivation of the resonant frequencies

Three frequencies are associated to the three invariants defined in (2.21). Ω_1 is the cyclotron frequency. The second frequency corresponds to the motion of particles around the torus: the transit frequency for passing particles and the bounce frequency for trapped ones. As indicated earlier, the poloidal angle measures a distance in the parallel direction for a given field aligned toroidal angle ζ. Ω_2 therefore corresponds to $\oint \mathrm{d}_t\theta$ where $\oint$ means $\int_{-\pi}^{\pi}$ for passing particles and (approximatively) $2\int_{-\theta_0}^{\theta_0}$ for trapped particles. Without taking the guiding centre drifts into account and using the expression (2.19) for the energy, one gets:

$$\mathrm{d}_t\theta = J(\psi,\theta) v_\parallel = \pm v_{Ts} J(\psi,\theta) \sqrt{\xi(1-\lambda b(\psi,\theta))} \tag{2.22}$$

where $\xi = (h_0 - e_s\phi)/T_s$ is the normalized kinetic energy, $\lambda = \mu_s B(\psi,0)/(h_0 - e_s\phi)$ is the pitch-angle and $b(\psi,\theta) = B(\psi,\theta)/B(\psi,0)$ corresponds to the poloidal variation of the magnetic field. $J(\psi,\theta) = \mathbf{B}\cdot\nabla\theta/B$ is the Jacobian of the rotational transform. In the circular geometry used in QuaLiKiz, $J = 1/(qR)$. Ω_2 finally reads:

$$\Omega_2 = \epsilon_\parallel v_{Ts} \sqrt{\xi} \bar{\omega}_2(\psi,\lambda) \tag{2.23}$$

where $\bar{\omega}_2$ is defined by

$$\bar{\omega}_2^{-1} = \oint \frac{\mathrm{d}\theta}{2\pi} \frac{1}{J\sqrt{1-\lambda b(\psi,\theta)}} \tag{2.24}$$

The third frequency corresponds to the guiding-centre drifts across the field lines. Therefore we make use of the field aligned coordinate $\zeta = \varphi - q(\psi)\theta$. The derivation in the general geometry case, somewhat tedious, does not bring many insight and is not performed here [see Garbet et al., 1990, for a general expression]. In the simplified circular geometry presented in Figure 2.4, $\psi = rBR/q$ and $\mathrm{d}_t\zeta$ can be expressed as:

$$\mathrm{d}_t\zeta = -\frac{q v_{ds}}{r}\left(\cos\theta + (\hat{s}\theta - \alpha\sin\theta)\sin\theta\right) - \frac{q v_{E\theta}}{r} \tag{2.25}$$

where v_{ds} is the norm of $\mathbf{v}_{ds}$ expressed in (2.9) projected on the radial and poloidal directions and $v_{E\theta}$ is the projection of $\mathbf{v_E}$ on the poloidal direction.

Hence $\Omega_3 = \oint \mathrm{d}\theta \mathrm{d}_t\zeta$ can be expressed as:

$$\Omega_3 = \frac{qE_r}{rB} - \frac{qT_s}{e_s BRr}\bar{\omega}_2 \oint \frac{\mathrm{d}\theta}{2\pi} \frac{(2-\lambda b)\left(\cos\theta - (\hat{s}\theta - \alpha\sin\theta)\sin\theta\right)}{\sqrt{1-\lambda b(r,\theta)}} \tag{2.26}$$

Note that in the large aspect ratio *i.e.* $r/R = \epsilon \ll 1$, the normalized magnetic field is expressed as $b(\psi,\theta) = 1 + \epsilon(1-\cos\theta)$. With this approximation, the frequencies Ω_2 and Ω_3 can be expressed analytically.

Linearised Vlasov equation

Now that the three frequencies have been derived, the Poisson bracket from (2.15) can be expressed as:

$$[f,h] = \partial_{\boldsymbol{\alpha}} f \partial_{\mathbf{J}} h - \partial_{\mathbf{J}} f \partial_{\boldsymbol{\alpha}} h \tag{2.27}$$

Having three invariants $\mathbf{J}$ is equivalent to having periodicity over their associated angle $\boldsymbol{\alpha}$. Thus, the Hamiltonian and the distribution function are developed in Fourier series:

$$h(\boldsymbol{\alpha},\mathbf{J},t) = h_0(\mathbf{J},t) + \sum_{\mathbf{n},\omega} \tilde{h}_{\mathbf{n},\omega}(\mathbf{J})\, e^{\imath(\mathbf{n}\cdot\boldsymbol{\alpha}-\omega t)} \tag{2.28a}$$

$$f(\boldsymbol{\alpha},\mathbf{J},t) = f_0(\mathbf{J},t) + \sum_{\mathbf{n},\omega} \tilde{f}_{\mathbf{n},\omega}(\mathbf{J})\, e^{\imath(\mathbf{n}\cdot\boldsymbol{\alpha}-\omega t)} \tag{2.28b}$$

The equilibrium distribution function f_0 and the unperturbed Hamiltonian h_0 are independent of $\boldsymbol{\alpha}$ by construction of the angle-action system.

Linearising the Vlasov equation $\mathrm{d}_t f = 0$ gives:

$$\partial_t f + \partial_J h_0 \partial_{\boldsymbol{\alpha}} \tilde{f} - \partial_J f_0 \partial_{\boldsymbol{\alpha}} \tilde{h} = 0 \tag{2.29}$$

Using the Fourier representation of (2.28) to express the derivatives with respect to $\boldsymbol{\alpha}$ leads to:

$$\tilde{f}_{\mathbf{n}\omega} = \frac{-\mathbf{n}\cdot\partial_{\mathbf{J}} f_0}{\omega - \mathbf{n}\cdot\partial_J h_0 + \imath o^+} \tilde{h}_{\mathbf{n}\omega} \tag{2.30}$$

where $\mathbf{n}$ are the wave number associated to $\boldsymbol{\Omega} = \partial_{\mathbf{J}} h_0$.

n_1 is the wave number associated to the gyro-motion. Since Ω_2 corresponds to a poloidal frequency following a field line, n_2 can be identified with m the *poloidal* wave number and $n_2\Omega_2$ can also be seen as the transit frequency $k_\parallel v_\parallel$. We will see that depending on the nature of the particle trajectory around the torus, either notation can be preferred. Ω_3 is the frequency associated with the drifts of the guiding centre with respect to the field lines. Thanks to the rotational transformed created by the induction of a toroidal electrical current in the plasma (represented by q), the drifts are pushed in the toroidal direction. Therefore Ω_3 is a toroidal precession frequency and n_3 can be identified to the *toroidal* wave number n.

In (2.30), o^+ is a small positive quantity. Indeed, a small imaginary quantity is needed for the analytical continuation of (2.30) when ω crosses the real axis. From the mathematical point of view either a positive or negative value is acceptable. However the physical consequences of this choice impose a positive value. Choosing a positive value leads to exponentially growing waves whereas a negative value means exponentially decaying waves. The later solution is in contradiction with the *causality* principle which states that any physical phenomenon originates from a cause and therefore any wave should be vanishing at $t \to -\infty$. This is known as the *Landau prescription* as it was first formulated by Lev Landau in [Landau, 1946].

We stress that (2.30) is a kinetic equation rather than gyro-kinetic. Applying the gyro-average operator makes the gyro-frequency vanish in (2.30) and introduces Bessel functions as explained in the next chapter.

2.2.3.2 The linearised gyro-kinetic electro-neutrality

The electro-neutrality equation is now used to close the linear system of equations defined by (2.30). To take the action of the perturbed electromagnetic field into account, a variational form of the electro-neutrality is used in the spirit of what is done in quantum mechanics when dealing with particle ensembles[Mermin, 1965]. The functional $\mathcal{L}_s(\omega) = \sum_{\mathbf{n}\omega} \bar{\rho}_s \mathrm{d}\mathbf{J}$ is minimised with respect to the perturbed electromagnetic potential[5], $\bar{\rho}_s = e_s \bar{n}_s$ being the gyro-averaged charge density. In the low-β limit, the fluctuations of the magnetic field are assumed negligible compared to the fluctuations of the electrostatic potential. Therefore, the functional $\mathcal{L}_s$ is minimised with respect to the Hermitian transpose of the electrostatic potential $\bar{\phi}^*$ only:

$$\partial_{\bar{\phi}^*} \sum_s \mathcal{L}_s = 0 \tag{2.31}$$

The condition (2.31) is assured by its weak form:

$$\sum_s \mathcal{L}_s \bar{\phi}^* = 0 \tag{2.32}$$

Since $\bar{n_s}$ is given by (2.30) and $\bar{\phi}^* = \tilde{\phi}^* \cdot J_0$, the gyro-kinetic electro-neutrality is expressed as follows in the variational form:

$$\sum_{s,\omega} e_s^2 \int J_0 \cdot \frac{-\mathbf{n} \cdot \partial_{\mathbf{J}} f_{0s}}{\omega - \mathbf{n} \cdot \partial_{\mathbf{J}} h_0 + \imath o^+} J_0 \cdot \left|\tilde{\phi}_{\mathbf{n}\omega}\right|^2 \mathrm{d}\mathbf{J} \frac{\mathrm{d}\boldsymbol{\alpha}}{(2\pi)^3} = 0 \tag{2.33}$$

Applying the gyro-averaged operator J_0 on the linear plasma response — $\frac{-\mathbf{n}\cdot\partial_{\mathbf{J}} f_{0s}}{\omega - \mathbf{n}\cdot\partial_{\mathbf{J}} h_0 + \imath o^+}$ — is equivalent to consider only the term $n_1 = 0$. Therefore, only $m\Omega_2$ and $n\Omega_3$ remain as possible resonances for the system described by (2.33). For the perturbed potential, taking

[5] This approach is somewhat more profound than a simple electro-neutrality condition since it describes the plasma self-organisation and can be linked to the principle of least action

only the term $n_1 = 0$ is equivalent to perform the integral over α_1: it can be described intuitively by an average in real space over the gyro-angle[6]:

$$J_0 \cdot \tilde{\phi}_{\mathbf{n}\omega}(\mathbf{J}) = \oint \frac{\mathrm{d}\varphi_c}{2\pi} \tilde{\phi}_{n_2,n_3,\omega}(J) \exp\left(-\imath \mathbf{n}_1 \cdot \boldsymbol{\alpha}_1\right) \tag{2.34}$$

n_1 is the wave vector associated to the gyro-motion for any position of the guiding-centre. Therefore, $n_1 \equiv k_\perp \rho_c$. $\boldsymbol{\alpha}_1$ corresponds to the gyro-angle $\boldsymbol{\varphi}_c$. Defining the gyro-averaged potential $\bar{\phi}_{\mathbf{n}\omega} = \tilde{\phi}_{n_2,n_3,\omega}(J)$, (2.34) is expressed as:

$$J_0 \cdot \tilde{\phi}_{\mathbf{n}\omega}(\mathbf{J}) = \bar{\phi}_{\mathbf{n}\omega} \oint \frac{\mathrm{d}\varphi_c}{2\pi} \exp\left(\imath \left(k_r \rho_c \cos\varphi_c + k_\theta \rho_c \sin\varphi_c\right)\right) \tag{2.35}$$

The result is projected on the circular geometry for simplicity but is valid on any magnetic geometry when using flux coordinates. The integral $\oint \frac{\mathrm{d}\varphi_c}{2\pi} \exp\left(\imath \left(k_r \rho_c \cos\varphi_c + k_\theta \rho_c \sin\varphi_c\right)\right)$ is the zero order Bessel function of the first kind $J_0(k_\perp \rho_c)$.

The equilibrium distribution function f_0 in (2.33) is still not determined. The equilibrium Valsov equation $\partial_t f_0 + [f_0, h_0] = 0$ is used for its determination. The determination of the equilibrium distribution used for this work is performed in chapter 3 because the equilibrium plasma density is assumed to be a flux function in this work which represents a loss of generality for this chapter. The reasons for this approximation and its consequences are also discussed in the next chapter.

Equation (2.33) is an eigenvalue/eigenfunction equation that should be solved consistently. In the next chapter, we will see that it is not carried out in QuaLiKiz to gain two orders of magnitude in CPU time, making the code compatible with an integrated modelling framework. Instead, the eigenfunctions are solved analytically in the so-called *hydrodynamic limit* [Sarazin, 2008]. Their expression is derived and they are compared to self-consistent gyro-kinetic eigenfunctions in § 3.2. The resulting eigenvalues ω — in particular the growth rates $\Im(\omega)$ — are studied in § 3.3.2 and compared to the results of self-consistent gyro-kinetic simulation performed with GKW [Peeters et al., 2009b].

[6] Averaging over the gyro-angle corresponds to the historic views of gyro-kinetic theory. In modern gyro-kinetic theory, the removal of gyro-angle dependences is performed through Lie transforms as derived by Littlejohn [1981] [see Brizard and Hahm, 2007, for a review]

3

QuaLiKiz framework for micro turbulence study

The goal of this chapter is to present in details the linear solver at the heart of the quasi-linear gyro-kinetic code QuaLiKiz[Bourdelle et al., 2002, 2007] used and expanded in this work, the saturated potential being presented in the next chapter.

The objectives of the code are first presented, explaining the various approximations performed in the following and used in QuaLiKiz. Then the electro-neutrality equation used in QuaLiKiz is based on the relation (2.33) derived in the previous chapter. The choice of the equilibrium distribution function is presented and justified. The consequences of this choice are also discussed briefly in § 3.1.2 (and illustrated in § 3.3.2.2).

The analytical model employed to determine the fluctuating potential $\bar{\phi}$ is latter derived. The *hydrodynamic* limit — $\omega \gg \Omega_{2,3}$ — is used to develop the resonant terms in power series of $\Omega_{2,3}/\omega$ and the short wavelength limit is taken allowing for a linearisation of the Bessel functions. The eigenfunctions are shown to be shifted Gaussian in this limit. The width of the Gaussian is linked to the balance between the instability drive and the parallel motion connecting more stable (HFS) and more unstable regions (LFS). The shift is proportional to the quantities breaking the parallel symmetry $(\alpha, v_\parallel) \to (-\alpha, -v_\parallel)$ of (2.33). Given the assumptions on the equilibrium distribution function (see § 3.1.2) and the circular geometry used in QuaLiKiz, the following quantities act as symmetry breakers:

- The parallel velocity $u_\parallel$;
- The parallel velocity gradient $\nabla u_\parallel$;
- The $\mathbf{E} \times \mathbf{B}$ velocity shear rate γ_E.

In QuaLiKiz, the magnetic equilibrium is the circular $\hat{s} - \alpha$ equilibrium, w.r.t. the poloidal mid-plane. Therefore, the mechanisms driving momentum transport via an *up-down asymmetry* [Camenen et al., 2009b] cannot be studied here. The tokamak is also considered

axisymmetric. The variation of the toroidal magnetic field (or *ripple*) is not treated by the present work although it can be important is certain tokamaks such as Tore Supra (the tokamak in operation for 25 years in Cadarache, Southern France).

The eigenfunctions are compared to the self-consistent eigenfunctions of the gyro-kinetic code GKW[Peeters et al., 2009b] run in its linear version both without and with symmetry breakers.

Finally, the linear growth rates are also compared to linear gyro-kinetic simulations with GKW.

3.1 From linearised gyro-kinetic theory to a fast solver: QuaLiKiz

3.1.1 The time constraint of integrated modelling

The goal of QuaLiKiz is to predict the turbulent fluxes of particles, heat (of ions and electrons) and angular momentum with sufficient accuracy for an analysis of the various experimental parameter effects on the confinement. Another goal is to be integrated into modelling platforms to performed predictive simulations of current and future experiments. This kind of modelling uses the scale separation between the equilibrium quantities and the fluctuations to evolve the profiles consistently with the sources (of particles, energy, momentum) and the fluxes (neoclassical and turbulent) calculated by separated codes. This implies numerous iterations for the codes calculating the fluxes — *i.e.* QuaLiKiz for the turbulent fluxes — which depend on the equilibrium profiles.

Being compatible with integrated modelling implies that QuaLiKiz must be run quickly for acceptable simulation times. In order to compute the turbulent thresholds more precisely and better reproduce parametric dependences close to the threshold, a gyro-kinetic approach is chosen as opposed to a fluid one. The increased accuracy of this framework is at the cost of CPU time, making it incompatible with the code objectives without further simplifications. As an illustration, a non-linear electrostatic gyro-kinetic simulation requires $\sim$ 5,000 CPU hours for a radius. For integrated simulation $\sim$ 20 radii and 10,000 calls to the code are needed to model one second of plasma because of non-linearities. This means $\sim$ 4,000 days on 1,000 processors. With QuaLiKiz, the cost is reduced to $\sim$ 4 days on 100 processors. Two orders of magnitude in CPU time are spared employed a quasi-linear approach rather than solving the full non-linear problem. Other two orders of magnitudes are gained by using the ballooning representation at lowest order to decrease the dimensionality of the problem and calculating the fluctuating potential $\bar{\phi}$ (*i.e.* the eigenfunctions) in the so-called *hydrodynamic* limit [Sarazin, 2008] allowing for analytic solutions of the fluctuating potential.

3.1.2 The choice of the equilibrium distribution function

As indicated in the previous chapter, the distribution function is split into an equilibrium distribution function evolving on the transport time scale (much slower than the phenomena studied) and a perturbed distribution function evolving on the studied time scales as indicated by (2.30). The equilibrium distribution function f_0 cannot be determined unequivocally by the framework presented in the previous chapter. f_0 chosen in agreement with the neoclassical theory which foresees that a Maxwellian distribution is reached at long time scales. f_0 must also verify the Vlasov equation to be compatible with the angle-action framework described in § 2.2.3:

$$\partial_t f_0 + [f_0, h_0] = 0 \tag{3.1}$$

A solution that ensures this property is for f_0 to be a function of the invariants of motion (μ,E,p_φ). A practical solution is to write $f_0 = n_s/(2\pi T_s/m_s)^{3/2}\exp(-E/T_s)$ where $E = h_0 - e_s\phi$ is the kinetic energy. However, such an equilibrium distribution function does not reproduce the equilibrium statistics of tokamak plasmas. Indeed, such f_0 does not allow for the equilibrium flows encountered in experiments. To take this possibility into consideration, the following probability distribution function is chosen for the species s of mass m_s, density n_s temperature T_s and thermal velocity $v_{Ts} = \sqrt{2T_s/m_s}$:

$$f_{0s} = \frac{n_s}{\left(2\pi T_s/m_s\right)^{3/2}} \exp\left(-\frac{\left(v_\parallel - u_\parallel\right)^2}{v_{Ts}^2} + \frac{\mu_s B}{T_s}\right) \tag{3.2}$$

which ensures that a non-vanishing equilibrium velocity $u_\parallel$ is possible since the equilibrium velocity is defined by $\int f_0 v_\parallel \mathrm{d}v_\parallel \mathrm{d}\mu = u_\parallel$. (3.2) is then written as a function of the Hamiltonian h_0.

$$f_{0s} = \frac{n_s}{\left(2\pi T_s/m_s\right)^{3/2}} \exp\left(-\frac{h_0 - e_s\phi}{T_s} + \frac{\left(2v_\parallel - u_\parallel\right)u_\parallel}{v_{Ts}^2}\right) \tag{3.3}$$

For the condition (3.1) to be respected, the densities n_s, temperatures T_s and velocity $u_\parallel$ must be functions of the invariants. In non-rotating plasmas, this is respected because the densities and temperatures are flux functions: $n_s = n_s(\psi)$ and $T_s = T_s(\psi)$. In this case $\psi = J_3/e_s$ since $e_s\psi \ll m_s R v_\varphi$. However, for $u_\parallel/v_{Ti}$ close to unity, a poloidal asymmetry of density develops due to centrifugal effects[Casson et al., 2010]. Therefore, the chosen equilibrium function is not adapted to highly rotating plasmas encountered in small aspect ratio — *spherical* — tokamaks[Roach et al., 2009]. The consequences of this choice on the linear growth rates are studied in § 3.3.2. In conventional tokamaks however, the rotation remains under $u_\parallel = 0.5 v_{Ti}$ and under $u_\parallel = 0.2 v_{Ti}$ in most cases. Within this range of parallel equilibrium flows, the assumption $n_s = n_s(\psi)$ is valid. Other approximations performed in QuaLiKiz such as the low-β approximation fail in the conditions encountered in spherical tokamaks where β is typically of several percent and, most importantly, QuaLiKiz

uses $\epsilon = r/R$ expansions based on large aspect ratio assumptions to keep most integrals analytical.

The $\hat{s}-\alpha$ equilibrium used in QuaLiKiz is also not well suited to model shaped plasma encountered in many tokamaks. In order to circumvent this issue, a more flexible equilibrium is planned on being implemented in QuaLiKiz.

The derivative of this distribution function with respect to the invariants is therefore:

$$\begin{aligned}\partial_{\mathbf{J}} \ln(f_0) =& \partial_{J_3} \ln(n_s) + \left(\xi - \frac{3}{2} - \frac{u_\parallel(2v_\parallel - u_\parallel)}{v_{Ts}^2}\right) \partial_{J_3} \ln(T_s) + 2\frac{v_\parallel - u_\parallel}{v_{Ts}^2}\partial_{J_3} u_\parallel + \\ & \frac{u_\parallel}{v_{Ts}^2}\partial_{p_\varphi} v_\parallel - \frac{1}{T_s}\partial_{\mathbf{J}} h_0 + \frac{e_s}{T_s}\partial_{J_3}\phi = \frac{1}{T_s}\left(\omega_E + \Omega^* - \partial_J h_0\right)\end{aligned} \tag{3.4}$$

since n_s, T_s and $u_\parallel$ are functions of J_3 only. $\xi = (h_0 - e_s\phi)/T_s$ is the normalized kinetic energy.

For the derivative with respect to J_3, a simplification is possible since $e_s\psi \gg m_s R v_\varphi$ in the large aspect ratio tokamak conditions. Indeed, in the $\hat{s} - \alpha$ equilibrium used in QuaLiKiz, the ratio of the quantities reads:

$$\frac{mRv_\varphi}{e_s\psi} = \frac{q}{r/a}\rho_{*s}\epsilon_\parallel\sqrt{\xi(1-\lambda b)} \tag{3.5}$$

where the normalized Larmor radius ρ_{*s} is a small quantity according to the gyro-kinetic ordering (see § 2.2.2.1) and $\epsilon_\parallel = \pm 1$ to account for both directions of circulation around the torus. Therefore, $\partial_{p_\varphi} \approx 1/e_s\partial_\psi$ for quantities primarily dependent on ψ such as n_s, T_s, $u_\parallel$ and ϕ. In contrast, $v_\parallel$ is essentially a function of v_φ. In this case, $v_\parallel$ is expressed at first order in ρ_{*s} as a function of J_3 using (3.5):

$$\partial_{p_\varphi} v_\parallel \approx \partial_{p_\varphi} \frac{q\rho_{*s}}{m_s Rr/a} p_\varphi = \frac{q\rho_{*s}}{m_s Rr/a} \tag{3.6}$$

Let us now introduce the generalized diamagnetic frequency $\mathbf{n}\cdot\mathbf{\Omega^*} = T_s\left(\mathbf{n}\cdot \mathrm{d}_{\mathbf{J}} \ln(f_0) + \mathbf{n}\cdot \mathrm{d}_{\mathbf{J}}\xi\right)$ in (2.33) which becomes:

$$\sum_{s,\omega} \frac{e_s^2 f_{0s}}{T_s} \int 1 - J_0 \cdot \frac{\omega - n\omega_E - \mathbf{n}\cdot\mathbf{\Omega^*}}{\omega - \mathbf{n}\cdot\partial_{\mathbf{J}} h_0 + \imath o^+} J_0 \cdot \left|\tilde{\phi}_{\mathbf{n}\omega}\right|^2 \mathrm{d}\mathbf{J} \frac{\mathrm{d}\boldsymbol{\alpha}}{(2\pi)^3} = 0 \tag{3.7}$$

where $\omega_E = \partial_\psi\phi = q/(rB)\partial_r\phi$ in $\hat{s} - \alpha$ geometry since $\psi = rRB_\theta$. The diamagnetic frequency Ω^* can be expressed as a function of the normalised gradients of density $R/L_{ns} = -R\partial_r \ln n_s$, temperature $R/L_{Ts} = -R\partial_r \ln T_s$ and velocity $R/L_u = -R/v_{Ts}\partial_r u_\parallel$:

$$\mathbf{n}\cdot\mathbf{\Omega^*} = n\bar{\omega}_{ds}\left[\frac{R}{L_{ns}} + \left(\xi - \frac{3}{2} - \frac{u_\parallel(2v_\parallel - u_\parallel)}{v_{Ts}^2}\right)\frac{R}{L_{Ts}} + \frac{2\left(v_\parallel - u_\parallel\right)}{v_{Ts}}\frac{R}{L_u}\right] \tag{3.8}$$

where the reference drift frequency $\bar{\omega}_{ds} = qT_s/(e_s rBR)$ is defined.

As discussed in the previous chapter, applying the gyro-average operator J_0 is equivalent to consider only the term $n_1 = 0$ in (3.7). As a result, the gyro-kinetic electro-neutrality equation is multiplied by the Bessel $J_0(k_\perp \rho_s)$:

$$\sum_{s,\omega} \frac{e_s^2 n_s}{T_s} \int \exp\left(-\xi + \frac{u_\parallel(2v_\parallel - u_\parallel)}{v_{Ts}^2}\right)\left(1 - \frac{\omega - n\omega_E - \mathbf{n}\cdot\mathbf{\Omega^*}}{\omega - n_2\Omega_2 - n_3\Omega_3 + \imath o^+}\right)\left|\bar{\phi}_{\mathbf{n}\omega}\right|^2 J_0^2(k_\perp\rho_{cs})\mathrm{d}\lambda\mathrm{d}\xi\mathrm{d}\theta\mathrm{d}\zeta = 0 \tag{3.9}$$

where ζ is the parallel (field aligned) coordinate and θ is the poloidal angle (along the field lines). Let us recall that $n_3\Omega_3 = n\omega ds + n\omega_E$ (see relation (2.26) in the previous chapter). Therefore, the previous can be written as a function of $\varpi = \omega - n\omega_E$ keeping in mind that ϖ has a radial electric field velocity:

$$\sum_{s,\omega} \frac{e_s^2 n_s}{T_s} \int \exp\left(-\xi + \frac{u_\parallel(2v_\parallel - u_\parallel)}{v_{Ts}^2}\right)\left(1 - \frac{\varpi - \mathbf{n}\cdot\mathbf{\Omega^*}}{\varpi - n_2\Omega_2 - n\omega_{ds} + \imath o^+}\right)\left|\bar{\phi}_{\mathbf{n}\omega}\right|^2 J_0^2(k_\perp\rho_{cs})\mathrm{d}\lambda\mathrm{d}\xi\mathrm{d}\theta\mathrm{d}\zeta = 0 \tag{3.10}$$

At this point, (3.10) is a two-dimensional eigenfunction/eigenvalue equation involving (r, θ) in real space due to the curvature of the magnetic field which prevents from a standard Fourier decomposition in $\bar{\phi}_{mn}(r)$ as it is possible in cylinders. The dimensionality of the problem is reduced via the so-called *ballooning representation* taken at lowest order. This is the subject of the next section.

Since the toroidal velocity is usually smaller than $0.4v_{Ti}$ in conventional tokamaks, the exponential in $u_\parallel$ in (3.10) is developed in power series up to the second order. Using the expansion has the benefit to allow for an analytic integration over ξ in (3.10) by using the plasma dispersion function. Another solution in order to have an analytic integration over ξ in (3.10) is to perform the variable transform $\xi = \mathcal{E} + 2u_\parallel v_\parallel / v_{Ts}^2$. The reformulation of (3.10) with this coordinate is however left for future work.

To keep an analytic integration over ξ in (3.10), the Bessel function $J_0(k_\perp\rho_s)$ is averaged over ξ. The ξ-dependence of the Bessel functions comes from $\rho_{cs} = \rho_s\sqrt{\xi\lambda b}$ where $\rho_s = \sqrt{2m_sT_s}e_sBR$ is the thermal Larmor radius of the species s. The average of J_0 over ξ is expressed by means of the modified Bessel function of the first kind I_0:

$$\int \mathrm{d}\xi J_0^2 k_\perp\rho_{cs} = \exp(-k_\perp^2\rho_s^2)I_0(k_\perp^2\rho_s^2) = \mathcal{B}_0(k_\perp\rho_s) \tag{3.11}$$

Once the equilibrium distribution function linearised in $u_\parallel$ and the Bessel function averaged in ξ, the linearised gyro-kinetic electro-neutrality equation used in QuaLiKiz can be written

as:

$$\sum_{s,\omega} \frac{e_s^2 n_s}{T_s} \int \left(1 + \frac{u_\parallel(2v_\parallel - u_\parallel)}{v_{Ts}^2} + \frac{u_\parallel^2}{v_{Ts}^2}\left(\frac{2v_\parallel^2}{v_{Ts}^2} - 1\right)\right) e^{-\xi} \left(1 - \frac{\varpi - \mathbf{n}\cdot\mathbf{\Omega}^*}{\omega - n_2\Omega_2 - n\omega_{ds} + \imath o^+}\right) \left|\bar{\phi}_{\mathbf{n}\omega}\right|^2 \frac{\mathrm{d}\lambda}{2\bar{\omega}_2} \mathrm{d}\xi \mathcal{B}_0(k_\perp \rho_s) \mathrm{d}\zeta \mathrm{d}\theta = 0 \tag{3.12}$$

The importance of the choice of the equilibrium distribution function is illustrated by (3.12). $\mathbf{n}\cdot\mathbf{\Omega}^*$, representing its sources terms, is directly linked to this choice. In a more physical view, the fluctuating distribution function $\bar{f}$ amplitude is considered much smaller than the equilibrium distribution function f_0. The choice of f_0 fixes therefore the thermodynamic state of the system *and* the fast event dynamics via the linear relation between the fluctuations and the equilibrium. Contrary to the implications of the choice made here, global *full-f* gyro-kinetic simulations find an excess of large energy events compared to Gaussian statistics [Abiteboul, 2012], suggesting that part of the turbulent transport processes is intermittent in core plasmas.

3.1.3 The ballooning representation

Aside from the considerations on turbulent transport dynamics and intermittency, the present section investigates the dimension reduction possible thanks to the symmetry properties of tokamaks.

In tokamaks, the Fourier modes of the electrostatic potential $\bar{\phi}_{mn}$ are strongly localised around resonant surfaces r_0 characterised by $n = mq(r_0)$. The radial extension of these modes allows for a coupling through the shearing of the magnetic field lines wielding $\hat{s}$ called *magnetic shear*. Using the anisotropy $k_\parallel \ll k_\perp$ induced by the strong toroidal magnetic field, the ballooning representation decouples the slow variation along the field lines from the fast variation in the perpendicular direction. The variation of the Fourier modes around the resonant surfaces at a typical scale of the distance between modes $d = 1/(k_\theta \hat{s})$ and the variation of the Fourier modes amplitude at a larger scale, typically of the order of the gradients length L_x [Connor et al., 1978, Pegoraro and Schep, 1981, Dewar and Glasser, 1983] is also separated using an eikonal representation:

$$\Phi_n(r,\theta,\varphi) = \bar{\phi}_n(r,\theta)\exp(-\imath n[\varphi - q(r)\theta]) \tag{3.13}$$

Assuming that q varies smoothly around the resonant surfaces r_0 where $q(r_0) \in \mathbb{Q}$, q is expanded in Taylor series at first order: $q(r) = q(r_0) + (r - r_0)/d$ where $d = 1/(nq') = 1/(k_\theta \hat{s})$ represents the distance between resonant modes. The ballooning representation consists in performing the following Fourier transform [Candy et al., 2004]:

$$\bar{\phi}_n(r,\theta) = \sum_p c_p(\theta,\theta_0)\exp(\imath(\theta_0 + 2\pi p)\frac{r - r_0}{d}) \tag{3.14}$$

The ballooning potential is introduced as

$$\hat{\phi}_n(\theta_p, \theta_0) = c_p(\theta, \theta_0) \exp(-\imath n q(r_0)(\theta_0 + 2\pi p)) \tag{3.15}$$

where $\theta_p = \theta + 2\pi p$. The fluctuating potential $\bar{\phi}_n$ can therefore be written as

$$\bar{\phi}_n(r, \theta) = \sum_p \int \frac{\mathrm{d}\theta_0}{2\pi} \hat{\phi}_{n\omega}(\theta_p, \theta_0) \exp\left(\imath(nq - m)(\theta_p - \theta_0)\right) \tag{3.16}$$

The ballooning angle θ_0 represents the direction of the largest wave vector of the modes in the poloidal plane. This angle varies in principle with the $\mathbf{E} \times \mathbf{B}$ velocity shear rate[Cooper, 1988, Miller and Waltz, 1994, Waltz et al., 1998]. According to global linear simulations finding that θ_0 is close to zero[Brunner et al., 1998], this angle is considered null allowing for a reduction of the dimension. It should be noticed that this constraint is greater in the presence of $\mathbf{E} \times \mathbf{B}$ shearing. In those simulations, the potential structures are shown to be sufficiently ballooned around the low field side mid-plane such that their poloidal extension is smaller than 2π. As the sum in p in (3.16) is there only to ensure the periodicity in θ, the expression of $\bar{\phi}$ can be limited to the term $p = 0$. Consequently, the p subscript is dropped in the following. The θ angle is therefore to be understood as an extended poloidal angle. This corresponds to the ballooning representation at the lowest order. In that case, no global envelope is considered. It is considered for each radius that the potential can be put under the form of a suite of identical modes.

In the general case of Equation (3.16), the only conclusion possible to draw is that $x = r - r_0 = \imath \frac{\mathrm{d}x}{n\mathrm{d}q} \partial_{\theta_0}$. Following the additional assumptions performed in the previous paragraph, the perpendicular and parallel wave vectors can be redefined. Since $\bar{\phi}(r, \theta, \varphi, t) = \sum_{n\omega} \hat{\phi}_{n\omega}(\theta) \exp(\imath n(\varphi - q(\theta - \theta_0)) - \imath\omega t)$:

$$\partial_r \bar{\phi} \equiv -\imath k_r \bar{\phi} \rightarrow -\imath n \frac{\mathrm{d}q}{\mathrm{d}r}(\theta - \theta_0)\hat{\phi} \tag{3.17a}$$

$$\partial_\theta \bar{\phi} \equiv -\imath k_\theta r \bar{\phi} \rightarrow -\imath n q \hat{\phi} \tag{3.17b}$$

There is therefore a relation between θ and k_r: $\theta - \theta_0 = k_r d$, with $\theta_0 = 0$ in QuaLiKiz. The poloidal wave number is also defined as $k_\theta = nq/r$.

The parallel wave number $k_\parallel$ is also defined. $\nabla_\parallel \bar{\phi} \equiv 1/(qR)\partial_\theta \hat{\phi}$ and ∂_θ is replaced by $1/d\partial_{k_r}$ in the ballooning representation. Now $\partial_{k_r} \rightarrow -\imath x$. Therefore, the parallel wave number is defined as:

$$k_\parallel = \frac{x}{qRd} = \frac{k_\theta \hat{s}}{qR} x \tag{3.18}$$

The scale separation on which is based the scale separation behind the eikonal transformation (3.13) is valid as long as the shortest gradient length L_x — typically L_T — is

large enough compared to the distance between resonant modes:

$$L_x \gg d \tag{3.19}$$

The condition (3.19) has proven to be correct for a wide range of parameters but fails at low magnetic shear ($\hat{s} < 0.1$) and low wave number conditions ($k_\theta \rho_s < 0.1$) due to the $(k_\theta \hat{s})^{-1}$ dependence of d, as shown in Citrin et al. [2012], Appendix C. The validity of (3.19) has to be proven for parallel and $\mathbf{E} \times \mathbf{B}$ velocity gradients since the equilibrium function used in this work allows them. If the velocity gradient scale length is defined as $L_u = \frac{v_{Ts}}{\nabla u_\parallel}$, it can reach values as small as $R/5$ for highly rotating core tokamak plasmas. The condition (3.19) then becomes $\epsilon \ll nqs/5$ where ϵ is the inverse aspect ratio. The latter condition specifies that (3.19) is valid down to $\hat{s} \geq 0.2$ and $n \geq 10$. For the $\mathbf{E} \times \mathbf{B}$ velocity shear, the condition of validity is satisfied for lower magnetic shear and toroidal wave numbers since $L_{\gamma_E} = v_{Ts}/\gamma_E = v_{Ts} B / \frac{dE_r}{\mathrm{d}r} > R$. The limitation is in fact essentially due to the loss of the locality condition (3.19) because of the divergence of the distance between modes d as the magnetic shear goes to zero. Therefore the limitations of this method are not different than the ones presented in Citrin et al. [2012]. The other limitation is the toroidal wave number condition $n \geq 10$ which is usually respected for micro-turbulence in tokamak plasmas developing at $k_\theta > 0.05/\rho_{ci}$. Incompatibilities are only found inside $r/a = 0.25$ for very low magnetic shear conditions $\hat{s} \geq 0.2$ for which large scale electromagnetic events such as sawteeth are possibly more important in term of plasma stability and transport.

The 1-D fluctuating potential $\hat{\phi}$ is now calculated using the reduced framework of the ballooning representation at lowest order. An analytic expression is derived in the so-called *hydrodynamic* limit. The resulting potential is later compared to the self-consistent gyro-kinetic eigenfunction of GKW [Peeters et al., 2009b] which uses Hamada's field align coordinates [Hamada, 1959] instead of the ballooning representation.

3.2 Trial eigenfunctions

To gain CPU time — 2 orders of magnitude together with the dimension reduction performed via the ballooning approximation formerly detailed — the fluctuating potential $\bar{\phi}$ is calculated in the hydrodynamic limit in which (3.10) can be solved analytically. The hydrodynamic limit consists in assuming that the frequency ω in (3.10) is much larger than the resonant frequencies $n_2\Omega_2$ and $n\omega_{ds}$ corresponding to the transit motion frequency and the curvature drift frequency respectively. This is a strong assumption since ω is essentially set by the resonant frequencies and collisions processes. Its validity will be discussed in the course of this chapter.

The eigenvalue/eigenfunction equation (3.10) is the starting point of the derivation. All previous approximations therefore apply, in particular the low Mach number approximation and the ballooning representation at lowest order.

3.2.1 Description of the reduced model for the eigenfunctions

Since the most relevant wave numbers for the transport phenomena linked to micro-turbulence are lower than $k_\theta \rho_i \approx 1$ [Dannert and Jenko, 2005], the model uses the short wavelength approximation where the Bessel functions coming from the gyro-average operator can be developed in power series:

$$\mathcal{B}_0(k_\perp \rho_i) \approx 1 - \frac{k_\perp^2 \rho_i^2}{2} \tag{3.20}$$

In that range, the passing electrons can be considered adiabatic *i.e.* they follow the fluctuations of the electrostatic potential without delay. Therefore, the resonant contribution from the passing electrons $(\omega - \mathbf{n}\cdot\mathbf{\Omega}^*)/(\omega - k_\parallel v_{\parallel,e})$ can be neglected. This is performed by separating the contributions from passing and trapped particles. This separation allows also for an average of the bounce motion of trapped particles. In the same spirit of the gyro-average, this leads to zero order Bessel functions of the first kind $\mathcal{B}_0(k_r\delta_s)$ as detailed in § 3.3. $\delta_s = q^2/(2\epsilon)\rho_s$ is the so-called banana width characterising the radial extent of the trapped particle motion. Both trapped ions and electrons are taken into account since they both contribute to the instabilities in the spectral range treated. The short wavelength approximation is also employed to develop the Bessel functions associated to the bounce motion.

All the simplifications done in (3.12) can be rewritten as a polynomial equation in ϖ:

$$\begin{aligned}
&\left[\frac{n_e}{T_e}\left(\left\langle 1-\left(1-\frac{n\omega_e^*}{\varpi}\right)\left(1+\frac{n\omega_{de}}{\varpi}\right)\right\rangle_t + f_p\right) + \right.\\
&\sum_i \frac{n_i Z_i^2}{T_i}\left\langle\left(1-\left(1-\frac{n\omega_i^*}{\varpi}\right)\left(1+\frac{n\omega_{di}}{\varpi}\right)\right)\left(1-\frac{k_r^2\delta_i^2}{4}\right)\right\rangle_t + \\
&\left.\sum_i \frac{n_i Z_i^2}{T_i}\left\langle\left(1-\left(1-\frac{n\omega_i^*}{\varpi}\right)\left(1+\frac{n\omega_{di}}{\varpi}+\frac{k_\parallel v_{\parallel i}}{\varpi}+\frac{k_\parallel^2 v_{\parallel i}^2}{\varpi^2}\right)\right)\left(1-\frac{k_\perp^2\rho_i^2}{2}\right)\right\rangle_p\right]\bar{\phi} = 0
\end{aligned} \tag{3.21}$$

The electro-neutrality condition $\sum_s e_s n_s = 0$ is used to reformulate (3.21). This enables for a species independent normalisation $n\bar{\omega}_d = n\bar{\omega}_{de} = -T_e/T_i n\bar{\omega}_{di}$.

In agreement with the assumption of ballooned turbulence around $\theta = 0$ made for the ballooning representation truncation, the curvature frequency of the passing particles is linearised in θ [see Romanelli et al., 2007, App. A]:

$$n\omega_{di} = -n\bar{\omega}_d\sqrt{\xi(2-\lambda b)}\left(\cos\theta - (\hat{s}\theta - \alpha\sin\theta)\sin\theta\right) \to n\bar{\omega}_d\sqrt{\xi(2-\lambda b)}\left(1-\left(\hat{s}-\alpha-\frac{1}{2}\right)\theta^2\right) \tag{3.22}$$

The thin banana approximation is used for trapped particles such that $n\omega_{de} = n\bar{\omega}_d\sqrt{\xi(2-\lambda b)}$. This is equivalent to consider that trapped particles are deeply trapped, the variation over the poloidal motion of the trapping parameter $\kappa = \sqrt{(1-\lambda)/(2\epsilon)}$ being neglected.

The relation $\theta = k_r d$ is used to express the passing particle curvature drift and an inverse Fourier transform $k_r \rightarrow -\imath\partial_x$ is performed leading to a second order differential equation.

It is important to recall here that ϖ includes the radial electric field velocity $n\omega_{\mathbf{E}\times\mathbf{B}}$. In order to make the role of the radial electric field shearing explicit, E_r is linearised: $E_r \rightarrow E_{r0} + E'_r x + O(x^2)$, assuming its radial dependence is smooth enough to neglect higher order derivatives. ϖ is changed into $\omega - k_\theta\gamma_E x$ where $\gamma_E = E'_r/B$ is the radial electric field shearing rate. The higher order in the expansion of E_r have been neglected, therefore, only the linear terms in $\gamma_E x$ will be taken into account in the eigenmode equation. The "new" ω is defined as $\omega - n\omega_{E0}$ since $n\omega_{E0}$ is a Doppler shift and does not change the stability of the mode.

As a first step, (3.21) is multiplied by ϖ^2 and expressed in function of x:

$$\left[\left(\omega\left(\frac{d_{\text{eff}}^2}{2}\frac{\mathrm{d}^2}{\mathrm{d}x^2} - \frac{k_\theta^2\rho_{\text{eff}}^2}{2}\right) - 2n\bar{\omega}_d + \frac{k_\parallel'^2 c_{\text{eff}}^2}{2\omega}x^2\right)\left(\omega - k_\theta\gamma_E x - n\omega_{pi}^*\right) - \frac{f_t}{f_p}n\omega_{pe}^* n\bar{\omega}_d \right.$$
$$\left. - \left(\omega - k_\theta\gamma_E x\right)\left(\omega - k_\theta\gamma_E x - n\omega_{ne}^*\right) + k'_\parallel x c_{\text{eff}}\left(n\omega_u^* + \frac{u_\parallel}{c_{\text{eff}}}\left(\frac{Z_{\text{eff}}}{\tau}\omega + n\omega_{ne}^* - 8n\bar{\omega}_d\right)\right)\right]\bar{\phi} = 0 \tag{3.23}$$

d_{eff} is defined as $d_{\text{eff}}^2 = \delta_{eff}^2 + 4\frac{n\bar{\omega}_d}{\omega}(\hat{s} - \alpha - 0.5)d^2$, containing all terms proportional to k_r^2 with $\delta_{eff} = q^2/(2\epsilon)\rho_{eff}$ and $c_{\text{eff}} = \sqrt{T_e/m_p}$. $k'_\parallel$ is the first term of the Taylor expansion of $k_\parallel$ *i.e.*$k'_\parallel = \frac{k_\theta\hat{s}}{qR}$.

(3.23) is not linear due to the interaction between the $\mathbf{E}\times\mathbf{B}$ shear and k_r. This is therefore a second order (non-linear) differential equation for which there is no generic analytic expression. But, the ballooning representation used to derive the gyro-kinetic dispersion relation (3.43) assumes a ballooned turbulence around $\theta = 0$. This is not correct if $\gamma_E \gg \omega$. Therefore, the quadratic terms in $\gamma_E x$ and the non-linear terms $k_\perp\gamma_E x$ are neglected, x being small. Any term in x^3 or superior is also neglected. This results in a second order *linear* differential equation:

$$\left[\left(\omega\left(\frac{d_{\text{eff}}^2}{2}\frac{\mathrm{d}^2}{\mathrm{d}x^2} - \frac{k_\theta^2\rho_{\text{eff}}^2}{2}\right) + \frac{k_\parallel'^2 c_{\text{eff}}^2}{2\omega}x^2\right)\left(\omega - n\omega_{pi}^*\right) - 2n\bar{\omega}_d(\omega - k_\theta\gamma_E x) - \omega^2 + 2k_\theta\gamma_E x + \right.$$
$$\left.\left(\omega - k_\theta\gamma_E\right)n\omega_{ne}^* - \frac{f_t}{f_p}n\omega_{pe}^* n\bar{\omega}_d + k'_\parallel x c_{\text{eff}}\left(n\omega_u^* + \frac{u_\parallel}{c_{\text{eff}}}\left(\frac{Z_{\text{eff}}}{\tau}\omega + n\omega_{ne}^* - 8n\bar{\omega}_d\right)\right)\right]\bar{\phi} = 0 \tag{3.24}$$

The solution of (3.24) is a shifted Gaussian:

$$\bar{\phi} = \frac{\phi_0}{\left(\pi \Re\left(\mathrm{w}^2\right)\right)^{1/4}} \exp - \frac{(x - x_0)^2}{2\mathrm{w}^2} \tag{3.25}$$

defined by its mode width w and its shift $\mathbf{x}_0$.

The mode width is defined by the *quadratic* terms in x in (3.24) considering that:

$$\frac{\mathrm{d}^2}{\mathrm{d}x^2}\bar{\phi} = \left(\frac{(x - \mathbf{x}_0)^2}{w^4} - \frac{1}{w^2}\right)\bar{\phi} \tag{3.26}$$

due to the expression of $\bar{\phi}$. The mode width corresponds the balance between the drive of the turbulence and the parallel dynamics of the passing particles connecting more stable (HFS) and more unstable (LFS) regions:

$$\mathrm{w}^2 = \frac{-\imath\omega d_{\mathit{eff}}}{|k'_\parallel| c_{\mathit{eff}}} \tag{3.27}$$

It follows the same definition as before [Bourdelle et al., 2007, Romanelli et al., 2007] but ω used here is the self consistent solution of (3.24), thus the mode width depends on γ_E, $\nabla u_\parallel$ and $u_\parallel$.

The mode shift, *i.e.* the parallel asymmetrisation of the mode, is calculated with the *linear* terms in x in (3.24):

$$x_0 = \frac{2n\bar{\omega}_d}{\omega - \omega^*_{ne}} \frac{\frac{q}{s}\gamma^N_E\left(2\omega + 2n\bar{\omega}_d - n\omega^*_{ne}\right) + n\omega^*_u + \frac{u_\parallel}{c_{\mathit{eff}}}\left(\frac{Z_{\mathit{eff}}}{\tau}\omega + n\omega^*_{ne} - 8n\bar{\omega}_d\right)}{k'_\parallel c_{\mathit{eff}}} \tag{3.28}$$

where $\gamma^N_E = \frac{\gamma_E}{c_{\mathit{eff}}/R}$ corresponds to usual normalisations of the $\mathbf{E} \times \mathbf{B}$ shear. The ITG dispersion relation $\frac{\omega}{\omega - \omega^*_{pi}} = -\frac{2n\bar{\omega}_d}{\omega - \omega^*_{ne}}$ is used in (3.28) to ensure that the shift stays small according to the assumption that the turbulence is ballooned around $\theta = 0$ in the same spirit as what is done in Garbet et al. [2002]. As x_0 is complex, an imaginary shift in x corresponds to a real shift in k_r which means a *linear* stabilization of large radial structures. Its dependence with respect to the parallel symmetry breakers is studied in the next section.

ω is defined by the x-free terms of (3.24). Once the mode width and the mode shift are expressed according to (3.27) and (3.28), the former relation reduces to a third order polynomial equation:

$$\begin{aligned}
&\frac{\omega}{2}\left(\frac{q}{s}\gamma^N_E\left(2\omega + 2n\bar{\omega}_d - n\omega^*_{ne}\right) + n\omega^*_u + \frac{u_\parallel}{c_{\mathit{eff}}}\left(\frac{Z_{\mathit{eff}}}{\tau}\omega + n\omega^*_{ne} - 8n\bar{\omega}_d\right)\right)^2 + \\
&\left(\omega\left(\omega - n\omega^*_{ne}\right) + \frac{f_t}{f_p}n\omega^*_{pe}n\bar{\omega}_d\right)\left(\omega - \omega^*_{pi}\right) + \left(2n\bar{\omega}_d + \frac{\imath k'_\parallel c_{\mathit{eff}} d_{\mathit{eff}}}{2}\right)\left(\omega - n\omega^*_{pi}\right)^2 = 0
\end{aligned} \tag{3.29}$$

The solution retained is the one of maximum growth rate $\gamma = \Im(\omega)$. The real part of ω is typically of the order of a few $n\bar{\omega}_d$ satisfying $\omega \geq k_\parallel v_\parallel$. The hydrodynamic limit conditions appear therefore barely respected. As for the solution of the kinetic equation (3.10), $n\omega_d < \Re(\omega) < k_\parallel v_\parallel$, confirming that the hydrodynamic limit is not valid in most conditions. Therefore, the predicted ω is overestimated, in particular its real part and the validity of the resulting eigenfunctions must be checked against self-consistent gyro-kinetic simulations.

3.2.2 Eigenfunctions validation

Now that the model employed to predict the linear eigenfunctions has been described, it remains to be compared to self-consistent gyro-kinetic eigenfunctions. This comparison is realized with the GKW code [Peeters et al., 2009b] which is δf code like QuaLiKiz. Field aligned coordinates [Hamada, 1959] are employed rather than the ballooning representation. There are no approximation in the integration over the pitch-angle and the energy and various magnetic equilibria are available in GKW. For consistency with QuaLiKiz, all direct comparisons are realized with the $\hat{s}-\alpha$ equilibrium in GKW using $\alpha = 0$. In this equilibrium, GKW parallel coordinate s is equivalent to QuaLiKiz $\frac{\theta}{2\pi}$[Peeters et al., 2009b]. The effects of the parallel velocity and its gradient are shown to be correctly accounted for in QuaLiKiz. The effect of γ_E is studied as well.

First, it is verified in Figure 3.1 that the new model previously presented gives a satisfactory agreement with gyro-kinetic eigenfunctions in the absence of rotation as in [Citrin et al., 2012, Romanelli et al., 2007]. Both GKW (in light green) and QuaLiKiz eigenfunctions (in darker blue) are plotted as a function of the parallel label $\theta/(2\pi)$. GA-std parameters are used. Unless stated otherwise $\epsilon = 1/6$, $R/L_n = 3$, $R/L_T = 9$, $q = 2$, $\hat{s} = 1$, $Z_{eff} = 1$. The poloidal wave number for the study is $k_\theta \rho_s = 0.3$ as it roughly corresponds to the spectral peak of non-linear fluxes. Figure 3.1 shows a good agreement between QuaLiKiz trial eigenfunction and GKW. QuaLiKiz eigenfunction is more peaked around $\theta = 0$, indicating a slight overestimation of the mode width. This is consistent with Figure 16 from Citrin et al. [2012].

The influence of the parallel rotation on the parallel structure of the eigenmodes is now studied in Figure 3.2. In the left panel, QuaLiKiz and GKW eigenfunctions are plotted against the field aligned poloidal angle $\theta/2\pi$ with GA-std parameters except for the parallel velocity gradient (PVG) set to $-4v_{Ti}/R$. This corresponds to maximum experimental values of PVG in core tokamak plasmas[de Vries et al., 2008, Peeters and Angioni, 2005]. In the right panel, the PVG is null and the parallel velocity is set to $0.2v_{Ti}$. It corresponds to the standard rotation of core plasmas. In both panels, the eigenfunctions appear ballooned in the region where $\theta \sim 0$ confirming previous approximations. But, contrary to the case where there is no rotation [Citrin et al., 2012] (see Figure 3.1), the eigenfunctions are no longer θ-symmetric. As expected from the expression (3.28) for the mode shift, $\mathbf{x}_0$ is proportional

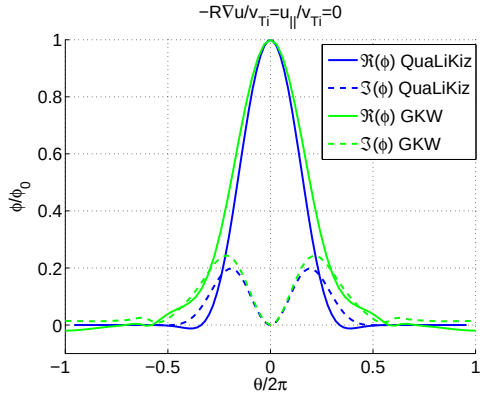

Figure 3.1: Parallel structure of the eigenfunctions showing the expected symmetry $\theta \rightarrow -\theta$ *i.e.* $k_{\parallel} = 0$ at zero rotation. GA-std parameters, $k_\theta \rho_s = 0.3$

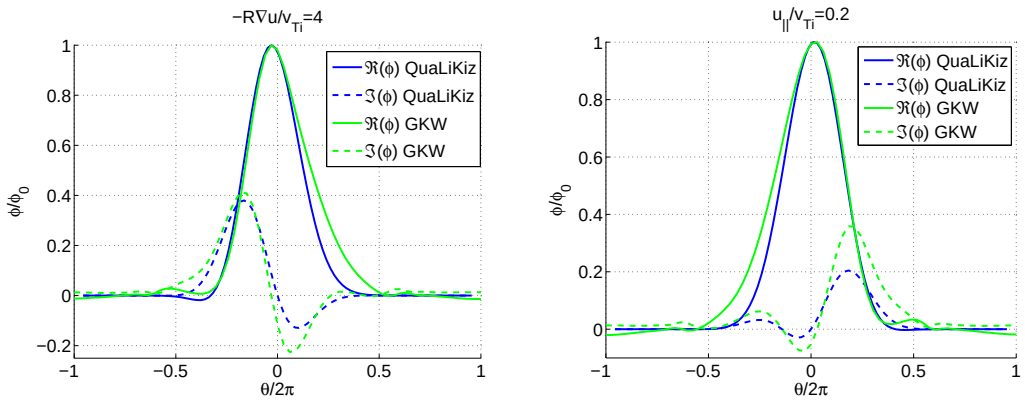

Figure 3.2: Parallel structure of the eigenfunctions showing finite $\langle k_{\parallel} \rangle$ in presence of finite $\nabla u_{\parallel}$ (left) and $u_{\parallel}$ (right)

to $u_{\parallel}$, $\nabla u_{\parallel}$ and γ_E. The agreement with gyro-kinetic eigenfunctions is very good in these conditions for both the real and the imaginary parts.

Closer to the turbulence threshold ($R/L_T = 6$), the agreement with gyro-kinetic eigenfunctions stays satisfactory as illustrated by Figure 3.3 both in the case without rotation and with rotation gradient. The behaviour of the model presented in 3.2.1 was also validated against gyro-kinetic simulations for various safety factor and magnetic shear values as illustrated in Figures 3.4 and 3.5 respectively.

The existence of an imaginary part is a novelty. It was previously neglected since, in the absence of sheared flows, the imaginary part of the mode width is small compared its real part and there is no shift in this case (see Figure 3.1). It was included here because it becomes of the order of the real part in case of strong $\mathbf{E} \times \mathbf{B}$ flow shear. An example of the eigenfunctions found in presence of $\mathbf{E} \times \mathbf{B}$ shearing is plotted in Figure 3.6 where the

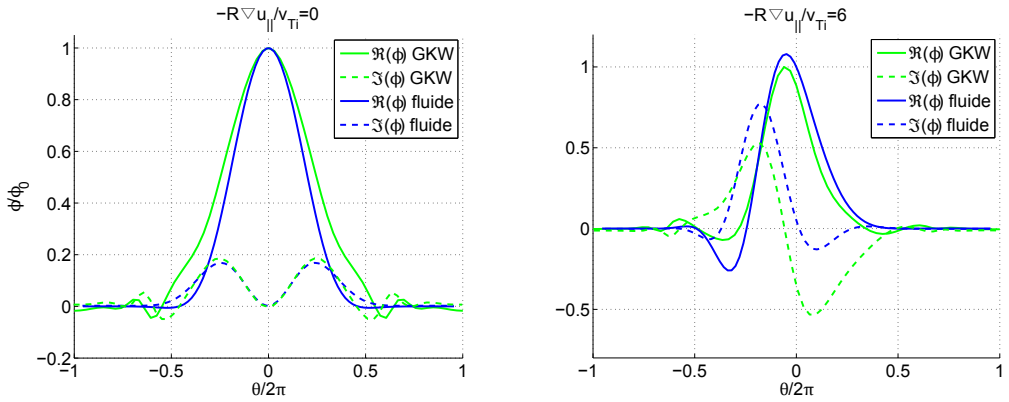

Figure 3.3: Parallel structure of the eigenfunctions in presence of lower temperature gradients: $R/L_T = 6$

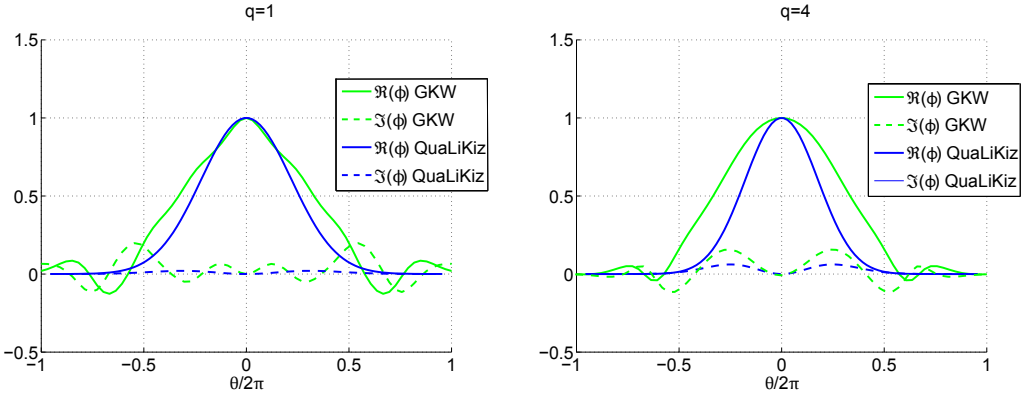

Figure 3.4: Parallel structure of the eigenfunctions in presence of lower and larger values of q

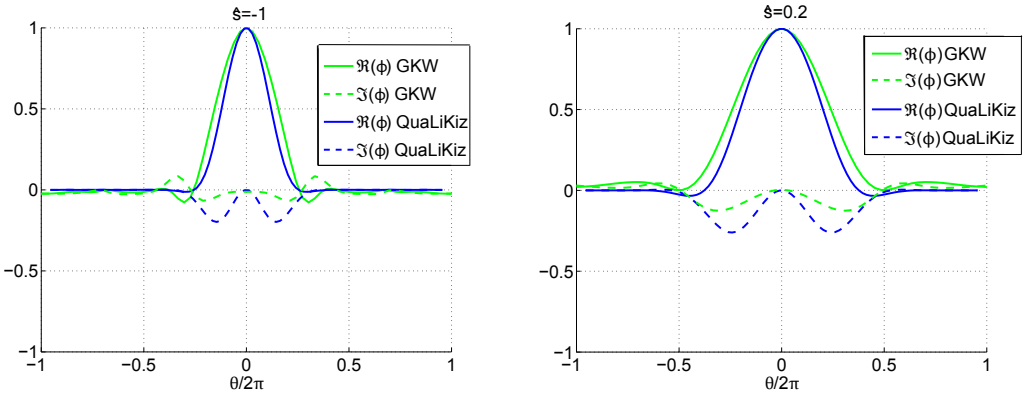

Figure 3.5: Parallel structure of the eigenfunctions in presence of negative magnetic shear and lower magnetic shear

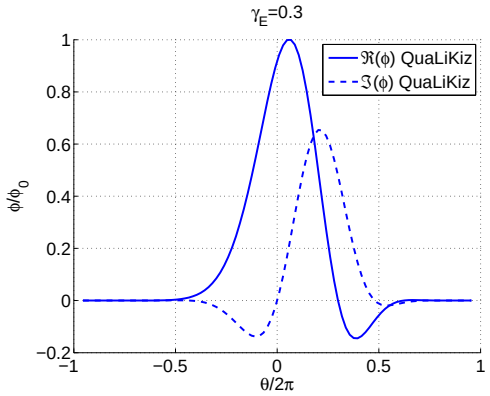

Figure 3.6: Parallel structure of the eigenfunctions showing finite $\langle k_\parallel \rangle$ in presence of finite $\mathbf{E} \times \mathbf{B}$ shear

imaginary part $\Im(\phi)$ (dashed curve) is found to be comparable to the real part $\Re(\phi)$ of the eigenfunction. The θ-shift of the real part of $\tilde{\phi}$ is especially important because it represents a $k_\parallel$-shift contributing to the momentum flux as illustrated in the following chapter § 4.3.1. For $\mathbf{E} \times \mathbf{B}$ shear, there is no direct comparison possible with GKW since the general solutions of the linearised gyro-kinetic equation in such conditions are oscillating Floquet modes[Cooper, 1988, Waltz et al., 1998]. In the reduced model presented here, eigenfunctions are found thanks to the truncation at lowest order of the ballooning representation and the linearisation of the eigenmode equation performed in (3.24). The validity of the eigenfunction found here is discussed in the next chapter when validating QuaLiKiz momentum flux versus non-linear GKW (see § 4.4).

With the GA-std case set of parameters, chosen for the cases presented above, Ion Temperature Gradient (ITG) modes are dominant. They are known to be ballooned around $\theta = 0$ in ballooning space [Candy et al., 2004] so the approximations taken in the previous chapter are correct. Under such approximations, the hydrodynamic-limit eigenfunctions are shown to agree reasonably well with self-consistent gyro-kinetic eigenfunctions even in presence of finite rotation and/or gradient of rotation.

The Trapped Electron eigenmodes (TEM) encountered in dominantly electron heated plasmas are more extended in θ than ITG modes[Brunner et al., 1998]. Taking only the lowest term of the ballooning representation as is done in QuaLiKiz, fails to reproduce their extension outside $\theta \in [-\pi; \pi]$ in ballooning space. This extension is especially important for strongly dominant TEM at $k_\theta \rho_s \sim 1$ as illustrated in Figure 3.7 where QuaLiKiz and GKW eigenfunctions are plotted for GA-std case parameters except for the ion temperature gradient: $R/L_{Ti} = 0$ while $R/L_{Te} = 9$. Inside $[-\pi; \pi]$, the agreement between QuaLiKiz and GKW is good at lower $k_\theta \rho_s$ and decline at finer scales as expected due to the linearisation of the Bessel functions in the hydrodynamic model.

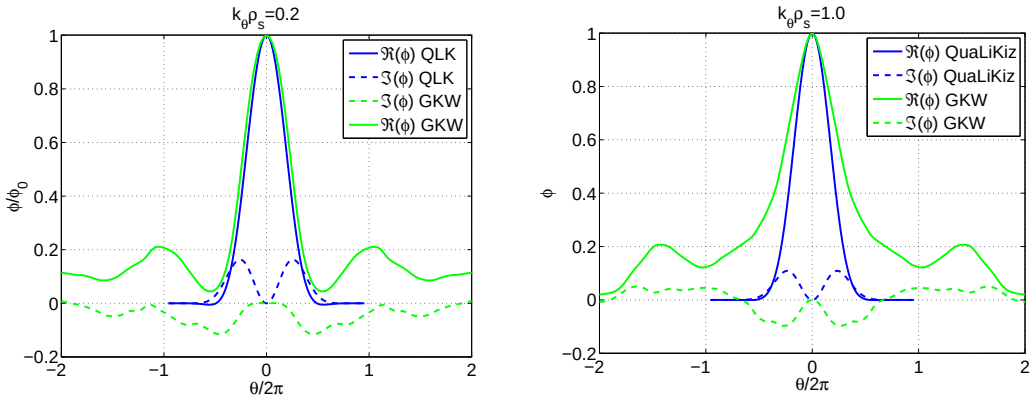

Figure 3.7: Parallel structure of the eigenfunctions showing the increased θ spreading with $k_\theta \rho_s$ in the case of TEM. $R/L_{Ti} = 0$, other parameters from GA-std test case. $k_\theta \rho_s = 0.2$ left panel. $k_\theta \rho_s = 1.0$ right panel.

Due to the limits at larger θ of the approximation used for QuaLiKiz eigenfunctions, an underestimation of TEM growth rate can therefore be foreseen for $k_\theta \rho_s \sim 1$. This is confirmed by QuaLiKiz underestimation of the growth rates compared to GKW in Figure 3.9 for $0.7 < k_\theta \rho_s \leq 1$. For transport studies however, the low $k_\theta \rho_s$ matter most. Moreover, the quasi-linear approximation is only correct at large scales (see § 4.2 next chapter). Since $\theta \in [-\pi; \pi]$ contains most of the physics, QuaLiKiz is able to model correctly heat and particle fluxes in TEM dominated regimes as illustrated by Figure 9 of Casati et al. [2009].

To summarize, the effects of $u_\parallel$, $\nabla u_\parallel$ and $\mathbf{E} \times \mathbf{B}$ shear are included in the model presented in Sec. 3.2.1. They result in a complex shift of the Gaussian eigenfunction and an increase of the relative amplitude of its imaginary part. The influence of $u_\parallel$ and $\nabla u_\parallel$ on the eigenfunctions is successfully benchmarked against GKW. QuaLiKiz model represents correctly ITG dominated eigenmodes but it cannot capture the extension outside $|\theta| = \pi$ of TEM. This is a necessary trade off to gain two orders of magnitude in CPU time with respect to self-consistent gyro-kinetic eigenfunctions calculation making QuaLiKiz suitable for integrated modelling.

The validity of QuaLiKiz model is further investigated in the next section where QuaLiKiz linear growth-rates are compared to GKW linear simulations.

3.3 Eigenvalues of QuaLiKiz dispersion relation

The linear growth rates calculated with the fluctuating potential defined in the previous section and the linearised gyro-kinetic electro-neutrality equation (3.10) is now compared to GKW linear simulations in presence of $u_\parallel$, $\nabla u_\parallel$ and $\mathbf{E} \times \mathbf{B}$ shear. First the dispersion relation of QuaLiKiz will be derived in details.

3.3.1 Separating passing and trapped particles

As mentioned in the previous section, passing and trapped particles are treated separately in QuaLiKiz to take advantage of their different dynamics and to reduce the numerical cost of the model. (3.10) will be formally expressed as $1 - \mathcal{L}_{s,tr} - \mathcal{L}_{s,pass} = 0$.

Different expressions for $n_2\Omega_2$ are used for the two types of particles. For passing particles, its expression is given by:

$$n_2\Omega_2 = k_\parallel v_\parallel = \pm\frac{v_{Ts}x}{qRd}\sqrt{\xi(1-\lambda b)} \tag{3.30}$$

where $d = \frac{1}{k_\theta \hat{s}}$ is the distance between resonant surfaces and x, the distance to the closest resonant surface. For trapped particles, the ratio $\frac{x}{d}$ is replaced by m, a poloidal wave number expressing the existence of a well defined bounce frequency ω_b so that $n_2\Omega_2 = m\omega_b$.

As previously indicated, an average over the bounce motion is performed for trapped particles, reducing further the numerical cost of the model. It enables to remove the θ dependence of the drift frequencies. In the same spirit as the gyro-motion average, bounce motion average — *i.e.* average over $\alpha_2 \approx \theta$ — results in the multiplication of the trapped particles response by Bessel functions $J_m(k_r\delta_s)$. The wave number $n_2 \equiv m$ corresponds to $k_r\delta_s$ this time where $\delta_s = q^2/(2\epsilon)\rho_s$ is the so-called banana width of the species s characterising the radial width of the bounce motion. The integration in energy of the Bessel functions is again done separately giving $\mathcal{B}_m(a) = \exp(-a^2)I_m(a^2)$ ([see Bourdelle et al., 2002, App. A.4] for the $m = 0$ case). In a condensed form, (3.10) reads:

$$\sum_s \frac{e_s^2 n_s}{T_s} 1 - \int \frac{\mathrm{d}k_r}{2\pi}\left(\langle \mathcal{I}_{s,pass}\rangle_p \mathcal{B}_0(k_\perp\rho_s) - \sum_m \langle \mathcal{I}_{s,m,tr}\rangle_t \mathcal{B}_0(k_\perp\rho_s)\mathcal{B}_m(k_r\delta_s)\right) = 0 \tag{3.31}$$

where the integration over the passing domain is

$$\langle\cdots\rangle_p = \int_0^\infty \frac{2\sqrt{\xi}}{\sqrt{\pi}}\exp(-\xi)\mathrm{d}\xi \int_0^{\lambda_c}\frac{\mathrm{d}\lambda}{4\bar{\omega}_b}$$

$\lambda_c = \frac{1-\epsilon}{1+\epsilon}$ is the minimum value of the pitch angle for which particles can be trapped and $\bar{\omega}_b$ is the normalization of λ over the parallel (or bounce) motion $\bar{\omega}_b^{-1} = \oint \frac{\mathrm{d}\theta}{2\pi}\frac{1}{\sqrt{1-\lambda b}}$ with $\oint = \int_\pi^\pi$ for passing particles and $\oint \approx 2\int_{-\theta_b}^{\theta_b}$ for trapped particles, θ_b being the bouncing point of the trapped particles. The integration over the trapped domain then reads:

$$\langle\cdots\rangle_t = \int_0^\infty \frac{2\sqrt{\xi}}{\sqrt{\pi}}\exp(-\xi)\mathrm{d}\xi \int_{\lambda_c}^1 \frac{\mathrm{d}\lambda}{4\bar{\omega}_b} = f_t\int_0^\infty \frac{2\sqrt{\xi}}{\sqrt{\pi}}\exp(-\xi)\mathrm{d}\xi\int_0^1 K(\kappa)\kappa\mathrm{d}\kappa$$

where f_t is the fraction of trapped particles, κ is related to the pitch-angle via $\lambda = 1 - 2\epsilon\kappa^2$ and K is the complete elliptic integral of the first kind. Now, $\mathcal{I}_{s,pass}$ and $\mathcal{I}_{s,tr}$ remain to be expressed.

3.3.1.1 Passing particle functional

Before integration the passing particle functional reads:

$$\mathcal{I}_{s,pass} = \sum_{\epsilon_\parallel=\pm 1}\left(1+\frac{2u_\parallel}{v_{Ts}}\epsilon_\parallel\sqrt{\xi(1-\lambda b)}+\frac{u_\parallel^2}{v_{Ts}^2}\left(2\xi(1-\lambda b)-1\right)\right) \frac{A_{Ts}^*\xi+2(A_u-A_{Ts})\frac{u_\parallel}{v_{Ts}}\epsilon_\parallel\sqrt{\xi(1-\lambda b)}+A_{ns}-\frac{3}{2}A_{Ts}+\frac{u_\parallel^2}{v_{Ts}^2}(A_{Ts}-2A_u)-\frac{\varpi}{n\bar{\omega}_{ds}}}{(2-\lambda b)f_\theta\xi+\epsilon_\parallel\frac{x}{d}\frac{\omega_b}{n\bar{\omega}_{ds}}-\frac{\varpi}{n\bar{\omega}_{ds}}+\imath o^+} \tag{3.32}$$

The integration over λ and ξ is then performed. In QuaLiKiz, the integration over λ, not tractable analytically, is simplified. It is considered that the passing particle pitch-angle variation does not influence the drift frequencies so that they can be averaged over λ. This assumption is correct for the curvature and ∇B drift for which the pitch angle variation represents no more than 50% of its value. For $k_\parallel v_\parallel$ expression however, this means that its value will be overestimated for barely passing particles. The result is given in Eq. 3.33 using the Fried-Conte function $Z(z)=\frac{1}{\sqrt{\pi}}\int_{-\infty}^{+\infty}\frac{e^{-v^2}}{v-z}\mathrm{d}v$.

$$\begin{aligned}\left\langle\mathcal{I}_{s,pass}\right\rangle_p = &\frac{3f_p}{2f_\theta}\left[A_{Ts}\frac{Z_2(V_+)-Z_2(V_-)}{V_+-V_-}+\left(A_{ns}-\frac{3}{2}A_{Ts}-\frac{\varpi}{n\bar{\omega}_{ds}}\right)\frac{Z_1(V_+)-Z_1(V_-)}{V_+-V_-}\right]\\ &+\frac{3f_p}{f_\theta}\left[\frac{u_\parallel}{v_{Ts}}A_{Ts}\frac{V_+Z_2(V_+)-V_-Z_2(V_-)}{V_+-V_-}+\left(A_u+\frac{u_\parallel}{v_{Ts}}\left(A_{ns}-\frac{5}{2}A_{Ts}-\frac{\varpi}{n\bar{\omega}_{ds}}\right)\right)\frac{V_+Z_1(V_+)-V_-Z_1(V_-)}{V_+-V_-}\right]\\ &+\frac{f_p}{f_\theta}\frac{u_\parallel}{v_{Ts}}\left[A_T\frac{u_\parallel}{v_{Ts}}\frac{Z_3(V_+)-Z_3(V_-)}{V_+-V_-}+\left(2A_u\frac{u_\parallel}{v_{Ts}}\left(A_{ns}-\frac{7}{2}A_{Ts}-\frac{\varpi}{n\bar{\omega}_{ds}}\right)\right)\frac{Z_2(V_+)-Z_2(V_-)}{V_+-V_-}\right]\\ &-\frac{3f_p}{f_\theta}\frac{u_\parallel}{v_{Ts}}\left[A_{Ts}\frac{u_\parallel}{v_{Ts}}\frac{Z_2(V_+)-Z_2(V_-)}{V_+-V_-}+\left(2A_u\frac{u_\parallel}{v_{Ts}}\left(A_{ns}-\frac{5}{2}A_{Ts}-\frac{\varpi}{n\bar{\omega}_{ds}}\right)\right)\frac{Z_1(V_+)-Z_1(V_-)}{V_+-V_-}\right]\end{aligned} \tag{3.33}$$

where f_p is the passing particle fraction. Z_1, Z_2 and Z_3 are based on the Fried-Conte function Z: $Z_1(z)=z+z^2Z(z)$, $Z_2(z)=\frac{1}{2}z+z^2Z_1(z)$ and $Z_3(z)=\frac{3}{4}z+z^2Z_2(z)$. The variables V_+ and V_- correspond to the poles of Eq. 3.32. They are defined by:

$$\begin{aligned}V_\pm &= \frac{1}{2}\frac{v_{Ts}x}{qRd}\frac{\bar{\omega}_b}{f_\theta n\bar{\omega}_{ds}}\pm\sqrt{\Delta}\\ \Delta &= \left(\frac{1}{2}\frac{v_{Ts}x}{qRd}\frac{\bar{\omega}_b}{f_\theta n\bar{\omega}_{ds}}\right)^2+\frac{\varpi}{f_\theta n\bar{\omega}_{ds}}\end{aligned} \tag{3.34}$$

The integration over k_r remains to be performed. As expressed in (3.30), there remains some x dependences in the passing particle functional. Moreover, it is reminded that $\varpi=\omega-n\omega_{E\times B}$ contains an x dependence too. To take these aspects into account an integration over k_r and $x=r-r_0$, where $x\ll r_0$, is performed as derived by Garbet et al. [1990] and presented first in Bourdelle et al. [2002, App. A.4.2] in QuaLiKiz framework. The expression

of $\mathcal{L}_{s,pas.} = \int_{-\infty}^{+\infty} \frac{\mathrm{d}k_r}{2\pi} \langle \mathcal{I}_{s,pass} \rangle_p \mathcal{B}_0(k_\theta \rho_s)$ is then transformed into:

$$\mathcal{L}_{s,pas.} = \int_{-\infty}^{\infty} \frac{\mathrm{d}k_+}{2\pi} \iint_{-\infty}^{\infty} \mathrm{d}x_+ \mathrm{d}x_- \tilde{\phi}(x_+ - \frac{x_-}{2}) \tilde{\phi}^*(x_+ + \frac{x_-}{2}) e^{\imath k_+ x_-} \langle \mathcal{I}_{s,pass} \rangle_p \mathcal{B}_0(k_\theta \rho_s) \quad (3.35)$$

As shown in section 3.2.1, $\tilde{\phi}(x) = \phi_0 \exp(-\frac{(x-x_0)^2}{2w^2})$ when enabling the treatment for non-zero values of $u_\parallel$, $\nabla u_\parallel$ and $\mathbf{E} \times \mathbf{B}$ shear. The product $\phi\phi^*$ can then be written as:

$$\tilde{\phi}\tilde{\phi}^* = \phi_0^2 \exp\left(-\frac{(x_+ - \Re(x_0) - k_+ \Im(\mathrm{w}^2))^2}{\Re(\mathrm{w}^2)} - \Re(\mathrm{w}^2) \left(k_+ - \frac{\Im(x_0)}{\Re(\mathrm{w}^2)} \right)^2 \right) \quad (3.36)$$

Dimensionless quantities ρ^* and k^* are defined for the integration over x_+ and k_+:

$$\begin{aligned} \rho^{*2} &= \frac{(x_+ - \Re(x_0) - k_+ \Im(\mathrm{w}^2))^2}{\Re(\mathrm{w}^2)} \\ k^{*2} &= \Re(\mathrm{w}^2) \left(k_+ - \frac{\Im(x_0)}{\Re(\mathrm{w}^2)} \right)^2 \end{aligned} \quad (3.37)$$

The x quantity used in (3.34) is replaced by $\rho^* \sqrt{\Re(\mathrm{w}^2)} + \Re(x_0) + k_+ \Im(\mathrm{w}^2)$ and $k_+ = \frac{k^*}{\sqrt{\Re(\mathrm{w}^2)}} + \frac{\Im(\mathrm{w}^2)}{\Re(\mathrm{w}^2)}$, $\Re(\mathrm{w}^2)$ being defined positive which ensures $\left|\tilde{\phi}\right|^2$ to be finite. The passing particle functional then becomes:

$$\mathcal{L}_{s,pass} = \int_{-\infty}^{\infty} \frac{\mathrm{d}k^*}{\sqrt{\pi}} e^{-k^{*2}} \int_{-\infty}^{\infty} \frac{\mathrm{d}\rho^*}{\sqrt{\pi}} e^{-\rho^{*2}} \langle \mathcal{I}_{s,pass} \rangle_p (k^*, \rho^*) \mathcal{B}_0(k_\theta \rho_s) \quad (3.38)$$

3.3.1.2 Trapped particle functional

For trapped particles, there are no θ dependence in the drifts, since it is already removed by the bounce average. So, the picture is somewhat simpler. It is reminded that $k_\parallel v_\parallel$ has no x dependence and $\frac{x}{d}$ in Eq. 3.32 is replaced by m.

$$\mathcal{I}_{i,m,tr} = \sum_{\epsilon_\parallel = \pm 1} \left(1 + \frac{2u_\parallel}{v_{Ts}} \epsilon_\parallel \sqrt{\xi(1-\lambda b)} + \frac{u_\parallel^2}{v_{Ts}^2} (2\xi(1-\lambda b) - 1) \right)$$
$$\frac{A_{Ts}^* \xi + 2(A_u - A_{Ts}) \frac{u_\parallel}{v_{Ts}} \epsilon_\parallel \sqrt{\xi(1-\lambda b)} + A_{ns} - \frac{3}{2} A_{Ts} + \frac{u_\parallel^2}{v_{Ts}^2} (A_{Ts} - 2A_u) - \frac{\varpi}{n\bar{\omega}_{ds}}}{(2-\lambda b) f_\theta \xi + \epsilon_\parallel m \frac{\omega_b}{n\bar{\omega}_{ds}} - \frac{\varpi}{n\bar{\omega}_{ds}} + \imath o^+} \quad (3.39)$$

The attentive reader noticed that the relation (3.39) is expressed for trapped ions. Its expression is different for trapped electrons because electron-ion collisions are taken into account in QuaLiKiz. Since the effect of collisionality on TEM is most important and not much predictable otherwise [Connor, 2006], collisions are only implemented on trapped electrons. For $\mathcal{I}_{e,m,tr}$, ν_{ie} is included in Eq. 3.39 in place of the Landau prescription for causality, the small quantity $\imath o^+$, through a Krook operator presented in Romanelli et al.

[2007]. The expression of $\mathcal{I}_{e,m,tr}$ is

$$\mathcal{I}_{e,m,tr} = \sum_{\epsilon_\parallel=\pm 1}\left(1+\frac{2u_\parallel}{v_{Ts}}\epsilon_\parallel\sqrt{\xi(1-\lambda b)}+\frac{u_\parallel^2}{v_{Ts}^2}\left(2\xi(1-\lambda b)-1\right)\right) \frac{A_{Ts}^*\xi+2(A_u-A_{Ts})\frac{u_\parallel}{v_{Ts}}\epsilon_\parallel\sqrt{\xi(1-\lambda b)}+A_{ns}-\frac{3}{2}A_{Ts}+\frac{u_\parallel^2}{v_{Ts}^2}(A_{Ts}-2A_u)-\frac{\varpi}{n\bar{\omega}_{ds}}}{(2-\lambda b)f_\theta\xi+\epsilon_\parallel m\frac{\omega_b}{n\bar{\omega}_{ds}}-\frac{\varpi}{n\bar{\omega}_{ds}}+\imath\frac{\nu_{fe}(\xi,\lambda)}{n\bar{\omega}_{ds}}} \tag{3.40}$$

where $\nu_{fe}=\nu_{ei}\left(\frac{v_{Te}}{\sqrt{\xi}}\right)^3 Z_{\text{eff}}\left(\frac{\epsilon}{|1-\epsilon-\lambda|^2}\frac{0.111\delta+1.31}{11.79\delta+1}\right)$ with $\delta=\left(\frac{|\omega|}{37.2/\epsilon Z_{\text{eff}}\nu_{ei}}\right)^{1/3}$ [Romanelli et al., 2007].

Now, before performing the integral over (ξ,λ) it is worth noting that $\mathcal{B}_1$ is odd in k_r. When integrating over k_r, it will only give a non-zero value for $\langle\mathcal{I}_{s,1,tr}\rangle$ in presence of an asymmetric eigenfunction in k_r which happens only in the presence of a parallel velocity symmetry breaker: $u_\parallel$, $\nabla u_\parallel$ or $\mathbf{E}\times\mathbf{B}$ shear in QuaLiKiz framework [Peeters and Angioni, 2005]. Given the fact that the Krook operator does not conserve momentum, it appears inadequate to keep this higher order term in the equation. Since $\mathcal{B}_2$ represents 5% of $\mathcal{B}_0$ when integrated over k_r, higher order are not treated neither. This is why the only term actually used in QuaLiKiz is $m=0$. Integrating (3.40) over (ξ,λ) gives the relation (3.41).

$$\langle\mathcal{I}_{0,i,tr}\rangle_t = 2f_t\int_0^1\frac{K(\kappa)\kappa}{f(\kappa)}\mathrm{d}\kappa\left[\left(1-\frac{u_\parallel^2}{v_{Ti}^2}\right)\left(A_{Ti}\frac{Z_2(z)}{z}+\left(A_{ni}-\frac{3}{2}A_{Ti}-z^2\right)\frac{Z_1(z)}{z}\right)-\frac{u_\parallel}{v_{Ti}}\left(2A_u-\frac{u_\parallel}{v_{Ti}}A_{Ti}\right)\right] \tag{3.41}$$

where z is the square root of $\frac{\varpi}{n\bar{\omega}_{ds}}$ which has a positive imaginary part and $f_\kappa=2\frac{E(\kappa)}{K(\kappa)}-1+4s\left(\kappa^2-1+\frac{E(\kappa)}{K(\kappa)}\right)=\oint\frac{\mathrm{d}\theta}{2\pi}\frac{f_\theta}{4\sqrt{1-\lambda b}}$ with $\lambda=1-2\epsilon\kappa^2$. Comparing (3.41) to (3.33), the reader might have noticed that the second and third terms (lines) of (3.33) are absent in (3.41). Indeed, the integration over λ gives $1-2\epsilon$ for passing particles and 2ϵ for trapped ions for the second term and $\frac{1}{3}$ for passing and $\frac{2}{3}f_t\epsilon$ for trapped ions for the third term. At lowest order in ϵ, the expression for the functional of trapped ions $\langle\mathcal{I}_{0,tr}\rangle$ therefore reduces to (3.41). For trapped electrons, the expression (3.40) is numerically integrated over (ξ,κ).

The integration over k_r is simplified by bounce averaging. Integration over θ being already performed for $\mathcal{I}_{0,tr}$ by bounce averaging, the only k_r dependence in $\mathcal{L}_{s,tr}$ lies in $\mathcal{B}_0(k_r\delta_s)|\tilde{\phi}_{n\omega}|^2$ which is integrated in k_r numerically. The Bessel function $\mathcal{B}_0(k_r\rho_s)$ is not included in the integration above. Indeed, the structures are much more elongated radially than poloidally: $k_\theta\gg k_r$ and $\delta_s\gg\rho_s$ making the k_r variation of $\bar{\phi}$ over the Larmor radius negligible compared to its variation over the banana width. The expression for the trapped

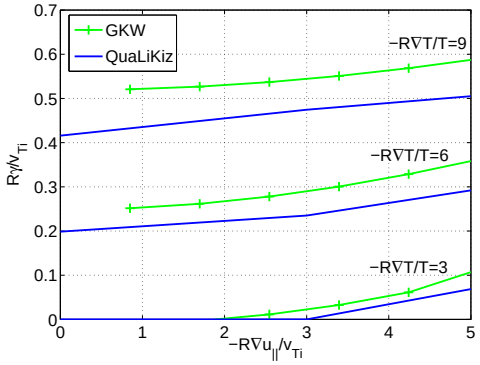

Figure 3.8: Maximum linear growth rates from QuaLiKiz and GKW for GA-std parameters

particle functionals $\mathcal{L}_{0,s,tr}$ can then be written:

$$\mathcal{L}_{0,s,tr} = \int_0^1 K(\kappa)\kappa\mathcal{I}_{0,tr}\mathrm{d}\kappa\mathcal{B}_0(k_\theta\rho_s)\int\frac{\mathrm{d}k_r}{2\pi}\mathcal{B}_0(k_r\delta_s)|\tilde{\phi}_{n\omega}(k_r)|^2 \tag{3.42}$$

In conclusion the expression (3.31) can be written as

$$\sum_s \frac{n_s e_s^2}{T_s}\left(1-\mathcal{L}_{s,pas}(\omega)-\mathcal{L}_{0,s,tr}(\omega)\right)=0 \tag{3.43}$$

with the definitions of the passing and trapped particle functionals given in the two previous sections.

3.3.2 Growth rates validation

A way to validate the model developed in this chapter is to compare the linear growth rates $\gamma = \Im(\omega)$ found with QuaLiKiz against the results from a gyro-kinetic code which does not use the simplifications previously detailed. An important benchmark effort has already been done, comparing QuaLiKiz growth rates against GS2 [Bourdelle et al., 2002, Romanelli et al., 2007] and GENE[Citrin et al., 2012]. A verification has been performed that new additions do not invalidate the results previously obtained. The comparison is limited here to the sheared flows impact by varying $u_\parallel$, $\nabla u_\parallel$ and γ_E using GKW linear simulations and GA-standard based test cases. Unless stated otherwise $\epsilon = 1/6$, $R/L_T = 9$, $R/L_n = 3$, $q = 2$, $\hat{s} = 1$, $\alpha = 0$, $\nu^* = 0$ in this section. The parallel velocity gradient destabilisation and the stabilizing effect of $\mathbf{E}\times\mathbf{B}$ shear are successfully benchmarked. The effects of the parallel velocity are recovered within the range of validity of the low Mach number approximation.

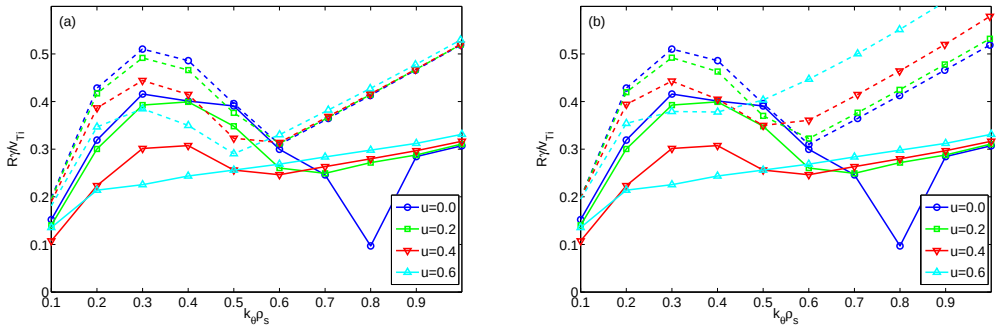

Figure 3.9: Linear growth rates from QuaLiKiz (plain curves) and GKW (dashed) for GA-std based cases with various $u = \frac{u_\parallel}{v_{Ti}}$ values. (a) GKW run without centrifugal effects (b) GKW run with centrifugal effects

3.3.2.1 The parallel velocity gradient instability

First, let us concentrate on $\nabla u_\parallel$. It has been extensively reported in the literature that parallel velocity gradients (PVG) destabilize a Kelvin-Helmholtz like instability[D'Angelo, 1965, Garbet et al., 2002, Peeters and Angioni, 2005]. PVG instabilities are destabilized by velocity gradients at rather high values: $-\frac{R\nabla u_\parallel}{v_{Ti}} \approx 5$ compared to the experiments[Peeters and Angioni, 2005]. But its threshold is reduced with increasing temperature gradient so that it can destabilize otherwise marginally stable conditions for ITG turbulence. Finally, PVG is known for enhancing the growth rates of already unstable ITG modes. All these effects are presented in Figure 3.8 where a scan in $\nabla u_\parallel$ is performed up to $\nabla u_\parallel = -5v_{Ti}/R$ for 3 values of temperature gradients $R/L_T = \{3, 6, 9\}$. For the flattest temperature profile conditions ($R/L_T = 3$), which is linearly stable without rotation, the PVG destabilization threshold is recovered. For the peaked temperature profile condition ($R/L_T = \{6, 9\}$), which are ITG unstable without rotation, the growth rate inflation with $\nabla u_\parallel$ is captured by QuaLiKiz. The values of the growth rates are nevertheless slightly underestimated.

3.3.2.2 The impact of the parallel velocity

The parallel velocity is known to have opposite effects on ion and electron modes. It stabilizes ITG modes and destabilizes trapped electron modes (TEM) via the expansion of the trapped domain in velocity space with increasing $u_\parallel$[Casson et al., 2010, 2012]. These effects are studied in Figure 3.9. Simulations from QuaLiKiz (in plain curve) and GKW (in dashed curve) based on GA-std parameters are represented. The parallel velocity is varied from 0 to $0.6v_{Ti}$, a larger value than usually observed in high aspect ratio tokamak core plasmas[de Vries et al., 2008]. The effect of the low Mach number approximation – used in QuaLiKiz, not in GKW – is analysed.

When comparing GKW (with centrifugal effects) and QuaLiKiz, Figure 3.9(b), it is clear that ITGs are stabilized with increasing $u_\parallel$ in both codes but TEMs are not destabilized in QuaLiKiz. This discrepancy is due to the low Mach number approximation which does not retain centrifugal effects. They were removed in GKW in Figure 3.9(a) to illustrate this. Indeed, without centrifugal effects, GKW electron modes are not destabilized. Moreover, at higher $\frac{u_\parallel}{v_{Ti}}$ values, ITGs are over stabilized in QuaLiKiz and TEMs become dominant for lower $k_\theta \rho_s$ values as $u_\parallel$ increases due to the stabilization of ITGs. This is a consequence of the development up to second order in $u_\parallel$ of the equilibrium distribution function (see (3.12)) which underestimates the values of the exponential in $u_\parallel$ contained in f_0 definition at larger values of $v_\parallel$. The underestimation of TEM growth rates by QuaLiKiz at higher $k_\theta \rho_s$ for any values of $u_\parallel$ is related to a discrepancy between QuaLiKiz and GKW eigenfunctions as detailed in 3.2.2.

Overall, larger $u_\parallel$ stabilize ITG dominated regimes in QuaLiKiz as observed in GKW. Trapped Electron Modes behaviour at larger poloidal wave numbers is however not properly modelled due to the low Mach number approximation and the reduced model used for the eigenfunctions.

3.3.2.3 The stabilization by $\mathbf{E} \times \mathbf{B}$ shear

The extensively studied stabilisation of the turbulence by $E \times B$ shear [Biglari et al., 1990, Dong and Horton, 1993, Waltz et al., 1994, Hahm and Burrell, 1995, Waltz et al., 1998, Roach et al., 2009, Barnes et al., 2011] is addressed in this section. To be able to perform the comparison with GKW, we highlight that a new method to calculate effective growth rates for initial value codes such as GKW with $\mathbf{E} \times \mathbf{B}$ shear is developed. This method is close to that of [Citrin, 2012] and results in a better qualitative agreement with non-linear observations. Indeed, with finite $\mathbf{E} \times \mathbf{B}$ shear, Floquet modes are solutions of the linearised gyro-kinetic equation, composed of an exponentially growing part and an oscillating part. Consequently, when averaging over the entire temporal window of the simulation, a strong drop in the effective growth rate is observed for the first non-zero value of γ_E and then a weak dependence with γ_E is seen as explained in [Waltz et al., 1998] and represented in Figure 3.11 dashed curve. In contrast, non-linear simulations show a smooth reduction of the fluxes with increasing $\mathbf{E} \times \mathbf{B}$ shear[Casson et al., 2009], fitted at times by a linear quench rule[Waltz et al., 1998]. An explanation for this discrepancy is that the non-linear decorrelation time is shorter than the time over which one averages the growth rates. The method proposed here to resolve this issue can be decomposed in two steps illustrated by Figure 3.10.

- First, an effective growth rate: $\gamma_{\text{eff}}(t)$ is calculated on 3 decorrelation times: τ, considering that $\tau = \gamma_{\text{eff}}^{-1}$. It means that $\gamma_{\text{eff}} = \left(\ln(\phi(t + \Delta t)) - \ln(\phi(t))\right)/\Delta t$ is calculated with $\Delta t = 3/\gamma_{\text{eff}}$. Equivalently $\phi(t + \Delta t) = \exp(3)\phi(t)$. The corresponding Δt is symbolized by the shaded area in Figure 3.10;

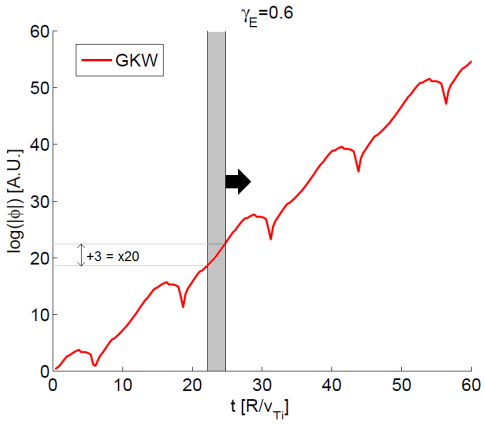

Figure 3.10: Example of the time evolution of a Floquet mode from a GKW simulation at $R/L_T = 15$, $\gamma_E = 0.6$ and other parameters from GA-std. The shaded region corresponds to $3\gamma^{-1} \approx 3\tau_{NL}$. The black arrow represents the displacement of the shaded region along t.

- The time window corresponding to $3\tau_{NL}$ is then moved along the simulation as indicated by the black arrow in Figure 3.10. The effective growth rate of the entire simulation is taken to be the 3^{rd} quartile of the ensemble of $\gamma_{eff}[0; t_{end}]$ to remove all negative $\gamma_{eff}(t)$ from the statistics.

This method is compared to the standard one – see for example [Roach et al., 2009] – in Figure 3.11. The so-called "GKW mean value" dotted curve represents the usual method and the "GKW" plain curve with error bars represents the method described above. The error bars extent corresponds to one standard deviation around the 3^{rd} quartile value. The usual "jump" in γ from 0 to finite value of γ_E is reduced, resulting in better qualitative agreement with the results from non-linear simulations. The growth rates from the eigenvalue code QuaLiKiz are plotted on the same figure in plain curve for comparison. They are in agreement with γ_{eff} within the error bars of the method presented above. This result shows that the $\mathbf{E} \times \mathbf{B}$ stabilisation mechanism is captured by QuaLiKiz approach using hydrodynamic shifted Gaussian eigenfunctions.

Through the three examples presented above, QuaLiKiz linear growth rates evolution with the three relevant quantities for sheared flows in a tokamak plasmas – $u_{\|}$, $\nabla u_{\|}$ and γ_E – have been validated. It should however be noted that more extensive benchmarks with different parameter sets have been left for future works. Along with the correct linear eigenfunctions, this gives the possibility to make a quasi linear estimate of the turbulent heat, particle and momentum fluxes accounting properly for PVG and $\mathbf{E} \times \mathbf{B}$ shear stabilisation at lower CPU cost.

*
* *

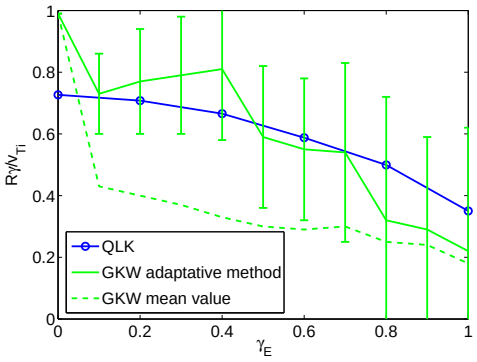

Figure 3.11: QuaLiKiz growth rates and GKW effective growth rates calculated with the standard averaging method and a new statistical method

In this chapter, the linearised gyro-kinetic dispersion relation (3.43) at the heart of the linear solver of QuaLiKiz was derived including the effect of the non-zero values for $u_\parallel$, $\nabla u_\parallel$ *and* $\mathbf{E}\times\mathbf{B}$ *shift in the low Mach number approximation and other standard approximations for QuaLiKiz, namely low* β *(electrostatic), large aspect ratio and lowest order ballooning representation. To solve this eigenfunction/eigenvalue equation, the eigenfunction* $\bar{\phi}$ *is calculated in the analytic hydrodynamic limit including the effect of sheared flows.* $\bar{\phi}$ *is a shifted Gaussian eigenfunction with a width illustrating the balance between the turbulence drive and the homogenisation by passing particles. The shift is proportional to the parallel symmetry breakers* $u_\parallel$, $\nabla u_\parallel$ *and the* $\mathbf{E}\times\mathbf{B}$ *shear. The resulting eigenfunctions and growth rates recover self-consistent gyro-kinetic results with a slight underestimation of the growth rates at larger scales and a more significant underestimation at finer scales. As illustrated in the next chapter, the validity of the quasi-linear approximation also falls off at finer scales. Due to the relative importance of large scales versus finer scales for transport processes, the quasi-linear model presented here show good agreement with non-linear gyro-kinetic simulations in spite of this loss of accuracy as exposed in the next chapter.*

4

Quasi-linear modelling of the turbulent fluxes

The goal of this chapter is to present the quasi-linear model employed for the fluxes calculation in QuaLiKiz and compare its results to non-linear gyro-kinetic simulations. The momentum flux is thoroughly studied since it is the main motivation of this work.

Attention is first focused on the quasi-linear approximation, its derivation and its validity for core tokamak plasma turbulence. The momentum flux is then derived using the formalism presented in chapters 2 and 3. As shown later on, quasi-linear fluxes are the product of two parts: a quasi-linear response and a saturated potential. We will see that the quasi-linear response corresponds essentially to the functionals derived in § 3.3. The saturated potential is typically a non-linear quantity which results from the interactions between the turbulence and zonal flows as well as mean flows. The part played by the interaction between linearly stable and unstable modes in the saturation process is also currently explored [Hatch et al., 2011]. Therefore, the saturated state cannot be inferred from the linearised equation. The construction of the saturated potential, based on both experimental observations and non-linear simulations is presented. In a second time, the modification of the quasi-linear fluxes by a sheared rotation is studied. The predicted stabilising effect of the $\mathbf{E} \times \mathbf{B}$ velocity shearing is studied in particular. The diffusivity of the momentum flux and the momentum pinch are analysed in a second time. As part of the study on the momentum flux contributions, the role of the eigenfunction asymmetrisation in both parts of the momentum flux will be discussed.

4.1 Achievements of quasi-linear models

Before diving into quasi-linear theory, a brief review of the existing models is presented with the aim to put QuaLiKiz framework and abilities into context, completeness being way out of the scope of this introduction.

4.1.1 Quasi-linear models for integrated simulation

Quasi-linear models have first been developed to be used as part of the integrated modelling framework. Indeed, the computational time saved not solving the non-linearities of the problem (see § 4.2) enables iterating the quasi-linear models a large number of times with a contained computational cost. The Weiland model [Weiland et al., 1989] was a noticeable step towards more theory-based quasi-linear model although the very basic assumptions carried out for its development can be questionned (in particular using the dominant mode at a unique wave number). A widely used series of quasi-linear models is the GLF (for gyro-Landau-fluid) series of codes [Waltz et al., 1997]. The novelty of the approach was to tune the model to fit linear gyro-kinetic and non-linear gyro-fluid simulations. Building on the GLF family, TGLF (for Trapped gyro-Landau-fluid) is based on a larger number of moment equations (15 instead of 8), uses an Hermite polynomial decomposition of the eigenfunctions instead of trial Gaussian and does not use the Padé approximation, enabling for higher k validity. Building on the progress of computational resources, all fitting of TGLF is based on gyro-kinetic simulations, either linear or non-linear. The model for the saturation has been recently revisited to improve TGLF ability for angular momentum transport predictions, in particular for the residual stress modelling [Staebler et al., 2013]. All the models presented above are fluid codes, necessitating closures and some tuning to match the linear gyro-kinetic response. The fact that QuaLiKiz is based on a gyro-kinetic solver [Bourdelle et al., 2002] and can still be run within an integrated framework represents most of its originality. Nonetheless, for the time being, it is much slower than TGLF and requires parallel computing when used in the integrated framework. Compared to TGLF, QuaLiKiz also lacks a more complete magnetic equilibrium and electro-magnetic effects.

4.1.2 Uses of quasi-linear model in integrated simulations

Most of integrated simulations focused on reconstructing the temperature profiles and modelling the turbulent heat transport since temperature and energy confinement are key elements of the tokamaks overall performance. Numerous simulations showed good agreement with experimental data especially in the case of standard H-modes (baseline for ITER) [Kinsey et al., 2008] but also for hybrid scenarii [Imbeaux et al., 2005] and experiments with internal transport barriers (ITBs) [Tala et al., 2006] with larger variation of the error between simulations predictions and experimental measurements [Imbeaux, 2009, Table 1].

Despite the success of these simulations, some open issues remain standing. First of all, the pedestal is not simulated in H-mode scenarii whereas it represents a significant part of the total stored energy of the plasma and mostly determined the pressure conditions in the core plasma as illustrated in Imbeaux [2009], Figure 24. Moreover, consistent transport under-predictions for $\rho \geq 0.8$ in low current L-modes were reported [Holland et al., 2013]. However, non-linear local gyro-kinetic simulations did not exhibits a closer agreement to the experiment in that case. The role of magnetic fluctuations, *i.e.* finite β effects, and the fast

particles should be more deeply studied given recent advances performed with non-linear gyro-kinetic simulations [Citrin, 2012]. Finally, given the recent advances in quasi-linear model for integrated modelling, a study of the synergy between all transport channels should be carried out on broader experimental range as started by Staebler et al. [2013].

4.1.3 Stand-alone quasi-linear modelling

Increasing computational resources enabled these recent years the use of linear gyro-kinetic simulations as a new standard for turbulence simulations. Therefore, using a quasi-linear model based on a parallelised linear gyro-kinetic solver such as GENE, GKW or GS2 became possible. From this ability, new results in the simulations of particle and impurity transport emerged for example on the particle flux reversal with collisionality [Angioni, 2010] or with changing dominant instability regime [Merz and Jenko, 2010]. For impurity transport, the importance of electron modes [Villegas et al., 2010] or of the roto-diffusion are now acknowledged [Camenen et al., 2009a, Angioni et al., 2011]. A lot of efforts were also devoted to angular momentum transport resulting in a better knowledge of its dependencies [Camenen et al., 2009b, Angioni et al., 2012]. However the quantitative predicting abilities of the stand alone approach is linked to the stiffness of the turbulent fluxes. Indeed, changing the gradients of temperature only by a few percent is sufficient to modify significantly the resulting heat flux. Since the gradients are imposed as an input of the codes in stand alone simulations, the experimental data pre-processing affects considerably the predicted fluxes as it will be illustrated in Chapter 5.

As a result, if not perfect, quasi-linear theory allows to gain some insight into turbulent transport mechanisms. Integrated simulations reproduces a wide range of experimental situations with correct orders of the turbulent fluxes. However, the region outside $\rho = /0.85$is not consistently modelled by these simulations seemingly due to global effects [Dif-Pradalier, 2013]. Given all the successes of quasi-linear models coupled to integrated framework, QuaLiKiz model has been extended to capture the effects of rotation on the turbulent fluxes and to model the angular momentum flux. Before going into the details of QuaLiKiz new abilities in sections 4.3 and 4.4, a detailed description of the quasi-linear fluxes construction is given in § 4.2.

4.2 Main principles for the derivation of quasi-linear fluxes

Since the pioneering papers [Drummond and Pines, 1962, Vedenov et al., 1962], quasi-linear theory has been developed to infer significant knowledge of the saturated turbulent state from the linear stability picture. Its validity remains an open field of research [Escande and Elskens, 2003, Besse et al., 2011]. This section aims to analyse its validity in the context of tokamak plasmas and to illustrate the construction of the saturated potential based on turbulence measurements and non-linear simulations. But first, the derivation of

the quasi-linear flux expression is given in the formalism used to derive the gyro-kinetic quasi-neutrality equation and the linear growth rates in Chapter 3.

4.2.1 Derivation of the quasi-linear diffusion equation

The quasi-linear theory is a mean field theory that studies the evolution of the distribution function at an intermediate time scale τ [Casati, 2010]:

- sufficiently large such that $\tau \gg \gamma^{-1}$ where γ is the growth rate of the linearly dominant unstable mode. Equivalently, the typical time scale of study is much larger than the time scale of the fluctuations;
- sufficiently small such that $\tau < t_0$, where t_0 is the macroscopic equilibrium evolution time.

This scale separation is crucial for the decomposition of the distribution function $f = f_0 + \bar{f}$ into an equilibrium and a fluctuating parts with $\langle f \rangle_\tau = f_0$. Vlasov equation (3.1) is therefore averaged over τ leading to:

$$\partial_t f_0 + \left\langle [\tilde{f}, \tilde{h}] \right\rangle = 0 \tag{4.1}$$

The averaged Poisson brackets can be expressed with the action-angle variables presented in chapter 2:

$$\left\langle [\tilde{f}, \tilde{h}] \right\rangle = \int_{t_0}^{t_0+\tau} \frac{\mathrm{d}t}{\tau} \int_0^{2\pi} \frac{\mathrm{d}\boldsymbol{\alpha}}{(2\pi)^3} \partial_{\boldsymbol{\alpha}} \tilde{f} \partial_{\mathbf{J}} \tilde{h} - \partial_{\mathbf{J}} \tilde{f} \partial_{\boldsymbol{\alpha}} \tilde{h} \tag{4.2}$$

A simple integration by parts on $\boldsymbol{\alpha}$ enables the identification of the Poisson bracket with a divergence thanks to the periodicity of $\bar{f}$ and $\bar{h}$ in $\boldsymbol{\alpha}$ (see § 2.2.3):

$$\left\langle [\tilde{f}, \tilde{h}] \right\rangle = \partial_{\mathbf{J}} \int_{t_0}^{t_0+\tau} \frac{\mathrm{d}t}{\tau} \int_0^{2\pi} \frac{\mathrm{d}\boldsymbol{\alpha}}{(2\pi)^3} \tilde{f} \partial_{\boldsymbol{\alpha}} \tilde{h} \tag{4.3}$$

By replacing $\bar{f}$ by its expression derived in (2.30), the Vlasov equation can be written as a diffusive equation[Bourdelle et al., 2007, Appendix A]

$$\partial_t f_0 = \nabla_{\mathbf{J}} \cdot \sum_{\mathbf{n},\omega} \mathbf{n} \Im \left(\frac{\mathbf{n} \cdot \partial_{\mathbf{J}} f_0}{\omega - \mathbf{n} \cdot \boldsymbol{\Omega}_{\mathbf{J}} + \imath o^+} \right) \left| \tilde{h}_{\mathbf{n}\omega} \right|^2 = D^{QL} \Delta f_0 \tag{4.4}$$

where the Laplacian Δ is taken in the Action coordinates $\{J_i\}_{i=\{1,3\}}$. The property that $\langle \exp(\imath(\mathbf{n}\alpha + \mathbf{n}'\alpha') - \imath(\omega t + \omega' t')) = \delta(\mathbf{n} + \mathbf{n}')\delta(\omega + \omega')$ was used in the previous equation along with $\tilde{h}_{-\mathbf{n},-\omega} = \tilde{h}^*_{\mathbf{n}\omega}$. The integral over α embedded in $\langle \cdot \rangle$ gives the Dirac function in $\mathbf{n}$ and the integral in time gives the Dirac function in ω. The latter identification is only possible if the intermediate time scale τ is much longer than the time scale of the fluctuation

$2\pi/\omega$ (or $1/\gamma$). From (4.4), the quasi-linear fluxes expression:

$$\Gamma^{QL} = \left\langle \sum_{\mathbf{n},\omega} \mathbf{n} \Im \left(\frac{\mathbf{n} \cdot \partial_{\mathbf{J}} f_0}{\omega - \mathbf{n} \cdot \mathbf{\Omega}_{\mathbf{J}} + \imath o^+} \right) |\tilde{h}_{\mathbf{n}\omega}|^2 \right\rangle_{\xi,\lambda} \tag{4.5}$$

is very close from the expression of the linearised gyro-kinetic equation (2.30). $|\tilde{h}_{\mathbf{n}\omega}|^2$ corresponds here to the saturated potential. Within the quasi-linear framework, this potential cannot be self-consistently determined since there is no saturation mechanism embedded in the theory. Therefore, it is constructed based on turbulence measurements and non-linear simulations [McKee et al., 2001, Hennequin et al., 2004, Casati et al., 2009]. Its construction is detailed in the next two sections. First, the problem of the frequency broadening of the resonance is issued with its implications on the turbulent transport. The characteristics of the non-linear k-spectrum of the saturated potential are reviewed later on. On the other hand, the remaining terms in the expression of Γ^{QL}, correspond to the linear response described in § 3.3.

4.2.2 Resonances and frequency broadening

Since the saturated state is reached, the frequency ω appearing in (4.4) is real and does not necessarily corresponds to the linear frequency determined in the previous chapter. In that case, the quasi-linear diffusion remains localised in phase-space at the resonant surfaces and there is no large scale transport. But the resonance is broadened by fluctuations forming islands of iso-perturbed Hamiltonian in phase-space, the KAM tori. According to the KAM theory [Kolmogorov, 1954, Arnold, 1963, Moser, 1962], when the islands overlap, KAM tori are reduced and stochasticity appears. If the overlap is large enough, a stochastic sea is created, enabling the exploration a large fraction of the phase space and creating a large scale transport. An intuitive criterion for the transition towards chaotic behaviour is the Chirikov parameter σ: the ratio of the island mean width to the distance between islands. If $\sigma \ll 1$, KAM tori are not destroyed, the resonating trajectories remain localised within the islands separatrix. If $\sigma > 1$, the system is chaotic, a large scale transport is possible [Chirikov, 1979].

In our problem, the distance between islands corresponds to the distance between resonant surfaces $d = 1/(k_\theta \hat{s})$. If the island mean width is in theory a non-linear quantity, a first estimate is the mode width defined in § 3.2.1. As illustrated in Romanelli et al. [2007, Appendix A], the ratio w/d is larger than unity for most cases. This means that a large scale transport via turbulence does happen in standard tokamak conditions. Therefore, taking into account the frequency broadening of the resonance by the Hamiltonian fluctuations is crucial for the correct prediction of the turbulent transport by quasi-linear models.

According to turbulent measurements, the frequency spectrum of the turbulent state is somewhere between Gaussian and Lorentzian [Hennequin et al., 2004, Casati et al., 2009]. Taking a finite imaginary part in ω in the expression of the quasi-linear flux (4.4), is equiva-

lent to taking a Lorentzian frequency spectrum for the saturated potential, the width of the Lorentzian being determined by the value of this imaginary part [Casati, 2010, Chapter 3]. This is called renormalised quasi-linear theory[Dupree, 1966, 1968, Orszag and Kraichna, 1967] and it is used in various quasi-linear models for tokamak turbulence [Weiland et al., 1989, Waltz et al., 1997, Staebler et al., 2005].

In physical terms, taking a Lorentzian shape for the frequency spectrum means that the transport is diffusive, the spectral width of the turbulence being proportional to k^2 [Krommes, 2002], [Casati, 2010, Chapter 4]. The validity of this physical assumption can be checked by investigating the values of the so-called Kubo number $\mathcal{K}$ [Kubo, 1963]. $\mathcal{K}$ quantifies the ratio of the typical time on which particles and waves interact τ_{wp} to a characteristic time τ_{NL} of the the non-linear evolution of the advecting field (the fluctuating electric potential in the case of electrostatic turbulence):

$$\mathcal{K} = \frac{\tau_{wp}}{\tau_{NL}} \tag{4.6}$$

When the ratio (4.6) is small the particles trajectories do not have the time to be strongly affected by the field patterns. Therefore, random walk processes accurately describe the transport phenomena. In the opposite scenario, the particle are *trapped into the field patterns* and the transport cannot be represented by a random walks. In tokamak conditions, the Kubo-like number was found to be lower than unity for a wide range of parameters[Casati et al., 2009, Citrin et al., 2012], indicating that quasi-linear theory can be used since an intermediate time scale exists between $1 : \gamma$ and t_0. A small Kubo-like number also advocates for a Lorentzian shape of the frequency spectrum.

A study of the cross-phases relations between particles, ions and electrons energy, and the fluctuating potential [see Dannert and Jenko, 2005, Casati et al., 2009, Figures 4-5] leads to the conclusion that taking the linear frequency found in the previous chapter for ω in (4.4) is correct for larger spatial scales ($k_\theta \rho_i < 0.5$). For smaller scales, the information about the linear state is lost in the saturated state and ω departs from the linear frequency since at smaller scales the Kubo number becomes larger, the particles are more easily trapped in the smaller patterns of the fluctuating potential.

Regarding the width of the frequency spectrum, comparisons between linear and non-linear gyro-kinetic simulations indicate that the frequency broadening is comparable to the linear growth rates, determined in the previous chapter, for larger spatial scales [Citrin et al., 2012]. It is also confirmed by turbulence frequency spectrum measurements [see Casati, 2010, Chapter 4]. As shown in the next section, larger spatial scales ($k_\theta \rho_i < 0.5$) mostly determine the turbulent transport. ω is therefore taken as the complex eigenvalue found by the linear solver presented in the previous chapter. Only positive growth rates are calculated thus the causality condition is respected.

4.2.3 Wave number spectrum and saturated potential amplitude

The perpendicular wave number spectrum of the saturated potential was found to peak around $k_\perp \rho_i = 0.2$ by turbulence measurements and non-linear gyro-kinetic simulations with a $k_\perp^{-3}$ slope for the cascade towards smaller scales found in non-linear simulations and experimentally measured [Hennequin et al., 2004, Gürcan et al., 2008, Casati et al., 2009]. This ensures that most of the turbulent transport, induced by the fluctuations of the electric potential, takes place at larger spatial scales where the hypothesis taken for the frequency: $\omega \equiv \omega_{\text{lin}}$ is verified.

For the inverse cascade at larger scales, it was found that a linear dependence reproduces best non-linear simulations (see Figure 4.1) although earlier turbulence measurements found a more symmetric shape for the wave number spectrum [McKee et al., 2001].

Building on the diffusive character of the turbulent processes at larger scales, a mixing length rule is employed to fix the wave number at which the saturated potential is maximum and its amplitude such that [Krommes, 2002]:

$$\max\left(\langle k_\perp^2 \rangle D_{\text{eff}}(k_\perp)\right) \approx \max\left(\gamma\right) \tag{4.7}$$

The relation (4.7) also uses the correspondence between the linear growth rate and the wave-particle interaction time $\tau_{wp} \approx \gamma^{-1}$ verified for larger scales.

In QuaLiKiz, the expression for $\langle k_\perp^2 \rangle$, based on the idea proposed by Dannert and Jenko [2005], has been recently revisited in Citrin et al. [2012] to improve the fluxes estimation at low magnetic shear. It reads:

$$\langle k_\perp^2 \rangle = k_\theta^2 + k_r^2 = k_\theta^2 + \left(\sqrt{k_\theta^2 \hat{s}^2 \langle \theta^2 \rangle} + \frac{0.4\exp(-2\hat{s})}{\sqrt{q}} + 1.5(k_\theta - 0.2/\rho_s)H(k_\theta - 0.2/\rho_s)\right)^2 \tag{4.8}$$

The expression of k_r in QuaLiKiz mixing length rule was modified because it was found that, at low magnetic shear, $k_r^2 = k_\theta^2 \hat{s}^2 \langle \theta^2 \rangle$ resulting from the magnetic field lines shearing is underestimated with respect to non-linear k_r [see Citrin et al., 2012, Sec. IV C.]. The factor $\frac{0.4\exp(-2\hat{s})}{\sqrt{q}}$ was found to represent best the non-linear isotropisation at low magnetic shear. Finally, the term $1.5(k_\theta - 0.2/\rho_s)H(k_\theta - 0.2/\rho_s))^2$ (H is the Heaviside function) is present to ensure a better agreement with non-linear gyro-kinetic simulations at higher k_θ values. This last part is of small impact on the resulting fluxes since most of the transport results from larger scales structures. This fit performed to match non-linear simulations at lower values of magnetic shear illustrates a limitation of the mixing length rule model. Indeed, the saturated potential amplitude is weakened possibly due to a stronger effect of damped modes and zonal flows at low magnetic shear which cannot be accounted for in the mixing length model as presented in (4.7).

Finally, the saturated potential amplitude is renormalised by a *fixed* parameter in order to have a correct value of the predicted fluxes [Peeters et al., 2006]. In QuaLiKiz, this renormalisation is performed such that the ion heat flux agrees with non-linear GYROsimulation for the GA-std case [Casati et al., 2009]. This renormalisation parameter is another limitation of the mixing length rule since there is no physical explanation for its value. Building a reduced model that quantitatively predicts the saturated potential amplitude without renormalisation appears as real challenge left for future work.

As a conclusion, the quasi-linear models have shown their abilities to predict heat, particle and momentum fluxes in various experimental conditions validating the choice to model the transport phenomena by diffusive processes. However, turbulence measurements and non-linear simulations indicate that the physical picture is not complete with this approach. Indeed, the frequency spectrum of the density fluctuations departs from a Lorentzian shape [Casati et al., 2009] and non-linear heat fluxes departs from a Gaussian statistics [Abiteboul et al., 2013]. Building on the successes of the quasi-linear approach, one can think that non-diffusive processes take place at smaller spatial scales than those crucial for the evaluation of the turbulent transport. This is supported by the fact that, at smaller spatial scales, the non-linear characteristic times should be smaller due to a smaller characteristic size for the field patterns. Therefore, the Kubo-like numbers should be higher.

4.3 Quasi-linear fluxes in presence of rotation in QuaLiKiz formalism

Including the effects of a sheared rotation of the plasma on the turbulent fluxes was the main objective of this work. They will be illustrated in this section and the next. In this section attention is focused on the derivation of the momentum flux, and the modification of the saturated potential by a sheared rotation.

The expression of the particle and heat fluxes such as used in QuaLiKiz and extensively studied in previous works by Bourdelle et al. [2007], Casati et al. [2009], Citrin et al. [2012] is reminded:

$$\Gamma_s = \Re \left\langle n_s \bar{f}_s \frac{\imath k_\theta \bar{\phi}}{B} \right\rangle \tag{4.9a}$$

$$Q_s = \Re \left\langle T_s \bar{f}_s \frac{\imath k_\theta \bar{\phi}}{B} \right\rangle \tag{4.9b}$$

The factor k_θ/B appearing in the relations above and not in (4.4) comes from the expression of the flux ψ in the circular equilibrium used in QuaLiKiz. Multiplied by the fluctuating potential $\bar{\phi}$, the ratio gives the fluctuating electric velocity $n\omega_E$. Therefore, the quasi-linear fluxes can be interpreted as the advection of the quantity of interest (density, energy, angular momentum) by the fluctuating electric velocity thanks to this reformulation.

4.3.1 The momentum flux derivation

Calculating the angular momentum flux, $\Pi_\parallel$, is the main objective of the present work, explaining all the modifications to the QuaLiKiz code presented in this work. The equal importance of the eigenfunction and linear growth rate modifications by the plasma rotation will be illustrated. As shown in Peeters et al. [2011], the momentum flux is finite only if the parallel symmetry is lost. In QuaLiKiz framework, this is possible only in presence of a finite (sheared or not) parallel rotation and/or $\mathbf{E}\times\mathbf{B}$ shear. In these cases, the eigenfunctions are shown to loose their symmetry in θ (see § 3.2.2). The impact of the eigenfunction asymmetrisation will be illustrated in the next section, but let us concentrate on the expression of the angular momentum for now.

Rigorously, the toroidal momentum flux Π_φ is the quantity to calculate since the total toroidal momentum is a conserved quantity [Abiteboul et al., 2011]. In large aspect ratio tokamaks, the flow is mostly parallel [Newton et al., 2010]. Therefore, the parallel component of the toroidal momentum flux is much larger than its perpendicular one; making the parallel momentum flux $\Pi_\parallel$ a good proxy of Π_φ:

$$\Pi_\parallel = \sum_s \Re\left\langle m_s R v_\parallel \bar{f}_s \frac{\imath k_\theta \bar{\phi}}{B} \right\rangle \tag{4.10}$$

$\bar{f}_s = \sum_{\mathbf{n}} e_s J_0 \cdot \frac{\mathbf{n}\partial_{\mathbf{J}} f_0^s}{\omega - \mathbf{n}\mathbf{n}\cdot\mathbf{\Omega}_{\mathbf{J}} + \imath 0^+}\bar{\phi}$ is the perturbed distribution function determined by the linearised gyro-kinetic electro-neutrality equation. R is the tokamak major radius averaged over a flux surface. In the large aspect ratio approximation, the radius of the magnetic axis R_0 is used instead of R disregarding the corrections in ϵ brought by the latter term.

Using the formalism developed in § 3.3, the complete expression of $\Pi_\parallel$ is:

$$\begin{aligned}\Pi_\parallel = -\sum_{\epsilon_\parallel=\pm1,s,n} n_s m_s \left(\frac{nq}{rB}\right)^2 \Bigg\langle \epsilon_\parallel \sqrt{1-\lambda b}\,\xi e^{-\xi}\left(1 + 2\frac{u_\parallel}{v_{Ts}}\epsilon_\parallel\sqrt{\xi(1-\lambda b)} + \frac{u_\parallel}{v_{Ts}}^2(2\xi(1-\lambda b)-1)\right)\\ \left[\frac{R\nabla n_s}{n_s} + \left(\xi - \frac{u_\parallel}{v_{Ts}}\left(2\epsilon_\parallel\sqrt{\xi(1-\lambda b)} - \frac{u_\parallel}{v_{Ts}}\right) - \frac{3}{2}\right)\frac{R\nabla T_s}{T_s} + \right.\\ \left. 2\left(\epsilon_\parallel\sqrt{\xi(1-\lambda b)} - \frac{u_\parallel}{v_{Ts}}\right)\frac{R\nabla u_\parallel}{v_{Ts}} + \frac{\varpi}{n\omega_{ds}}\right]\Im\left(\frac{1}{\omega - n\Omega_J(\xi,\lambda) + \imath 0^+}\right)\left|\bar{\phi}_{n\omega}\right|^2\Bigg\rangle_{\xi,\lambda,k_r}\end{aligned} \tag{4.11}$$

Compared to (3.32) and (3.39), the expression of the momentum flux has the opposite parity in ξ and λ due to the multiplication by $v_\parallel = \sqrt{\xi(1-\lambda b)}$. Otherwise, the expression is similar. The same techniques as before are then employed. The contributions from trapped

and passing particles to the momentum flux are treated separately:

$$\Pi_{\parallel} = -\sum_{\epsilon_{\parallel}=\pm 1,s,n} n_s\sqrt{2m_sT_s}\left(\frac{nq}{rB}\right)^2\Big\{\mathcal{J}_{s,tr}\int\frac{\mathrm{d}k_r}{2\pi}\mathcal{B}_0(k_\theta\rho_s)\mathcal{B}_0(k_r\delta_s)|\tilde{\phi}_n(k_r)|^2 + \int_{-\infty}^{\infty}\frac{\mathrm{d}k^*}{\sqrt{\pi}}e^{-k^{*2}}\int_{-\infty}^{\infty}\frac{\mathrm{d}\rho^*}{\sqrt{\pi}}e^{-\rho^{*2}}\Re(\mathcal{J}_{s,pass}(k^*,\rho^*))\mathcal{B}_0(k_\theta\rho_s)\left|\tilde{\phi}_n\right|^2 \tag{4.12}$$

The expression for $\mathcal{J}_{s,pass}$ is detailed in (4.13). Due to the multiplication of the functionals by v, the even functions of (3.32) — $Z_1(v)$, $Z_2(v)$, $Z_3(v)$ — become odd functions — $vZ_1(v)$, $vZ_2(v)$, $vZ_3(v)$ — in the momentum flux expression. Combined with the fact the even functions are multiplied by $u_{\parallel}$ or $\nabla u_{\parallel}$, the momentum flux is zero in the absence of rotation as expected [Peeters et al., 2011].

$$\begin{aligned}\mathcal{J}_{s,pass} =& \frac{2}{f_\theta}\left[A_{Ts}\frac{V_+Z_2(V_+)-V_-Z_2(V_-)}{V_+-V_-}+\left(A_{ns}-\frac{3}{2}A_{Ts}-\frac{\varpi}{n\bar{\omega}_{ds}}\right)\frac{V_+Z_1(V_+)-V_-Z_1(V_-)}{V_+-V_-}\right]\\ &+\frac{4}{3f_\theta}\left[\frac{u_{\parallel}}{v_{Ts}}A_{Ts}\frac{Z_3(V_+)-Z_3(V_-)}{V_+-V_-}+\left(A_u+\frac{u_{\parallel}}{v_{Ts}}\left(A_{ns}-\frac{5}{2}A_{Ts}-\frac{\varpi}{n\bar{\omega}_{ds}}\right)\right)\frac{Z_2(V_+)-Z_2(V_-)}{V_+-V_-}\right]\\ &+\frac{u_{\parallel}}{f_\theta v_{Ts}}\left[\frac{u_{\parallel}}{v_{Ts}}A_{Ts}\frac{V_+Z_3(V_+)-V_-Z_3(V_-)}{V_+-V_-}+\left(2A_u+\frac{u_{\parallel}}{v_{Ts}}\left(A_{ns}-\frac{7}{2}A_{Ts}-\frac{\varpi}{n\bar{\omega}_{ds}}\right)\right)\frac{V_+Z_2(V_+)-V_-Z_2(V_-)}{V_+-V_-}\right]\\ &-\frac{2u_{\parallel}}{f_\theta v_{Ts})}\left[\frac{u_{\parallel}}{v_{Ts}}A_{Ts}\frac{V_+Z_2(V_+)-V_-Z_2(V_-)}{V_+-V_-}+\left(2A_u+\frac{u_{\parallel}}{v_{Ts}}\left(A_{ns}-\frac{5}{2}A_{Ts}-\frac{\varpi}{n\bar{\omega}_{ds}}\right)\right)\frac{V_+Z_1(V_+)-V_-Z_1(V_-)}{V_+-V_-}\right]\end{aligned} \tag{4.13}$$

For trapped particles, the multiplication by $v_{\parallel}=\sqrt{\xi(1-\lambda b)}$ implies there is no contribution to the momentum flux at lowest order in ϵ because the corresponding terms are odd in ξ. However, the term in $\sqrt{\epsilon}$ is even in ξ. Therefore the trapped particles bear a small net contribution:

$$\mathcal{J}_{s,tr} = 2\bar{\omega}_b\left[\left(A_u+\frac{u_{\parallel}}{v_{Ts}}\left(A_{ns}-\frac{5}{2}A_{Ts}-\frac{\varpi}{n\bar{\omega}_{ds}}\right)\right)\frac{Z_2(z)}{z}+\frac{u_{\parallel}}{v_{Ts}}A_{Ts}\frac{Z_3(z)}{z}\right] \tag{4.14}$$

Given the expressions of the passing and trapped particle contributions to the momentum flux, (4.11) can formally be written in the form:

$$\Pi_{\parallel} = \sum_s m_sn_sR(-\chi_{\parallel}\nabla u_{\parallel}+V_{\parallel}u_{\parallel})+\Pi_{RS} \tag{4.15}$$

$\chi_{\parallel}$ represents the momentum diffusivity, $V_{\parallel}$, the momentum pinch and Π_{RS} being the residual stress.

However, the identification of $\chi_{\parallel}$, $V_{\parallel}$ and Π_{RS} with (4.11) is not as straightforward as it may appear. From (4.13) and (4.14), it is clear that $\Pi_{\parallel}$ contains terms directly proportional to $u_{\parallel}$ and $\nabla u_{\parallel}$. They are called Π_u and $\Pi_{\nabla u}$. They do not contain all contributions from $u_{\parallel}$ and $\nabla u_{\parallel}$. Indeed, the remaining terms are proportional to the linear eigenfunction shift $\mathbf{x}_0$ which, itself, is proportional to $\nabla u_{\parallel}$, $u_{\parallel}$ and γ_E as expressed by (3.28) from § 3.2.1[Gürcan et al., 2007]. These terms, proportional to the eigenfunction shift, are called Π_{x0}. They

correspond to the only terms which are not multiplied by $u_\parallel$ or $\nabla u_\parallel$ in (4.13). If the $\mathbf{E}\times\mathbf{B}$ shear is the only symmetry breaker, $\Pi_{\mathrm{x0}} \equiv \Pi_{RS}$. Otherwise, $\Pi_{\mathrm{x0}} \propto u_\parallel, \nabla u_\parallel, \gamma_E$ cannot be identify with Π_{RS} as $\Pi_{\nabla u}$ (resp. Π_u) does not contain all conductive (resp. convective) contributions to the momentum flux. Comparing the results given by this direct separation with the actual conductive and convective contributions to the momentum flux gives an estimate of the importance of the eigenfunction contribution as evaluated in § 4.4. As for the residual stress, it would be strictly zero in the absence of a shift of the eigenfunctions.

4.3.2 Modification of the saturated potential in presence of rotation

The saturated potential is also modified by the introduction of a finite rotation of the plasma on two points: the frequency spectrum and the mixing length rule.

As explained in the previous section, the frequency spectrum is a Lorentzian of width γ modified at low magnetic shear values. In the case of simulations with large $\mathbf{E}\times\mathbf{B}$ shear, the width is modified. Indeed, if $\gamma_E > \gamma$, the shear rate defines a shorter time scale than the linear growth rate. The width of the Lorentzian is therefore taken as $\max(\gamma(k), \gamma_E)$. This rule would need to be validated against non-linear gyro-kinetic simulations. It implies a high resolution diagnostic for the frequency that deals correctly with the implementation of the $\mathbf{E}\times\mathbf{B}$ shear. To our knowledge, such a diagnostic does not exist yet but should be developed to address more quantitatively the evolution of the saturated potential frequency spectrum with the $\mathbf{E}\times\mathbf{B}$ shearing.

The mixing length rule is linearly modified by the modification of the linear growth rate. The definition for the mixing length rule is also modified by the linear eigenfunction shift $\mathbf{x}_0$ proportional to the symmetry breakers (3.28). Indeed, the linear eigenfunction enters the expression of $\langle k_\perp^2 \rangle$ in (4.8) through $\langle \theta^2 \rangle$:

$$\langle \theta^2 \rangle = \frac{\int \theta^2 \tilde{\phi} \mathrm{d}\theta}{\int \tilde{\phi} \mathrm{d}\theta} = \frac{2d^2}{\Re(\mathrm{w}^2)} \frac{\Gamma(0.75)}{\Gamma(0.25)} + \frac{\Im(\mathbf{x}_0)^2 d^2}{\Re(\mathrm{w}^2)^2} \tag{4.16}$$

Therefore, the symmetry breakers influence $\langle k_\perp^2 \rangle$ through the imaginary part of the eigenfunction shift $\Im(\mathbf{x}_0)$ and the real part of the mode width, the latter being proportional to the growth rate found in the fluid model. Thus, both γ (see Sec. 3.3.2) and $\langle k_\perp^2 \rangle$ are modified in the presence of finite sheared rotation.

The modification of $\tilde{\phi}_{sat}$ induced by $\mathbf{E}\times\mathbf{B}$ shearing are plotted and compared to non-linear GKW saturated potential [Casson et al., 2009] in Figure 4.1. In the simulations presented here, GA-std case parameter set has been employed with $u_\parallel = \nabla u_\parallel = 0$. Three values of $\mathbf{E}\times\mathbf{B}$ shear are chosen corresponding to an experimentally relevant range of γ_E from 0 to $0.5R/v_{Ti}$. The $k_\theta \rho_s$ extent covered in Figure 4.1 corresponds to the transport relevant spectral range.

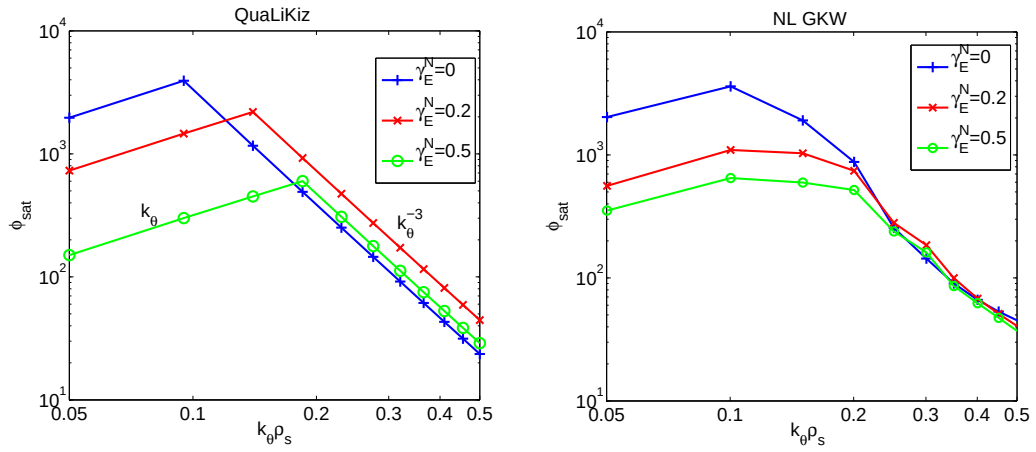

Figure 4.1: QuaLiKiz $\tilde{\phi}_{sat}$ estimate (left panel) and GKW non linear saturated potential. Simulations with $\mathbf{E}\times\mathbf{B}$ shear only. γ_E values in v_{Ti}/R units. GKW data: courtesy of F.J. Casson[Casson et al., 2009]

For both QuaLiKiz and non-linear GKW, as $\mathbf{E}\times\mathbf{B}$ shear is increased, the amplitude of the saturated potential is reduced at the largest scales (lowest wave numbers). In QuaLiKiz, this is due to a shift of the maximum of the saturated potential towards smaller scales corresponding to the usual picture of the non-linear effect of the $\mathbf{E}\times\mathbf{B}$ shear. In GKW, a flattening of the saturated potential amplitude is rather observed around its maximum. However, in the case of pure ITG, *i.e.* adiabatic electrons, a spectral shift of the maximum towards smaller scales is observed in GKW [Casson et al., 2009]. Both codes exhibit a weak dependence of their saturated potential with γ_E at $k_\theta\rho_s > 0.2$. Quantitatively, in QuaLiKiz, the reduction of the saturated potential maximum amplitude is underestimated at lower $\mathbf{E}\times\mathbf{B}$ and overestimated at higher $\mathbf{E}\times\mathbf{B}$ shear values.

Despite the quantitative differences, the non-linear quenching with $\mathbf{E}\times\mathbf{B}$ shear is captured qualitatively with a shifted eigenfunction calculated in the fluid limit and a simple mixing length rule estimate for the saturation level. In the next section, the quasi-linear fluxes are compared to non-linear simulations and the influence of the saturated potential of the fluxes is further discussed.

4.4 Validation of QuaLiKiz fluxes versus quasi-linear and non-linear simulations

To finally evaluate the model presented above, the resulting heat, particle and momentum fluxes are compared to non linear simulations. First, the impact of the $\mathbf{E}\times\mathbf{B}$ shear alone is studied in Figure 4.2, i.e. $u_\parallel$ and $\nabla u_\parallel$ are set to 0. GA std case parameters are used to compare QuaLiKiz predictions with published results from non-linear GYRO [Staebler et al.,

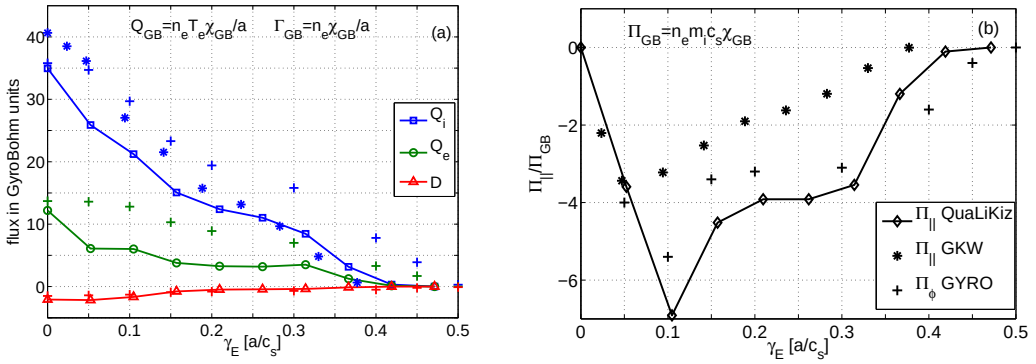

Figure 4.2: (a) Ion and electron heat fluxes, particle flux and (b) angular momentum flux for GA-std parameters. Here $\Pi_{||} \equiv \Pi_{RS}$ since $u_{||} = \nabla u_{||} = 0$. The solid lines are QuaLiKiz results, the stars $*$ are GKW data from [Casson et al., 2009] and the crosses $+$ are GYRO data from [Staebler et al., 2013]. a/c_s units have to be multiplied by $3/\sqrt{2}$ to have their R/v_{Ti} equivalent.

2013] and GKW[Casson et al., 2009]. The conductive and convective contributions to the momentum fluxes are analysed later on and compared to non-linear GKW findings. The influence of the eigenfunction shift on both contributions will also be discussed.

4.4.1 Evolution of the fluxes in presence of radial electric field shearing

For GA-std case parameters, QuaLiKiz ion and electron heat and particle fluxes are smoothly reduced and quenched for $\gamma_E > 0.4 c_s/a$ as illustrated in Figure 4.2(a). This quench value is lower than what is found by GYRO simulations (crosses in Figure 4.2(a)[Staebler et al., 2013, Figure 1]) but is in agreement with the value obtained with GKW(stars in Figure 4.2(a) [Casson et al., 2009, Table II]) using non-linear GKW. QuaLiKiz predictions should be compared in priority against GKW since GYRO was run with Miller's equilibrium in Staebler et al. [2013] whereas QuaLiKiz and GKW use an $\hat{s} - \alpha$ equilibrium. QuaLiKiz predictions for the heat and particle fluxes is somewhat lower than both non-linear GKW and non-linear GYRO. Please notice that QuaLiKiz ion heat flux is fixed to GYRO level for $\gamma_E = 0$ in the presented GA-std case. In GYRO, the fluxes reduction with increasing $\mathbf{E} \times \mathbf{B}$ shear is notably slower than the reduction found with GKW and QuaLiKiz which are almost equivalent as illustrated by Figure 4.2(a). This may be caused by the different equilibrium employed.

The angular momentum flux $\Pi_{||}$ is presented in Figure 4.2(b). As $u_{||}$ and $\nabla u_{||}$ are set to zero, $\Pi_{||}$ corresponds to the residual stress Π_{RS} in this case. In absolute value, the momentum flux increases at first with γ_E due the $\mathbf{E} \times \mathbf{B}$ shear asymmetrisation of the eigenfunction. Then, the momentum flux is slowly reduced due to the turbulence quenching by the $\mathbf{E} \times \mathbf{B}$ shear. QuaLiKiz is in qualitative agreement with non-linear simulations. Quantitatively, QuaLiKiz overestimates the momentum flux found with GKW by a factor 2 for $\gamma_E \geq 0.2 R/v_{Ti}$. The agreement with GYRO simulations is better but is explained by the

fact that fluxes are found higher using Miller's equilibrium rather than $\hat{s} - \alpha$ [Lapillonne et al., 2009]. For experimental interpretations and predictions, the fact that $\hat{s} - \alpha$ and Miller's equilibria give substantially different momentum fluxes calls for the implementation of a more complete magnetic equilibrium in QuaLiKiz and more comparisons between the momentum fluxes computed with each equilibrium. Indeed, the momentum flux has been shown to be particularly sensitive to the magnetic equilibrium geometry [Camenen et al., 2009b]. Nevertheless, GYRO ion heat flux is surprisingly lower than GKW's in the absence of electric field shearing. The discrepancy between QuaLiKiz and GKW is thought to be related to the overestimation of the saturated potential amplitude at lower $k_\theta \rho_s$ and intermediate values of γ_E in QuaLiKiz illustrated in the previous section (see Figure 4.1). All in all, the $\mathbf{E} \times \mathbf{B}$ induced residual stress for $\gamma_E < 0.05$ provided by QuaLiKiz is in agreement with non-linear models. At larger values, the prediction is overestimated by a factor ~ 2. We may stress that computing successfully the $\mathbf{E} \times \mathbf{B}$ induced residual stress with a reduced model, compatible with integrated modelling, is a very recent breakthrough [Staebler et al., 2013]. The mechanisms by which $\mathbf{E} \times \mathbf{B}$ shearing transports momentum can be understood as a creation of a poloidal asymmetry. The idea that a shift in the ballooning angle θ_0 due the $\mathbf{E} \times \mathbf{B}$ shearing is responsible for both turbulence quenching and momentum driving has also been successfully used in Staebler et al. [2013].

4.4.2 Conductive and convective contributions to the momentum flux

Now, the effect of $\nabla u_\parallel$ and $u_\parallel$ on the momentum flux are analysed. To perform this analysis, the following non dimensional quantities are employed: The Prandtl number $\frac{\chi_\parallel}{\chi_i}$ and the pinch number $\frac{RV_\parallel}{\chi_\parallel}$. The Prandtl number is the ratio of the viscosity to the diffusivity and the pinch number the ratio of the momentum convection to the viscosity. Therefore, for a given heat flux (mainly diffusive), the Prandtl gives the stiffness of the momentum flux to the velocity gradient. The pinch number represents the balance between diffusive and convective behaviour for the momentum flux. They facilitate the comparison with non-linear simulations and with experimental analysis where they have been extensively investigated as the saturated potential does not appear in these ratios.

Isolating the conductive and convective contributions to the momentum flux is not straightforward due to the eigenfunction shift dependences presented in § 4.3.1 contributing to the momentum flux (Equations (4.13) and (4.14)). To evaluate the *total* conductive part of the momentum flux, a simulation with only $\nabla u_\parallel$ as a symmetry breaker ($u_\parallel = \gamma_E = 0$) is performed. The ratio of the momentum flux to the ion heat flux then gives the Prandtl number. To evaluate the *total* convective part, a simulation with only $u_\parallel - \nabla u_\parallel = \gamma_E = 0$ – is carried out. The ratio between the resulting momentum flux to the previous $\nabla u_\parallel$-only momentum flux gives the pinch number. Using this method, the contribution of the eigenfunction shift to the conductive and convective parts of the momentum flux can be quantified. In the following, this method is called the *2-point method* since it is a regression based on two points of the parameter space.

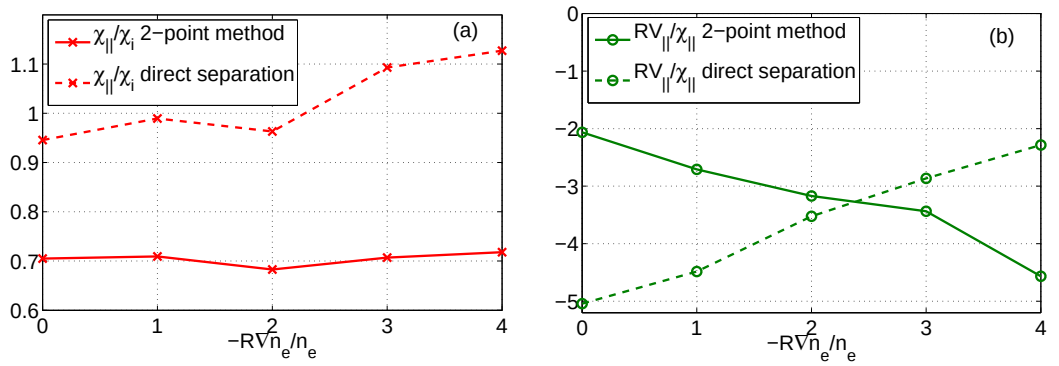

Figure 4.3: (a) Prandtl (red crosses) and (b) pinch number (green circles) calculated with the *direct separation method* (dashed curves) and with the *2-point method*[Peeters et al., 2011] (plain curves)

Two QuaLiKiz simulations based on GA-std case parameter set are performed for the validation of the conductive and convective contributions to the momentum flux calculated by the 2-point method:

- one with $\frac{-R\nabla u_\parallel}{v_{Ti}} = 1$, $\frac{u_\parallel}{v_{Ti}} = 0$;
- one with $\frac{-R\nabla u_\parallel}{v_{Ti}} = 0$, $\frac{u_\parallel}{v_{Ti}} = 0.2$.

As explained in Sec. 4.3.1, a direct extraction of a $\Pi_{\nabla u}$ and a Π_u – corresponding to diffusive and convective contributions to the momentum transport *without* taking the eigenfunction shift effect into account – is possible in QuaLiKiz. This method called the *direct separation method* is compared to the 2-point method in Figure 4.3 to give an idea of the impact of the eigenfunction shift on $\chi_\parallel$ and $V_\parallel$.

The normalised density gradient R/L_n was varied from 0 to 4. Indeed, results from non-linear gyro-kinetic simulations indicate a strong correlation between R/L_n and the pinch number [Peeters et al., 2007, 2011], the Prandtl number being weakly correlated. In Figure 4.3, the Prandtl number is displayed with crosses and the pinch number with circles, the results from the 2-point method being in plain curves and the estimations via direct separation in dashed curves.

The Prandtl number deduced from the 2-point method is found to be close to 0.7 agreeing with quasi-linear [Peeters and Angioni, 2005] and non-linear simulations[Peeters et al., 2011]. Due to the omission of the eigenfunction shift effect, the direct separation in QuaLiKiz gives a higher Prandtl number, close to one, as predicted in early theoretical calculations[Mattor and Diamond, 1988]. Using the 2-point method, the pinch number $\frac{RV_\parallel}{\chi_\parallel}$ is found to vary from -2 to -5, with a strong correlation with R/L_n, as in [Peeters et al., 2011]. When neglecting the eigenfunction shift effects, *i.e.* with the direct separation technique, the correlation with R/L_n is inverted. This behaviour is all the more surprising that simple fluid

models considering $k_{\|} = 0$ recover the right R/L_n correlation Peeters et al. [2007, 2009a]. This inverted correlation may be caused spurious effects of the direct separation technique (since part of the functionals are cut out for the fluxes computation in this case). Taking the ratio of the momentum fluxes amplifies the error. The eigenfunction shift effect is therefore important to have the correct dependencies and values of the different contributions to the momentum flux. Hence, the fact that QuaLiKiz correctly models the R/L_n impact and gives correct values for both the Prandtl and the pinch numbers, is a strong indication that the model used in QuaLiKiz is appropriate to compute the momentum fluxes. Additional comparisons with non-linear gyro-kinetic simulations could be performed for various safety factor or magnetic shear values. However, due to the lack of other strong correlations in non-linear results, such comparisons were not carried out in this work.

*
* *

In this chapter, the quasi-linear approximation was briefly presented. Thanks to numerous theoretical works and comparisons with non-linear simulation, quasi-linear theory has been validated in tokamak plasmas conditions, at least at larger spatial scales, most relevant for turbulent transport. At smaller scales, the quasi-linear approximation starts failing due to the loss of the time scale separation, particle being trapped in the field patterns. Since the fluxes are mostly induced by the large scales structures, the quasi-linear estimations are comparable to non-linear simulations. The momentum flux calculated with QuaLiKiz successfully reproduces non-linear simulations, including the momentum diffusivity, the momentum pinch and the residual stress. *For the conductive and convective parts of the momentum flux, two methods are compared to underline the importance of the eigenfunction shift contribution. The influence of* $\mathbf{E} \times \mathbf{B}$ *shearing on particle and heat fluxes is also addressed. The resulting quenching values and the fluxes amplitudes are in agreement with non-linear calculations given the variations between non-linear gyro-kinetic simulations.*

5

Comparing quasi-linear momentum fluxes with experimental results

This chapter is focused on comparing momentum flux modelled by QuaLiKiz with experimental results. Such a comparison is performed through the analysis with QuaLiKiz of NBI modulations experiments carried out at JET by Tala et al. [2009]. Before comparing QuaLiKiz predictions against experimental measurements, it appears essential to introduce the main diagnostics used to provide the velocity data.

5.1 What experiments to characterise the angular momentum?

Before confronting QuaLiKiz results to the experiments, the diagnostics making the comparison possible are briefly presented to illustrate the issues linked to the analysis of the experiments. The importance of the experiment studied later on the course of this chapter is then put in context. At this point, a brief review of the evolution of the momentum transport understanding is given.

5.1.1 What diagnostics to measure the plasma rotation?

Two major techniques employed to measure the plasma rotation are presented in this first section. Both techniques are active diagnostics and use the Doppler frequency shift of the signal to access the velocity. The techniques are otherwise quite different from one another: Charge eXchange Recombination Spectroscopy (CXRS) analyses the spectroscopic signature of the interaction of a highly energetic neutral beam with the plasma whereas Doppler reflectometry (DR) analyses the back-scattering of a centimetric wave by the plasma. The measured velocities are also different: CXRS captures the toroidal bulk velocity and in some

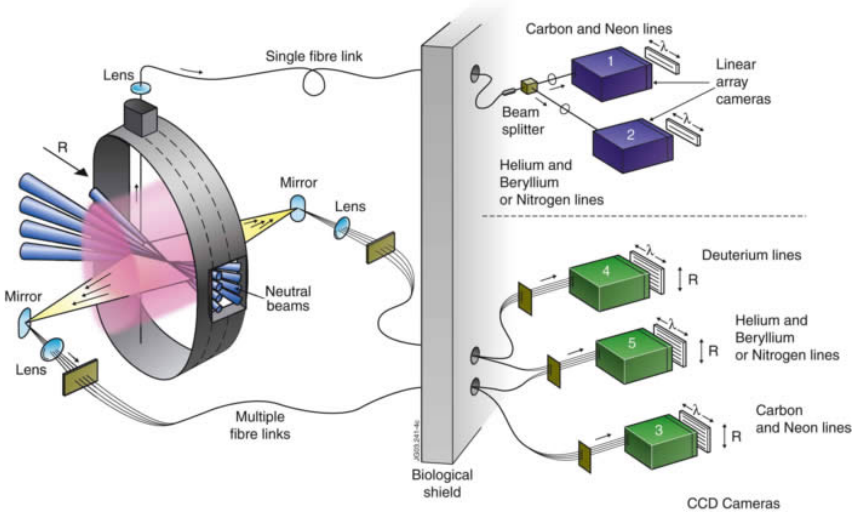

Figure 5.1: Charge exchange recombination lines of sight (yellow) and neutral beam injector (blue) in JET [JET EFDA, 2013]

cases also the poloidal [Viezzer et al., 2012] whereas DR gives access the fluctuations velocity leading to the radial electric field as explained in the following.

5.1.1.1 Charge eXchange Recombination Spectroscopy

Charge exchange spectroscopy consists in launching a beam of highly energetic particles in the plasma, typically at 55 keV in Tore Supra and up to 140 keV in JET [von Hellermann et al., 2005] and analysing the electron recombination emission of the plasma with a spectrometer as illustrated in Figure 5.1. Various spectral lines of light impurities can be measured. For signal over noise ratio quality reasons, they correspond to the main impurities of the plasma: Carbon (C VI) for carbon-wall machines, Boron after boronisation [Angioni et al., 2011], or the injected impurity: Helium (He II), Neon, Argon, in the case of impurity seeding experiments. However, advances in the D_α emission modelling enabled for a direct measurement of the deuterium velocity in DIII-D [Grierson et al., 2012, 2013]. CXRS measures the temperature of the considered ion via the broadening of the spectral lines, hence not directly the main ion temperature. Since the recombination emission wavelengths are documented with accuracy in the atomic database (ADAS), the Doppler shift of the considered spectral line can be precisely determined. The ion rotation is measured in the direction of the spectrometer lines of sight which is typically tangential. As the radial component of the particle velocity is much smaller than its toroidal component, the toroidal velocity of the considered ion species can be extracted. Systems resolving the poloidal velocity are also developed example [Viezzer et al., 2012, Bortolon et al., 2013].

Using Helium plasmas, the equivalence between impurities and main ions velocities was shown to fail in low plasma current discharges with high temperature gradients *i.e.* significant only at the edge of H-mode plasma since they exhibit large pressure gradients [Kim et al., 1994]. More recent experiments on DIII-D, where a direct measurement of Deuterium velocity is possible, showed that deuterium and carbon velocities can be different either in ECH H-modes or more significantly in the presence of ITBs [see Grierson et al., 2012, Figures 8,14]. In contrast, the temperature of Carbon is shown to coincide with the temperature of Deuterium in all cases.

In TCV, the diagnostic neutral beam injector was designed to access the plasma up to the high field side of the machine since it has no intended contribution to the plasma heating. Therefore, the in-out asymmetry of the toroidal rotation can be measured and be linked to the poloidal rotation thanks to neoclassical theory [Kim et al., 1991]. This way the poloidal rotation can be inferred from the toroidal rotation shunting the difficulties linked to the measurement of the rather small poloidal velocities. Due to the good accuracy of the method, an estimation of the radial electric field is possible via the radial force balance equation [see Bortolon et al., 2013, Figure 6]. For radial electric field measurements, a new high resolution poloidal charge exchange has been recently installed in ASDEX Upgrade [Viezzer et al., 2012]. As the radial electric field is thought to play an important role in the L-H transition and the active CX signal is attenuated with decreasing plasma radius, the poloidal charge exchange gives access only to the plasma edge. Combining poloidal and toroidal CX measurements enables for a precise reconstruction of the radial electric field which can be compared to the Doppler Reflectometry measurements [see Viezzer et al., 2013, Figure 5].

5.1.1.2 Doppler reflectometry

Reflectometry is an active technique developed to analyse the density fluctuations in the tokamak plasmas [see Conway, 2006, for an overview]. A microwave is launched in the plasma. Since the transmission coefficient of microwaves decreases with the plasma density, a cut-off layer is defined inside the plasma and the wave is reflected. The cut-off density depends also on the frequency of the wave. Therefore, the density profile is reconstructed with a scan in frequency and a measure of the *time of flight* of the wave [Moreau et al., 2000]. Reflectometry can also be used at fixed frequency to access information about density fluctuations at the cut-off surface. Under the Born approximation, the phase variation of the reflected wave is proportional to the density fluctuations $\delta n/n$[Sabot et al., 2006]. If the equilibrium density is known, the density fluctuations can be followed in time with this technique. However, accessing the rotation velocity of the fluctuations is not possible with this technique due to the lack of wave number selection.

To have access to the fluctuations velocity, back-scattering techniques are combined with reflectometry. Indeed, the fluctuations of density are known to induce back-scattering

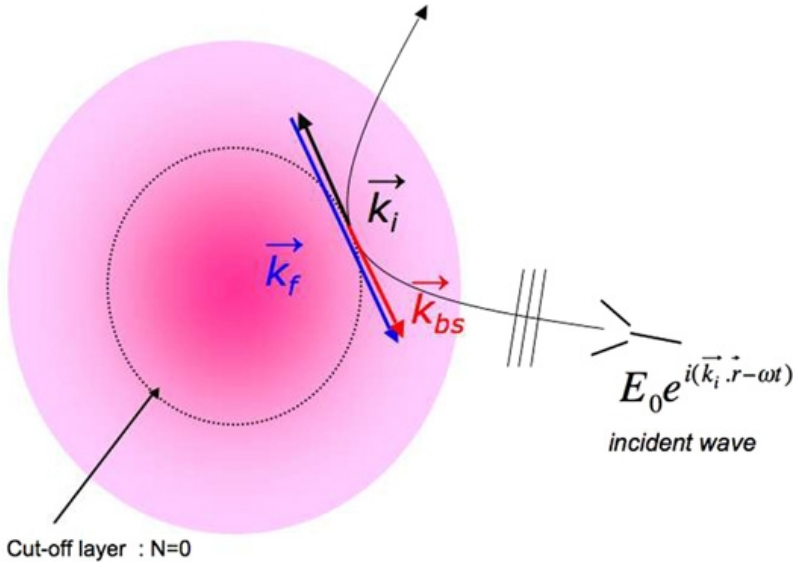

Figure 5.2: Schematic representation of the Doppler reflectometry technique [Vermare et al., 2011]

of the electro-magnetic waves [Truc et al., 1992]. Back-scattering is a also known for its wave number selecting abilities since Bragg. By launching the microwave in an oblique direction (with respect to the normal of the iso-index surfaces), the back-scattered signal is decoupled from the reflected signal enabling its analysis. Back-scattering processes are amplified in the vicinity of the cut-off layer by the amplification of the incident field and they remove only a negligible amount of energy from the incident wave along its way to the cut-off layer. Therefore, only the back-scattering of the cut-off vicinity is collected and the good spatial resolution of reflectometry is conserved [Vermare et al., 2011]. As illustrated in Figure 5.2, the back-scattered wave is selected following the Bragg relation: $2k_i = -k_f$ where k_i is the local wave-number of the probing wave and k_f is the wave-number of the fluctuations. By varying the angle of the incident wave the selected wave number is changed and a spectrum in wave-number of the fluctuations can be constructed [see Conway et al., 2004, for a complete review on DR]. The wave number spectrum of QuaLiKiz saturated potential was constructed based on this kind of measurements [Casati et al., 2009] as discussed in § 4.2.3.

Information on the fluctuation velocity lies in the frequency spectrum of the back-scattered signal. The incident wave frequency spectrum is indeed broadened by the fluctuations and shifted by Doppler effect: $\Delta\omega = \mathbf{k}_f \cdot \mathbf{v}_f$ where $\mathbf{v}_f$ is the group velocity of the fluctuations. Measuring the Doppler shift gives access to the group velocity of the fluctuations. As detailed in Chapter 2, the fluctuations velocity essentially corresponds to the $\mathbf{E} \times \mathbf{B}$ velocity. Hence, Doppler reflectometry gives a measure of the radial electric field.

The accessible size of fluctuations ranges from $k_\perp \sim 2$ cm^{-1} to 10 cm^{-1}, in the range of TEM turbulence. Radii from $r/a \approx 0.5$ to the edge can be probed with this technique. Thus, a combination with CXRS data is possible to access the poloidal velocity via the

radial force balance equation as performed in Fenzi et al. [2011, Figure 8]. As previously mentioned, a comparison between the radial electric field calculated from DR measurements was recently compared to the radial electric field from CXRS measurements in the plasma edge of ASDEX Upgrade giving a convincing validation on both techniques [Viezzer et al., 2013, Figure 5].

5.1.2 A few words about experimental and numerical analysis of angular momentum transport

Thanks to the progress of computing technology and the improvement of diagnostic techniques over the past decade, simulations and experimental values of the momentum can be obtain both with sufficient precision such that quantitative comparisons are possible. Interestingly, they have changed the understanding of the momentum transport in tokamak plasmas.

A link between momentum and heat transport has been clearly established experimentally on various machines [Suckewer et al., 1981, Burrell et al., 1988, Weisen et al., 1989, Scott et al., 1990, Kallenbach et al., 1991, Nagashima et al., 1994, de Vries et al., 2008] and explained theoretically [Mattor and Diamond, 1988]. Nevertheless, the experimental values of the effective Prandtl number $Pr_{\text{eff}} = \chi_{\varphi,\text{eff}}/\chi_{i,\text{eff}} = \Pi_\varphi \nabla T_i / Q_i \nabla u_\parallel$ have been reported ranging from 0.1 to 0.4 in the gradient region [de Vries et al., 2006], significantly below $Pr = \chi_\varphi/\chi_i = 1$ estimated in early theoretical works [Mattor and Diamond, 1988]. The discrepancy between the effective Prandtl number and the theoretical one is a strong indication of the existence of an additional inward mechanism for the momentum transport. An inward convective component *i.e.* a pinch of the angular momentum transport of significant value was first evidenced experimentally by shifting the NBI torque from on-axis to off-axis in JT-60U[Nagashima et al., 1994]. Thanks to the development of gyro-kinetic simulations (see § 4.1), it is now well determined numerically [Peeters et al., 2007, 2011]. Dedicated torque modulation experiments [Tala et al., 2007, Yoshida et al., 2007, Solomon et al., 2009] and time evolution studies of the rotation profile after applying magnetic perturbations [Kaye et al., 2009] enabled for an experimental characterisation of the momentum pinch. In particular, its strong dependence with the density peaking predicted by theory [Peeters et al., 2011] is confirmed [Kaye et al., 2009, de Vries et al., 2010, Tala et al., 2011, Weisen et al., 2012], as its weak dependence with collisionality (see Kluy et al. [2009] for simulations and Solomon et al. [2010], Tala et al. [2011] for experimental results).

However, contrary to particle transport, the picture of momentum transport is not complete with only diffusive and convective components. Indeed, tokamak plasmas can spin up without any significant external injection of angular momentum [Lee et al., 2003, Rice et al., 2004, 2007]. Dedicated experiments [Solomon et al., 2007] shows that a finite torque is needed to maintain zero rotation in a tokamak plasma proving de facto the existence of the so-called *residual stress*. The explanation for the existence of the residual stress reflects

the fact that angular momentum conservation is only guaranteed in an axisymmetric system contrary to particle or energy conservation. Therefore, any breaking of the toroidal symmetry will generate a momentum flux [Peeters and Angioni, 2005, Hahm et al., 2007, Diamond et al., 2008]. Among the non-diffusive, non-convective sources of momentum transport, the $\mathbf{E} \times \mathbf{B}$ velocity shearing is a strong parallel symmetry breaker as illustrated in Chapter 2 which is not necessary linked to the parallel velocity as illustrated by the radial force balance equation:

$$E_r = v_\varphi B_\theta - v_\theta B_\varphi + \frac{\nabla p_i}{e_i n_i} \tag{5.1}$$

Its contribution to the residual stress has been quantified numerically [Gürcan et al., 2007, Casson et al., 2009] and experimentally [Yan et al., 2010] despite the difficulty to measure a radial electric field *shear*.

Other symmetry breakers which are not included in this work contribute to the residual stress. The up-down asymmetry of the equilibrium generates also a net angular momentum as demonstrated by Camenen et al. [2010] by breaking the parallel symmetry. Going to higher order in ρ^*, the profile shearing effect in global simulations is also an angular momentum source [Gürcan et al., 2010a], due to the induced tilt in the ballooning angles of the eddies as illustrated in Camenen et al. [2011].

The toroidal field ripple breaks the toroidal invariance of tokamak geometry. Therefore, angular momentum is exchanged between the coils and the plasma [see Abiteboul, 2012, Chapter 6] creating an opposite torque on the fixed coils than the one in the plasma such that the total angular momentum is conserved. It was illustrated byde Vries et al. [2010], Fenzi et al. [2011] experimentally where a scan in toroidal field ripple was performed and resulted in the modification of the toroidal momentum up to the centre of the plasma.

The interaction of the plasma with the boundaries is also a significant source of angular momentum as illustrated by the variation of the boundary conditions in a reduced model Gürcan et al. [2010b] and confirmed by non-linear gyro-kinetic simulations [Abiteboul et al., 2013] and turbulence and rotation measurements [LaBombard et al., 2004, Hennequin et al., 2010]. Moreover, thermal orbit loss are also a momentum source worth mentioning [de-Grassie, 2009]. Finally, the poloidal asymmetry of the turbulence intensity in tokamaks creates a poloidal asymmetric flow in the scrape of layer [Bufferand et al., 2011]. The scrape of layer back-reaction on the plasma core can be seen as an asymmetric boundary condition. Due to the complexity and numerical cost of an accurate and consistent description of core, edge and scrape of layer dynamics, such a mechanism remains yet to be modelled.

Therefore, there are numerous mechanisms responsible for a torque in addition to the tangential NBI, which could explain the current discrepancy between simulations and experiments in the evaluation of the momentum diffusivity and pinch.

5.2 Experiments analysis with QuaLiKiz

5.2.1 NBI modulation experiments in JET

The NBI modulation experiment that demonstrated the existence of an angular momentum pinch in JET [Tala et al., 2007] is analysed. In this JET shot, the amplitude of the NBI was modulated to produce a modulated plasma rotation. Two quantities can be measured: the amplitude and the phase of the modulated toroidal velocity. The phase and amplitude are modelled assuming various combinations of χ_φ and V_{pinch} and zero residual stress using JETTO [Cenacchi and Taroni, 1988]:

- either with only momentum diffusivity *i.e.* $\chi_\varphi/\chi_i = \chi_{\varphi,eff}/\chi_i \approx 0.25$
- or with both momentum diffusivity and pinch. χ_φ/χ_i is chosen to be equal to unity [Tala et al., 2007] as in early theoretical works [Mattor and Diamond, 1988] or is adapted to match the predicted gyro-kinetic values [Tala et al., 2009]. In the later case, a pinch velocity of 15 m/s is found by matching the experimental effective diffusivity $\chi_{\varphi,eff}$ or, equivalently, the modulated toroidal velocity amplitude.

As illustrated in Tala et al. [2007] and Tala et al. [2009], both the amplitude and the phase of the experimental toroidal velocity are only correctly reproduced when a momentum pinch is taken into account, the disagreement in the case of a diffusive momentum being clearer on the phase signal. The residual stress was neglected in Tala et al. [2007, 2009] analysis since it was considered that the amplitude of the velocity modulation is small enough not to change the temperature and density profiles or the turbulent state.

Quasi-linear gyro-kinetic simulations are performed with QuaLiKiz. The global parameters are the ones used in GKW for the determination of χ_φ presented in Tala et al. [2009, Figure 3]. The main input parameters of the simulation are displayed in Figure 5.3. All parameters are taken from JETTO interpretative run performed for GKW simulation of [Tala et al., 2009] with the exception of $T_i = T_e$ as there is no evidence from the CX and ECE signals for $T_i \neq T_e$. Since QuaLiKiz has an $\hat{s} - \alpha$ equilibrium, the gradients are averaged over the flux surface.

The $\mathbf{E} \times \mathbf{B}$ shear calculated with the radial force balance equation on the carbon impurity is significant in this shot, as indicated in Figure 5.3. The *2-point method* presented in the former chapter is adapted to take the effect of the residual stress into account in the estimation of the momentum diffusivity and pinch. Three simulations are performed enabling to estimate the residual stress as well. The first one corresponds to the experimental conditions described in Figure 5.3. The second one is performed with the parallel velocity modified by $\pm 20\%$. Both the parallel velocity gradient and the $\mathbf{E}\times\mathbf{B}$ shearing are affected by this modification of the parallel velocity. The last simulation is performed with the parallel velocity *incremented* by $\pm 0.05 v_{Ti}$. The parallel velocity gradient is not perturbed by this modification. Considering that such modifications have a *linear* effect on the momentum

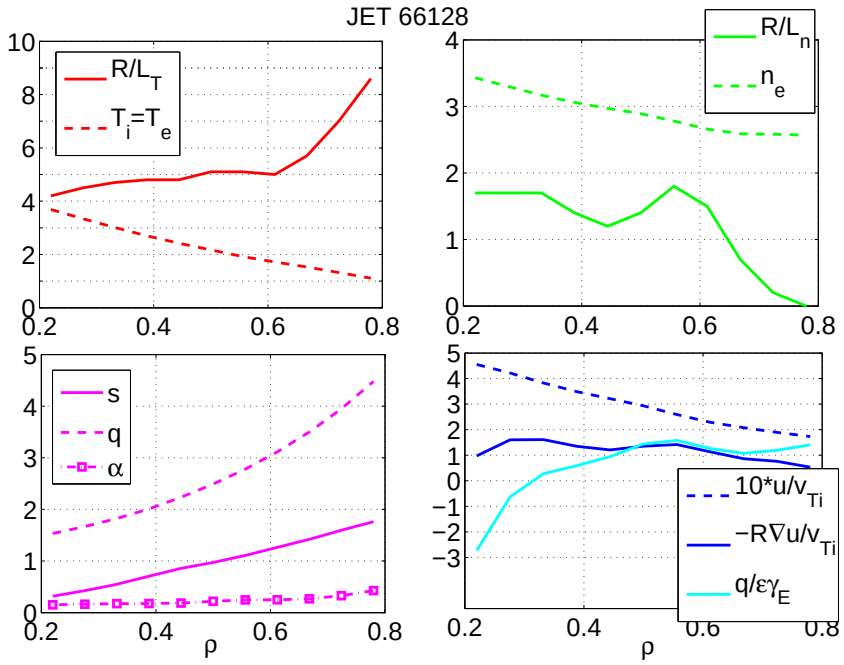

Figure 5.3: Input parameters for QuaLiKiz simulation of JET shot 66128. All parameters were taken from JETTO fit realized for GKW simulations of [Tala et al., 2009] except $T_i = T_e$. $Z_{eff} = 2$

flux, a linear regression is possible to estimate the momentum diffusivity $\chi_\parallel$, the pinch $V_\parallel$ and the residual stress Π_{RS}. If Π_1 is the normalised parallel momentum flux from the 1$^{\text{st}}$ simulation, Π_2 from the 2$^{\text{nd}}$ and Π_3 from the 3$^{\text{rd}}$, they read, under a linear modification by the changes presented above:

$$\Pi_1 = -\chi_\parallel \nabla u_\parallel + V_\parallel u_\parallel + \Pi_{RS} / \sum_s m_s n_s R \tag{5.2a}$$

$$\Pi_2 = -1.2\chi_\parallel \nabla u_\parallel + 1.2 V_\parallel u_\parallel + \Pi_{RS} / \sum_s m_s n_s R \tag{5.2b}$$

$$\Pi_3 = -\chi_\parallel \nabla u_\parallel + V_\parallel (u_\parallel + 0.05 v_{Ti}) + \Pi_{RS} / \sum_s m_s n_s R \tag{5.2c}$$

The system (5.2) is a set a 3 independent equations of 3 variables. Therefore each of the variables $\chi_\parallel$, $V_\parallel$ and Π_{RS} are uniquely defined. Varying $u_\parallel$ by $\pm 20\%$ and incrementing $u_\parallel$ by $\pm 0.05 v_{Ti}$ defines 3 systems. If the momentum flux dependence with respect to $u_\parallel$ and $\nabla u_\parallel$ is linear the 3 systems should give the same results. In the opposite case, the dispersion between the results (inversely) measures the validity of the bilinear regression. The method ensures that linear dependences of γ_E with $\nabla u_\parallel$ and $u_\parallel$ are removed from the residual stress and accounted for in $\chi_\parallel$ and $V_\parallel$ respectively.

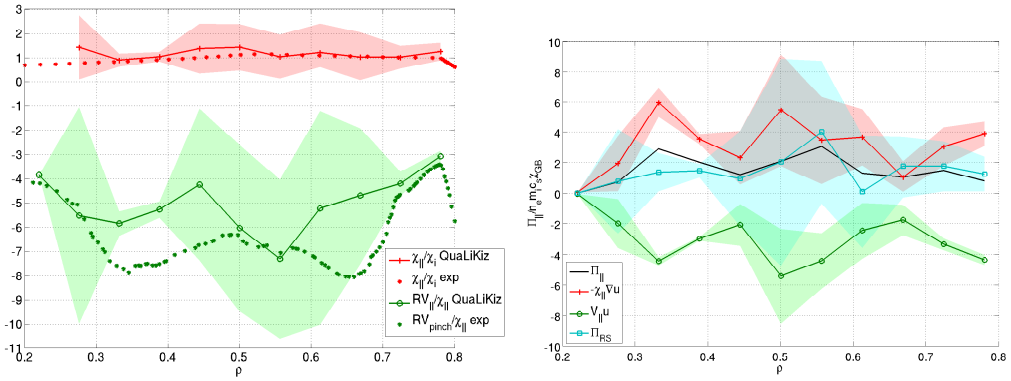

Figure 5.4: Left: Prandtl number (red crossed) and pinch number(green circles) calculated by a 3-point method. Right: Detail of the different contributions to $\Pi_{||}$.

The resulting Prandtl and pinch numbers are given in Figure 5.4(a) the coloured regions being the dispersion of the values for both quantities due to the non-linear evolution of the momentum flux with $u_\parallel$, $\nabla u_\parallel$, γ_E [see Casson et al., 2009].

The estimated Prandtl number lies within 0.8 and 1.4, close to the value determined in Tala et al. [2009]. The pinch number calculated with QuaLiKiz ranges from 3 to 7, in good agreement with the experimental values ranging from 3 to 8. The large uncertainties obtained with the 3-point method indicates that the momentum flux changes in a complex way with $u_\parallel$ and $\nabla u_\parallel$, the growth rates being modified by the modification of $u_\parallel$, $\nabla u_\parallel$ and γ_E. Thus, the linearisation employed to get Figure 5.4(a) is not entirely valid with such an amplitude for the regression in $u_\parallel$, $\nabla u_\parallel$. This amplitude is however necessary to have a acceptable signal over noise ratio since the numerical integrals used in QuaLiKiz have a finite precision.

The contributions to the momentum flux from $u_\parallel$, $\nabla u_\parallel$ and the residual stress are compared in Figure 5.4(b). The estimated residual stress seems not entirely negligible in this shot. However a definitive conclusion would require smaller error bars.

Since QuaLiKiz provides absolute values for the fluxes, and their diffusive and convective parts, they can be compared to the quantities inferred from the JETTO analysis in physical units. The pinch velocity itself $-V_\parallel$ (plain curve) is plotted along with the effective ion heat flux $\chi_{i,eff}$ (dashed curve) in Figure 5.5 and compared to the experimental estimates (right panel). To improve the robustness of the results and reproduce experimental uncertainties, R/L_T was varied by 20% with the associated modification of γ_E. It corresponds to the coloured regions of Figure 5.5. When increasing the temperature gradients by 20% $\chi_{i,eff}$, QuaLiKiz predictions are much closer to the experiment. Since the pinch and the Prandtl number are in good agreement with the experimental values, the values predicted by QuaLiKiz for $V_\parallel$ show the same agreement with experimental data than for $\chi_{i,eff}$. This advocates for including a more refined magnetic equilibrium in QuaLiKiz. Indeed, averaging

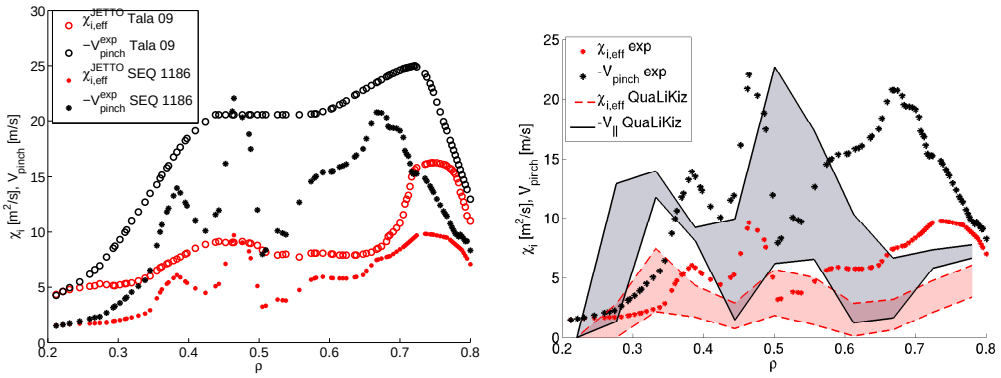

Figure 5.5: Ion heat flux diffusivity (red dashed) and angular momentum pinch velocity (plain). The coloured regions correspond to a 20% variation of R/L_T with associated variation of γ_E. Left panel experimental data from Tala et al. [2009] compared to the experimental data used in this work. Right panel experimental data compared to QuaLiKiz predictions

over the flux surface is a way to take the stabilizing effect of the elongation into account [Angelino et al., 2009]. However, it appears that the stabilization is overestimated by this method. Increasing the gradients by 20% gives values comparable to the gradients taken at the mid-plane. The over-stabilisation due the flux surface average of the gradients could be linked to the ballooned structure of the turbulence. The most unstable region, responsible for most of the radial flux, experiences indeed a much steeper gradient than averaged on a flux surface in the case of elongated plasmas such as JET ones. Around $\rho = 0.7$, the discrepancy between QuaLiKiz and JETTO predictions enlarges. This may comes from the choice of $T_e = T_i$ made in QuaLiKiz simulations based on CX and ECE signals in disagreement with JETTO fit. However, the fact that JETTO runs fail to reproduce the experimental phase of the modulated velocity at $\rho \approx 0.7$ is worth noticing.

Comparing the data published in Tala et al. [2009] with the data from the same JETTO sequence used for QuaLiKiz input (Figure 5.5, left panel) shows a significant discrepancy between both experimental fluxes. Moreover, power balance are significantly different between the both JETTO sequences without any obvious reason. This is another indication that driving the turbulent codes with the gradients is not experimentally relevant due to the combined uncertainties on the gradients deduced from experimental profiles and high stiffness of the turbulent fluxes.

To summarize, considering the experimental uncertainties on the various gradients used as inputs, QuaLiKiz estimations of the Prandtl number and the momentum pinch are close enough to the ones evaluated from the experiment. In particular, an inward convective flux of momentum is found in the model and the experiment with a pinch number ranging from 5 to 8. However, a quantitative analysis on the fluxes intensity remains difficult due to the fluxes sensitivity to the temperature gradients combined with the difficulty to measure them accurately in experiments. To overcome this issue, the present version of QuaLiKiz

has to be coupled to an integrated platform such as CRONOS. This will enable driving QuaLiKiz via the sources which is more relevant physically than to impose the gradients.

5.3 Perspectives: Implementation in CRONOS, QuaLiKiz simulations driven by sources

As indicated at the beginning of Chapter 2, the goal of QuaLiKiz is to be part of an integrated work-flow, which imposes for the code to be fast enough. To achieve this goal, QuaLiKiz needs to be further optimised to keep the global simulation time of 1s of plasma under a week on a few tens of processors [Baiocchi et al., 2013].

Nevertheless, the implementation of QuaLiKiz in an integrated code such as CRONOS enables forcing the code by physical sources rather than by the gradients. This will considerably improve the prediction capabilities of the code compared to the situation presented in this work considering the error bars associated with the gradients determined experimentally. Moreover this forcing enables a self-consistent treatment of the profiles which are evolving according to the fluxes. However, the equilibrium distribution function remains Gaussian and non-local effects cannot be modelled by this approach.

6

Conclusion

On the path to controlling nuclear fusion as a source of energy, the machines grew up in size from table experiments to ITER, the next generation fusion device, a 6 m major radius and 2 m minor radius machine, requiring a total power of 50 MW for its operation. Along with the size of the machine, increases the cost of its construction. Therefore, understanding the turbulence and discovering scenarii with optimized confinement is of prime importance to limit the size growth of future machines. To achieve this goal, predicting consistently the profiles of temperature and density and rotation is an important challenge to manage. The work presented in this manuscript is a step in this direction. The ability to predict the angular momentum turbulent transport has been added in the quasi-linear gyro-kinetic code QuaLiKiz previously developed. This represents the first step towards a coherent prediction of temperature, density and rotation in the sense that QuaLiKiz operates a reduced model of the complex non-linear self-organising plasma physics fast enough to be coupled to an integrated code.

A trade off has to be found to retain most of the physics of turbulent transport at a reduced numerical cost. A gyro-kinetic description is used in order to retain the kinetic wave-particle resonance essential in the establishment of the turbulence threshold. Due to the cost of this framework, several additional simplifications are performed. The intrinsically non-linear problem is not solved self-consistently. Instead, an extensively validated quasi-linear approach is taken, saving two orders of magnitude in CPU time. For the linear solver, a specific method enables saving other two orders of magnitude in computing time using the dimensional reduction associated with a low order ballooning approximation and analytic eigenfunctions. With these four orders of magnitude gained over non-linear gyro-kinetic simulations, a gyro-kinetic quasi-linear approach starts being doable within an integrated modelling framework.

For a coherent angular momentum transport modelling, the ability to consider rotating equilibria has been added in QuaLiKiz. Integrating rotating equilibria involved accounting for a potential sheared parallel rotation of the plasma and for $\mathbf{E} \times \mathbf{B}$ shearing. Therefore, the new system of equations is derived and presented as implemented in QuaLiKiz.

Consequently, a new analytic model for the eigenfunctions has been developed to reproduce the effect of sheared parallel rotation and $\mathbf{E} \times \mathbf{B}$ shearing on the fluctuating potential. The eigenfunction asymmetrisation resulting from the parallel symmetry breaking by both parallel rotation and $\mathbf{E} \times \mathbf{B}$ shearing is observed in this hydrodynamic model. Moreover, the eigenfunctions are shown to reproduce self-consistent gyro-kinetic calculations, at least for the dominant transport spatial scales. The evolution of the resulting linear growth rates have been compared to self-consistent gyro-kinetic calculations as well. They exhibit a good agreement with respect to more complete linear gyro-kinetic calculations in a large range of parameters within the experimental domain.

The derivation of the quasi-linear turbulent flux of angular momentum is presented along with the modifications of the saturated potential induced by the presence of a sheared rotation. Accounting for the modifications of the eigenfunctions in the mixing-length framework is shown to access to the $\mathbf{E} \times \mathbf{B}$ stabilizing effect and to its impact on the shift towards smaller spatial scales. The sensitivity of the momentum to the parallel rotation and its gradient is studied and successfully compared to published non-linear gyro-kinetic simulations. The effect of $\mathbf{E} \times \mathbf{B}$ shearing on the heat, particle and angular momentum fluxes is specifically studied due to its beneficial effect on the confinement properties in tokamak plasmas. QuaLiKiz predictions are shown to be in good agreement with non-linear gyro-kinetic simulations for the heat and particle transport. For the angular momentum transport, the flux amplitude is overestimated by a factor 2 at large values of $\mathbf{E} \times \mathbf{B}$ shearing due to the overestimation by the analytic model of the eigenfunction asymmetrisation.

Finally, an NBI modulation experiment performed at JET is simulated to illustrate QuaLiKiz abilities for experimental analysis and prediction. The momentum flux dependence on the parallel rotation and its gradient, *i.e.* the momentum diffusivity and the momentum pinch, show good agreement with experimental values. The comparison also brings to light the sensitivity of the predicted fluxes to the gradients used as an input and the limitations of using an $\hat{s} - \alpha$ equilibrium to simulate shaped plasmas. The first issue will however be solved by coupling QuaLiKiz to an integrated code such as CRONOS. Within CRONOS framework, QuaLiKiz will be driven by the fluxes, enabling for the self-adjustment of the profiles.

*
* *

On the path to predicting consistently the temperature, density and angular momentum profiles, a number of challenges remain to be solved. Indeed, however fast QuaLiKiz should be for a gyro-kinetic code, some additional optimisation is needed to bring down the

required time for a 1 s plasma integrated simulation which is one week on a few tens of processors for now. After coupling this new version to CRONOS, the ability of QuaLiKiz to predict the plasma confinement properties should be assessed, especially in the case of strong rotation and strong $\mathbf{E} \times \mathbf{B}$ shearing. Additionally, implementing a shaped analytic equilibrium such as Miller's would improve QuaLiKiz predictions for the various shaped plasma tokamaks (JET, ASDEX Upgrade, DIII-D, etc). A longer term and more theoretical objective would be to build a physical alternative to the parameter used to adapt QuaLiKiz saturation rule at low magnetic shear. Replacing the fixed parameter setting the saturated potential amplitude for the GA-std case by a physical model appears to be a challenging objective.

Bibliography

J. Abiteboul. *Transport turbulent et néoclassique de quantité de mouvement toroïdale dans les plasmas de tokamak*. PhD thesis, Aix-Marseille Université, 2012.

J. Abiteboul, Ph. Ghendrih, V. Grandgirard, T. Cartier-Michaud, G. Dif-Pradalier, X. Garbet, G. Latu, C. Passeron, Y. Sarazin, A. Strugarek, O. Thomine, and D. Zarzoso. Turbulent momentum transport in core tokamak plasmas and penetration of scrape-off layer flows. *Plasma Physics and Controlled Fusion*, 55(7):074001, 2013. URL http://stacks.iop.org/0741-3335/55/i=7/a=074001.

J. Abiteboul, X. Garbet, V. Grandgirard, S. J. Allfrey, Ph. Ghendrih, G. Latu, Y. Sarazin, and A. Strugarek. Conservation equations and calculation of mean flows in gyrokinetics. *Physics of Plasmas*, 18(8), AUG 2011. ISSN 1070-664X. doi: {10.1063/1.3620407}.

Moinuddin Ahmed, Kevin J. Anchukaitis, Asfawossen Asrat, Hemant P. Borgaonkar, Martina Braida, Brendan M. Buckley, Ulf Buntgen, Brian M. Chase, Duncan A. Christie, Edward R. Cook, Mark A. J. Curran, Henry F. Diaz, Jan Esper, Ze-Xin Fan, Narayan P. Gaire, Quansheng Ge, Joelle Gergis, J. Fidel Gonzalez-Rouco, Hugues Goosse, Stefan W. Grab, Nicholas Graham, Rochelle Graham, Martin Grosjean, Sami T. Hanhijarvi, Darrell S. Kaufman, Thorsten Kiefer, Katsuhiko Kimura, Atte A. Korhola, Paul J. Krusic, Antonio Lara, Anne-Marie Lezine, Fredrik C. Ljungqvist, Andrew M. Lorrey, Jurg Luterbacher, Valerie Masson-Delmotte, Danny McCarroll, Joseph R. McConnell, Nicholas P. McKay, Mariano S. Morales, Andrew D. Moy, Robert Mulvaney, Ignacio A. Mundo, Takeshi Nakatsuka, David J. Nash, Raphael Neukom, Sharon E. Nicholson, Hans Oerter, Jonathan G. Palmer, Steven J. Phipps, Maria R. Prieto, Andres Rivera, Masaki Sano, Mirko Severi, Timothy M. Shanahan, Xuemei Shao, Feng Shi, Michael Sigl, Jason E. Smerdon, Olga N. Solomina, Eric J. Steig, Barbara Stenni, Meloth Thamban, Valerie Trouet, Chris S. M. Turney, Mohammed Umer, Tas van Ommen, Dirk Verschuren, Andre E. Viau, Ricardo Villalba, Bo M. Vinther, Lucien von Gunten, Sebastian Wagner,

Eugene R. Wahl, Heinz Wanner, Johannes P. Werner, James W. C. White, Koh Yasue, Eduardo Zorita, and PAGES 2k Consortium. Continental-scale temperature variability during the past two millennia. *Nature Geoscience*, 6(5):339–346, MAY 2013. ISSN 1752-0894. doi: {10.1038/NGEO1797}.

P. Angelino, X. Garbet, L. Villard, A. Bottino, S. Jolliet, Ph. Ghendrih, V. Grandgirard, B. F. McMillan, Y. Sarazin, G. Dif-Pradalier, and T. M. Tran. Role of plasma elongation on turbulent transport in magnetically confined plasmas. *Physical Review Letters*, 102: 195002, May 2009. doi: 10.1103/PhysRevLett.102.195002. URL http://link.aps.org/doi/10.1103/PhysRevLett.102.195002.

C. Angioni. *Theoretical and Experimental Research on Particle and Impuity Transport in the Core of Tokamak Plasmas*. Habilitation à diriger des recherches, Max-Planck Institut für Plasma Physik, 2010.

C. Angioni, R. M. McDermott, E. Fable, R. Fischer, T. Puetterich, F. Ryter, G. Tardini, and ASDEX Upgrade Team. Gyrokinetic modelling of electron and boron density profiles of H-mode plasmas in ASDEX Upgrade. *Nuclear Fusion*, 51(2), FEB 2011. ISSN 0029-5515. doi: {10.1088/0029-5515/51/2/023006}.

C. Angioni, Y. Camenen, F. J. Casson, E. Fable, R. M. McDermott, A. G. Peeters, and J. E. Rice. Off-diagonal particle and toroidal momentum transport: a survey of experimental, theoretical and modelling aspects. *Nuclear Fusion*, 52(11, SI), NOV 2012. ISSN 0029-5515. doi: {10.1088/0029-5515/52/11/114003}. 13th International Workshop on H-Mode Physics and Transport Barriers, Lady Margaret Hall Coll, Oxford, ENGLAND, OCT, 2011.

V.I. Arnold. A proof of A.N. Kolmogorov's theorem on the conservation of conditional-periodic motions in a small change of the Hamiltonian function. *Uspekhi Matematicheskikh Nauk*, 18(5):13–40, 1963.

B. Baiocchi, J. Garcia, M. Beurkens, C. Bourdelle, F. Crisanti, C. Giroud, J. Hobirk, F. Imbeaux, I. Nunes, EU-ITM ITER Scenario Modelling group, and JET EFDA contributors. Turbulent transport analysis of JET H-mode and hybrid plasmas using QuaLiKiz, TGLF and GLF23. In *40th EPS Conference on Plasma Physics*, volume 37D, page P2.165. European Physical Society, JUL 2013.

M. Barnes, F. I. Parra, E. G. Highcock, A. A. Schekochihin, S. C. Cowley, and C. M. Roach. Turbulent transport in tokamak plasmas with rotational shear. *Physical Review Letters*, 106:175004, Apr 2011. doi: 10.1103/PhysRevLett.106.175004. URL http://link.aps.org/doi/10.1103/PhysRevLett.106.175004.

M. A. Beer. *Gyrofluid models of turbulent transport in tokamaks*. PhD thesis, Princeton University, 1995.

Nicolas Besse, Yves Elskens, D. F. Escande, and Pierre Bertrand. Validity of quasilinear theory: refutations and new numerical confirmation. *Plasma Physics and Controlled Fusion*, 53(2), FEB 2011. ISSN 0741-3335. doi: {10.1088/0741-3335/53/2/025012}.

H. Biglari, P.H. Diamond, and P.W. Terry. Influence of sheared poloidal rotation on edge turbulence. *Physics of Fluids B-Plasma Physics*, 2(1):1–4, Jan 1990. ISSN 0899-8221. doi: 10.1063/1.859529.

A. Bortolon, Y. Camenen, A.N. Karpushov, B.P. Duval, Y. Andrebe, L. Federspiel, O. Sauter, and the TCV Team. Indirect measurement of poloidal rotation using inboard-âĂŞoutboard asymmetry of toroidal rotation and comparison with neoclassical predictions. *Nuclear Fusion*, 53(2):023002, 2013. URL http://stacks.iop.org/0029-5515/53/i=2/a=023002.

C. Bourdelle, X. Garbet, G.T. Hoang, J. Ongena, and R.V. Budny. Stability analysis of improved confinement discharges: internal transport barriers in tore supra and radiative improved mode in textor. *Nuclear Fusion*, 42(7):892–902, Jul 2002. ISSN 0029-5515. doi: 10.1088/0029-5515/42/7/312.

C. Bourdelle, X. Garbet, F. Imbeaux, A. Casati, N. Dubuit, R. Guirlet, and T. Parisot. A new gyrokinetic quasilinear transport model applied to particle transport in tokamak plasmas. *Physics of Plasmas*, 14(11), Nov 2007. ISSN 1070-664X. doi: 10.1063/1.2800869.

p.l.c. BP. Bp statistical review of world energy june 2013. Technical report, BP p.l.c., June 2013a.

p.l.c. BP. Bp energy outlook 2030. Technical report, BP p.l.c., January 2013b.

A. J. Brizard and T. S. Hahm. Foundations of nonlinear gyrokinetic theory. *Reviews of Modern Physics*, 79(2):421–468, Apr-Jun 2007. ISSN 0034-6861. doi: 10.1103/RevModPhys.79.421.

James H. Brown, William R. Burnside, Ana D. Davidson, John P. DeLong, William C. Dunn, Marcus J. Hamilton, Norman Mercado-Silva, Jeffrey C. Nekola, Jordan G. Okie, William H. Woodruff, and Wenyun Zuo. Energetic Limits to Economic Growth. *Bioscience*, 61(1):19–26, JAN 2011. ISSN 0006-3568. doi: {10.1525/bio.2011.61.1.7}.

S. Brunner, M. Fivaz, T.M. Tran, and J. Vaclavik. Global approach to the spectral problem of microinstabilities in tokamak plasmas using a gyrokinetic model. *Physics of Plasmas*, 5(11):3929–3949, NOV 1998. ISSN 1070-664X. doi: {10.1063/1.873113}.

H. Bufferand, G. Ciraolo, L. Isoardi, G. Chiavassa, F. Schwander, E. Serre, N. Fedorczak, Ph. Ghendrih, and P. Tamain. Applications of SOLEDGE-2D code to complex SOL configurations and analysis of Mach probe measurements. *Journal of Nuclear Materials*, 415(1, S):S589–S592, AUG 1 2011. ISSN 0022-3115. doi: {10.1016/j.jnucmat.2010.11.037}. 19th International Conference on Plasma-Surface Interactions in Controlled Fusion Devices (PSI), Univ Calif, Gen Atom, San Diego, CA, MAY 24-28, 2010.

K.H. Burrell, R.J. Groebner, H. St. John, and R.P. Seraydarian. Confinement of angular momentum in divertor and limiter discharges in the doublet iii tokamak. *Nuclear Fusion*, 28(1):3, 1988. URL http://stacks.iop.org/0029-5515/28/i=1/a=001.

Y. Camenen, A. Bortolon, B. P. Duval, L. Federspiel, A. G. Peeters, F. J. Casson, W. A. Hornsby, A. N. Karpushov, F. Piras, O. Sauter, A. P. Snodin, and G. Szepesi. Experimental evidence of momentum transport induced by an up-down asymmetric magnetic equilibrium in toroidal plasmas. *Physical Review Letters*, 105:135003, Sep 2010. doi: 10.1103/PhysRevLett.105.135003. URL http://link.aps.org/doi/10.1103/PhysRevLett.105.135003.

Y. Camenen, A. G. Peeters, C. Angioni, F. J. Casson, W. A. Hornsby, A. P. Snodin, and D. Strintzi. Impact of the background toroidal rotation on particle and heat turbulent transport in tokamak plasmas. *Physics of Plasmas*, 16(1), JAN 2009a. ISSN 1070-664X. doi: {10.1063/1.3057356}.

Y. Camenen, A. G. Peeters, C. Angioni, F. J. Casson, W. A. Hornsby, A. P. Snodin, and D. Strintzi. Intrinsic rotation driven by the electrostatic turbulence in up-down asymmetric toroidal plasmas. *Physics of Plasmas*, 16(6), JUN 2009b. ISSN 1070-664X. doi: {10.1063/1.3138747}.

Y. Camenen, Y. Idomura, S. Jolliet, and A. G. Peeters. Consequences of profile shearing on toroidal momentum transport. *Nuclear Fusion*, 51(7), JUL 2011. ISSN 0029-5515. doi: {10.1088/0029-5515/51/7/073039}.

J. Candy, R.E. Waltz, and M.N. Rosenbluth. Smoothness of turbulent transport across a minimum-q surface. *Physics of Plasmas*, 11(5):1879–1890, MAY 2004. ISSN 1070-664X. doi: {10.1063/1.1689967}.

A. Casati. *A quasi-linear gyrokinetic transport model for tokamak plasmas*. PhD thesis, Université de Provence – Aix-Marseille 1, 2010.

A. Casati, T. Gerbaud, P. Hennequin, C. Bourdelle, J. Candy, F. Clairet, X. Garbet, V. Grandgirard, Ö. D. Gürcan, S. Heuraux, G. T. Hoang, C. Honoré, F. Imbeaux, R. Sabot, Y. Sarazin, L. Vermare, and R. E. Waltz. Turbulence in the tore supra tokamak: Measurements and validation of nonlinear simulations. *Phys. Rev. Lett.*, 102:165005, Apr 2009. doi: 10.1103/PhysRevLett.102.165005. URL http://link.aps.org/doi/10.1103/PhysRevLett.102.165005.

A. Casati, C. Bourdelle, X. Garbet, F. Imbeaux, J. Candy, F. Clairet, G. Dif-Pradalier, G. Falchetto, T. Gerbaud, V. Grandgirard, Oe. D. Guercan, P. Hennequin, J. Kinsey, M. Ottaviani, R. Sabot, Y. Sarazin, L. Vermare, and R. E. Waltz. Validating a quasi-linear transport model versus nonlinear simulations. *Nuclear Fusion*, 49(8), AUG 2009. ISSN 0029-5515. doi: {10.1088/0029-5515/49/8/085012}.

F. J. Casson, A. G. Peeters, Y. Camenen, W. A. Hornsby, A. P. Snodin, D. Strintzi, and G. Szepesi. Anomalous parallel momentum transport due to e x b flow shear in a tokamak plasma. *Physics Of Plasmas*, 16(9), Sep 2009. ISSN 1070-664X. doi: 10.1063/1.3227650.

F. J. Casson, A. G. Peeters, C. Angioni, Y. Camenen, W. A. Hornsby, A. P. Snodin, and G. Szepesi. Gyrokinetic simulations including the centrifugal force in a rotating tokamak plasma. *Physics of Plasmas*, 17(10), Oct 2010. ISSN 1070-664X. doi: 10.1063/1.3491110.

F. J. Casson, A. G. Peeters, C. Angioni, Y. Camenen, W. A. Hornsby, A. P. Snodin, and G. Szepesi. Gyrokinetic simulations including the centrifugal force in a rotating tokamak plasma (vol 17, 102305, 2010). *Physics of Plasmas*, 19(9), SEP 2012. ISSN 1070-664X. doi: {10.1063/1.4757116}.

P.J. Catto, M.N. Rosenbluth, and C.S. Liu. Parallel velocity shear instabilities in an inhomogeneous plasma with a sheared magnetic field. *Physics of Fluids*, 16(10):1719–1729, 1973. ISSN 1070-6631. doi: {10.1063/1.1694200}.

C. Cenacchi and G. Taroni. JETTO: A free boundary plasma transport code. Technical report, JET EFDA, 1988.

B.V. Chirikov. A universal instability of many-dimensional oscillator systems. *Physics Reports*, 52:265–379, MAY 1979. ISSN 0370-1573.

J. Citrin. *Turbulent transport in tokamak advanced scenarios.* PhD thesis, Technische Universiteit Eindhoven, 2012.

J. Citrin, C. Bourdelle, P. Cottier, D. F. Escande, Oe D. Guercan, D. R. Hatch, G. M. D. Hogeweij, F. Jenko, and M. J. Pueschel. Quasilinear transport modelling at low magnetic shear. *Physics of Plasmas*, 19(6), Jun 2012. ISSN 1070-664X. doi: 10.1063/1.4719697.

J. Citrin, F. Jenko, P. Mantica, D. Told, C. Bourdelle, J. Garcia, J.W. Haverkort, G.M.D. Hogeweij, T. Johnson, M.J. Pueschel, and JET-EFDA contributors. Nonlinear stabilization of tokamak microturbulence by fast ions. *Physical Review Letters*, submitted, 2013.

J. W. Connor. Magnetic geometry, plasma profiles, and stability. *Plasma Physics Reports*, 32(7):539–548, JUL 2006. ISSN 1063-780X. doi: {10.1134/S1063780X06070026}.

J.W. Connor, R.J. Hastie, and J.B. Taylor. Shear, periodicity, and plasma ballooning modes. *Physical Review Letters*, 40(6):396–399, 1978. ISSN 0031-9007. doi: 10.1103/PhysRevLett.40.396.

G. D. Conway. Microwave reflectometry for fusion plasma diagnosis. *Nuclear Fusion*, 46(9): S665–S669, SEP 2006. ISSN 0029-5515. doi: {10.1088/0029-5515/46/9/S01}.

G.D. Conway, J. Schirmer, S. Klenge, W. Suttrop, E. Hozhauer, and ASDEX Upgrade Team. Plasma rotation profile measurements using Doppler reflectometry. *Plasma Physics and Controlled Fusion*, 46(6):951–970, JUN 2004. ISSN 0741-3335. doi: {10.1088/0741-3335/46/6/003}.

W.A. Cooper. Ballooning instabilities in tokamaks with sheared toroidal flows. *Plasma Physics and Controlled Fusion*, 30(13):1805–1812, DEC 1988. ISSN 0741-3335. doi: {10.1088/0741-3335/30/13/001}.

Nicola D'Angelo. Kelvin–Helmholtz Instability in a Fully Ionized Plasma in a Magnetic Field. *Physics of Fluids*, 8(9):1748–1750, 1965. doi: 10.1063/1.1761496. URL http://link.aip.org/link/?PFL/8/1748/1.

T. Dannert and F. Jenko. Gyrokinetic simulation of collisionless trapped-electron mode turbulence. *Physics of Plasmas*, 12(7), JUL 2005. ISSN 1070-664X. doi: {10.1063/1.1947447}.

P. C. de Vries, M. D. Hua, D. C. McDonald, C. Giroud, M. Janvier, M. F. Johnson, T. Tala, K. D. Zastrow, and JET Efda Contributors. Scaling of rotation and momentum confinement in JET plasmas. *Nuclear Fusion*, 48(6), Jun 2008. ISSN 0029-5515. doi: 10.1088/0029-5515/48/6/065006.

P. C. de Vries, T. W. Versloot, A. Salmi, M.-D. Hua, D. H. Howell, C. Giroud, V. Parail, G. Saibene, T. Tala, and JET EFDA Contributors. Momentum transport studies in jet h-mode discharges with an enhanced toroidal field ripple. *Plasma Physics and Controlled Fusion*, 52(6):065004, 2010. URL http://stacks.iop.org/0741-3335/52/i=6/a=065004.

P. C. de Vries, K. M. Rantamaki, C. Giroud, E. Asp, G. Corrigan, A. Eriksson, M. de Greef, I. Jenkins, H. C. M. Knoops, P. Mantica, H. Nordman, P. Strand, T. Tala, J. Weiland, K.-D. Zastrow, and JET EFDA Contributors. Plasma rotation and momentum transport studies at JET. *Plasma Physics and Controlled Fusion*, 48(12):1693–1708, DEC 2006. ISSN 0741-3335. doi: {10.1088/0741-3335/48/12/001}.

J.S. deGrassie. Tokamak rotation sources, transport and sinks. *Plasma Physics and Controlled Fusion*, 51(12):124047, 2009. URL http://stacks.iop.org/0741-3335/51/i=12/a=124047.

R.L. Dewar and A.H. Glasser. Ballooning mode spectrum in general toroidal systems. *Physics of Fluids*, 26(10):3038–3052, 1983. ISSN 1070-6631. doi: 10.1063/1.864028.

P. H. Diamond, C. J. McDevitt, Ö. D. Gürcan, T. S. Hahm, and V. Naulin. Transport of parallel momentum by collisionless drift wave turbulence. *Physics of Plasmas*, 15 (1):012303, 2008. doi: 10.1063/1.2826436. URL http://link.aip.org/link/?PHP/15/012303/1.

G. Dif-Pradalier. Spatial Propagation of Turbulence and Formation of Mesoscopic Structures in Plasma Turbulence. In *U.S.-E.U. Joint Transport Task Force Workshop*, April 2013.

J.Q. Dong and W. Horton. Kinetic quasitoroidal ion temperature-gradient instability in the presence of sheared flows. *Physics of Fluids B-Plasma Physics*, 5(5):1581–1592, May 1993. ISSN 0899-8221. doi: 10.1063/1.860898.

W. E. Drummond and D. Pines. Non-linear stability of plasma oscillations. *Nuclear Fusion*, (3):1049–1057, 1962. ISSN 0029-5515.

T.H. Dupree. A pertubation theory for strong plasma turbulence. *PHYSICS OF FLUIDS*, 9(9):1773–&, 1966. ISSN 1070-6631. doi: {10.1063/1.1761932}.

T.H. Dupree. Nonlinear theory of low-frequency instabilities. *Physics of Fluids*, 11(12): 2680–&, 1968. ISSN 1070-6631. doi: {10.1063/1.1691875}.

D. F. Escande and Y. Elskens. Proof of quasilinear equations in the strongly nonlinear regime of the weak warm beam instability. *Physics of Plasmas*, 10(5, 2):1588–1594, MAY 2003. ISSN 1070-664X. doi: {10.1063/1.1556604}. 44th Annual Meeting of the Division of Plasma of the American-Physical-Society, ORLANDO, FLORIDA, NOV 11-15, 2002.

C. Fenzi, X. Garbet, E. Trier, P. Hennequin, C. Bourdelle, T. Aniel, G. Colledani, P. Devynck, C. Gil, Oe. Guercan, L. Manenc, M. Schneider, J. L. Segui, and Tore Supra Team. On plasma rotation with toroidal magnetic field ripple and no external momentum input. *Nuclear Fusion*, 51(10), OCT 2011. ISSN 0029-5515. doi: {10.1088/0029-5515/51/10/103038}.

T. Fujita, Y. Kamada, S. Ishida, Y. Neyatani, T. Oikawa, S. Ide, S. Takeji, Y. Koide, A. Isayama, T. Fukuda, T. Hatae, Y. Ishii, T. Ozeki, H. Shirai, and JT-60 Team. High performance experiments in jt-60u reversed shear discharges. *Nuclear Fusion*, 39(11Y): 1627, 1999. URL http://stacks.iop.org/0029-5515/39/i=11Y/a=302.

X. Garbet, L. Laurent, F. Mourgues, J.P. Roubin, and A. Samain. Variational calculation of electromagnetic instabilities in tokamaks. *Journal Of Computational Physics*, 87(2): 249–269, Apr 1990. ISSN 0021-9991. doi: 10.1016/0021-9991(90)90253-W.

X. Garbet, Y. Sarazin, P. Ghendrih, S. Benkadda, P. Beyer, C. Figarella, and I. Voitsekhovitch. Turbulence simulations of transport barriers with toroidal velocity. *Physics of Plasmas*, 9(9):3893–3905, Sep 2002. ISSN 1070-664X. doi: 10.1063/1.1499494.

X. Garbet, Y. Idomura, L. Villard, and T. H. Watanabe. Gyrokinetic simulations of turbulent transport. *Nuclear Fusion*, 50(4), APR 2010. ISSN 0029-5515. doi: {10.1088/0029-5515/50/4/043002}.

Siegfried H. Glenzer, Brian K. Spears, M. John Edwards, Ethan T. Alger, Richard L. Berger, Darren L. Bleuel, David K. Bradley, Joseph A. Caggiano, Debra A. Callahan, Carlos Castro, Daniel T. Casey, Christine Choate, Daniel S. Clark, Charles J. Cerjan, Gilbert W. Collins, Eduard L. Dewald, Jean-Michel G. Di Nicola, Pascale Di Nicola, Laurent Divol, Shamasundar N. Dixit, Tilo Doeppner, Rebecca Dylla-Spears, Elizabeth G. Dzenitis, James E. Fair, Lars Johan Anders Frenje, M. Gatu Johnson, E. Giraldez, Vladimir Glebov, Steven M. Glenn, Steven W. Haan, Bruce A. Hammel, Stephen P. Hatchett, II, Christopher A. Haynam, Robert F. Heeter, Glenn M. Heestand, Hans W. Herrmann, Damien G. Hicks, Dean M. Holunga, Jeffrey B. Horner, Haibo Huang, Nobuhiko Izumi,

Ogden S. Jones, Daniel H. Kalantar, Joseph D. Kilkenny, Robert K. Kirkwood, John L. Kline, James P. Knauer, Bernard Kozioziemski, Andrea L. Kritcher, Jeremy J. Kroll, George A. Kyrala, Kai N. LaFortune, Otto L. Landen, Douglas W. Larson, Ramon J. Leeper, Sebastien Le Pape, John D. Lindl, Tammy Ma, Andrew J. Mackinnon, Andrew G. MacPhee, Evan Mapoles, Patrick W. McKenty, Nathan B. Meezan, Pierre Michel, Jose L. Milovich, John D. Moody, Alastair S. Moore, Mike Moran, Kari Ann Moreno, David H. Munro, Bryan R. Nathan, Abbas Nikroo, Richard E. Olson, Charles D. Orth, Arthur Pak, Pravesh K. Patel, Tom Parham, Richard Petrasso, Joseph E. Ralph, Hans Rinderknecht, Sean P. Regan, Harry F. Robey, J. Steven Ross, Jay D. Salmonson, Craig Sangster, Jim Sater, Marilyn B. Schneider, F. H. Seguin, Michael J. Shaw, Milton J. Shoup, Paul T. Springer, Wolfgang Stoeffl, Larry J. Suter, Cliff Avery Thomas, Richard P. J. Town, Curtis Walters, Stephen V. Weber, Paul J. Wegner, Clay Widmayer, Pamela K. Whitman, Klaus Widmann, Douglas C. Wilson, Bruno M. Van Wonterghem, Brian J. MacGowan, L. Jeff Atherton, and Edward I. Moses. First implosion experiments with cryogenic thermonuclear fuel on the National Ignition Facility. *Plasma Physics and Controlled Fusion*, 54(4), APR 2012. ISSN 0741-3335. doi: {10.1088/0741-3335/54/4/045013}.

B. A. Grierson, K. H. Burrell, W. W. Heidbrink, M. J. Lanctot, N. A. Pablant, and W. M. Solomon. Measurements of the deuterium ion toroidal rotation in the DIII-D tokamak and comparison to neoclassical theory. *Physics of Plasmas*, 19(5), MAY 2012. ISSN 1070-664X. doi: {10.1063/1.3694656}.

B.A. Grierson, K.H. Burrell, W.M. Solomon, R.V. Budny, and J. Candy. Collisionality scaling of main-ion toroidal and poloidal rotation in low torque diii-d plasmas. *Nuclear Fusion*, 53(6):063010, 2013. URL http://stacks.iop.org/0029-5515/53/i=6/a=063010.

Ö. D. Gürcan, P. H. Diamond, and T. S. Hahm. Turbulent equipartition and homogenization of plasma angular momentum. *Physical Review Letters*, 100:135001, APR 2008. doi: 10.1103/PhysRevLett.100.135001. URL http://link.aps.org/doi/10.1103/PhysRevLett.100.135001.

Ö. D. Gürcan, P. H. Diamond, T. S. Hahm, and R. Singh. Intrinsic rotation and electric field shear. *Physics of Plasmas*, 14(4), APR 2007. ISSN 1070-664X. doi: {10.1063/1.2717891}.

Ö. D. Gürcan, P. H. Diamond, P. Hennequin, C. J. McDevitt, X. Garbet, and C. Bourdelle. Residual parallel Reynolds stress due to turbulence intensity gradient in tokamak plasmas. *Physics of Plasmas*, 17(11), NOV 2010a. ISSN 1070-664X. doi: {10.1063/1.3503624}.

Ö. D. Gürcan, P. H. Diamond, C. J. McDevitt, and T. S. Hahm. A simple model of intrinsic rotation in high confinement regime tokamak plasmas. *Physics of Plasmas*, 17(3), MAR 2010b. ISSN 1070-664X. doi: {10.1063/1.3339909}.

T. S. Hahm, P. H. Diamond, O. D. Gurcan, and G. Rewoldt. Nonlinear gyrokinetic theory of toroidal momentum pinch. *Physics of Plasmas*, 14(7), JUL 2007. ISSN 1070-664X. doi: {10.1063/1.2743642}.

T.S. Hahm and K.H. Burrell. Flow shear-induced fluctuation suppression in finite aspect ratio shaped tokamak plasma. *Physics of Plasmas*, 2(5):1648–1651, May 1995. ISSN 1070-664X. doi: 10.1063/1.871313.

S. Hamada. Notes on magneto-hydridynamic equilibrium. *Progress of Theoretical Physics*, 22(1):145–146, 1959. ISSN 0033-068X. doi: {10.1143/PTP.22.145}.

D. R. Hatch, P. W. Terry, F. Jenko, F. Merz, and W. M. Nevins. Saturation of gyrokinetic turbulence through damped eigenmodes. *Physical Review Letters*, 106:115003, Mar 2011. doi: 10.1103/PhysRevLett.106.115003. URL http://link.aps.org/doi/10.1103/PhysRevLett.106.115003.

G.B. Haxel, J.B. Hedrick, and G.J. Orris. Rare earth elements critical resources for high technology, 2002. URL http://pubs.usgs.gov/fs/2002/fs087-02.

P. Hennequin. Fusion thermonucléaire controlée : une introduction. Cours de Master 2 Rayonnement et Energie, Physique des Plasmas, Université Paris-Sud Orsay, 2007.

P. Hennequin, R. Sabot, C. Honore, G.T. Hoang, X. Garbet, A. Truc, C. Fenzi, and A. Quemeneur. Scaling laws of density fluctuations at high-k on Tore Supra. *Plasma Physics and Controlled Fusion*, 46(12B, SI):B121–B133, DEC 2004. ISSN 0741-3335. doi: {10.1088/0741-3335/46/12B/011}. 31st European-Physical-Society Conference on Plasma Physics, London, ENGLAND, JUN 28-JUL 02, 2004.

P. Hennequin, L. Vermare, N. Fedorczak, J. Bernardo, Ö. D. Gürcan, E. Trier, N. Stuyck, C. Fenzi, J. Gunn, P. Monier-Garbet, C. Bourdelle, P. Ghendrih, and X. Garbet. The effect of SOL flows on edge and core radial electric field and rotation in Tore Supra. In *37th EPS Conference on Plasma Physics*, volume P1, page 1040. European Physical Society, JUN 2010.

C. Holland, J.E. Kinsey, J.C. DeBoo, K.H. Burrell, T.C. Luce, S.P. Smith, C.C. Petty, A.E. White, T.L. Rhodes, L. Schmitz, E.J. Doyle, J.C. Hillesheim, G.R. McKee, Z. Yan, G. Wang, L. Zeng, B.A. Grierson, A. Marinoni, P. Mantica, P.B. Snyder, R.E. Waltz, G.M. Staebler, and J. Candy. Validation Studies of Gyrofluid and Gyrokinetic Predictions of Transport and Turbulence Stiffness Using the DIII-d Tokamak. *Nuclear Fusion*, 53:083027 (11 pp.), Aug. 2013. ISSN 0029-5515.

W Horton. Drift waves and transport. *Reviews of Modern Physics*, 71(3):735–778, APR 1999. ISSN 0034-6861. doi: {10.1103/RevModPhys.71.735}.

F. Imbeaux. *Transport de courant et de chaleur dans les tokamaks : interprétation et prédiction des expériences par modélisation intégrée*. Habilitation à diriger des recherches, Association Euratom – CEA sur la fusion contrôlée, 2009.

F. Imbeaux, J.-F. Artaud, J. Kinsey, T.J.J. Tala, C. Bourdelle, T. Fujita, C. Greenfield, E. Joffrin, Y.S. Na, V.V. Parail, Y. Sakamoto, A.C.C. Sips, I. Voitsekovitch, ITPA Topical

Grp Transport Physics, and ITB Database Working Grp. Mint-machine transport analysis of hybrid discharges from the ITPA profile database. *Plasma Physics and Controlled Fusion*, 47(12B, SI):B179–B194, DEC 2005. ISSN 0741-3335. doi: {10.1088/0741-3335/47/12B/S14}. 32nd European-Physical-Society Conference on Plasma Physics, Tarragona, SPAIN, JUN 27-JUL 01, 2005.

IO. ITER, the world's largest Tokamak, August 2013. URL http://http://www.iter.org/mach.

IPP. Wendelstein 7-x, August 2013. URL http://http://www.ipp.mpg.de/ippcms/eng/pr/forschung/w7x/.

Physics Expert Group on Energetic Particles, Heating and Current Drive ITER and ITER Physics Basis Editors. Chapter 6: Plasma auxiliary heating and current drive. *Nuclear Fusion*, 39(12):2495, 1999. URL http://stacks.iop.org/0029-5515/39/i=12/a=306.

JET EFDA. Charge exchange spectroscopy, AUG 2013. URL http://http://www.efda.org/fusion/focus-on-jet-data/diagnostics/charge-exchange-spectroscopy/.

(prepared by F.G. Rimini) JET Team. DT fusion power production in ELM free H modes in JET. *Nuclear Fusion*, 39(11Y):1897, 1999. URL http://stacks.iop.org/0029-5515/39/i=11Y/a=332.

A. Kallenbach, H. M. Mayer, G. Fussmann, V. Mertens, U Stroth, O. Vollmer, and The ASDEX Team. Characterization of the angular momentum transport in asdex. *Plasma Physics and Controlled Fusion*, 33(6):595, 1991. URL http://stacks.iop.org/0741-3335/33/i=6/a=004.

S.M. Kaye, W. Solomon, R.E. Bell, B.P. LeBlanc, F. Levinton, J. Menard, G. Rewoldt, S. Sabbagh, W. Wang, and H. Yuh. Momentum transport in electron-dominated nstx spherical torus plasmas. *Nuclear Fusion*, 49(4):045010, 2009. URL http://stacks.iop.org/0029-5515/49/i=4/a=045010.

J. Kim, K. H. Burrell, P. Gohil, R. J. Groebner, Y.-B. Kim, H. E. St. John, R. P. Seraydarian, and M. R. Wade. Rotation characteristics of main ions and impurity ions in H-mode tokamak plasma. *Physical Review Letters*, 72:2199–2202, Apr 1994. doi: 10.1103/PhysRevLett.72.2199. URL http://link.aps.org/doi/10.1103/PhysRevLett.72.2199.

Y. B. Kim, P. H. Diamond, and R. J. Groebner. Neoclassical poloidal and toroidal rotation in tokamaks. *Physics of Fluids B: Plasma Physics*, 3(8):2050–2060, 1991. doi: 10.1063/1.859671. URL http://link.aip.org/link/?PFB/3/2050/1.

J.E. Kinsey, G.M. Staebler, and R.E. Waltz. The first transport code simulations using the trapped gyro-Landau-fluid model. *Physics of Plasmas*, 15:055908–1–14, May 2008. ISSN 1070-664X.

N. Kluy, C. Angioni, Y. Camenen, and A. G. Peeters. Linear gyrokinetic calculations of toroidal momentum transport in the presence of trapped electron modes in tokamak plasmas. *Physics of Plasmas*, 16(12):122302, 2009. doi: 10.1063/1.3271411. URL http://link.aip.org/link/?PHP/16/122302/1.

A.N. Kolmogorov. On the conservation of conditionnaly periodic motion under small perturbation of the Hamiltonian. *Doklady Akademii Nauk SSSR*, 98:527–530, 1954.

J.A. Krommes. Fundamental statistical descriptions of plasma turbulence in magnetic fields. *Physics Reports-Review section of Physics Letters*, 360(1-4):1–352, APR 2002. ISSN 0370-1573. doi: {10.1016/S0370-1573(01)00066-7}.

R. Kubo. Stochastic liouville equations. *Journal of Mathematical Physics*, 4(2):174–&, 1963. ISSN 0022-2488. doi: {10.1063/1.1703941}.

J.E LaBombard, B. and. Rice, A.E. Hubbard, J.W. Hughes, M. Greenwald, J. Irby, Y. Lin, B. Lipschultz, E.S. Marmar, C.S. Pitcher, N. Smick, S.M. Wolfe, S.J. Wukitch, and the Alcator Group. Transport-driven scrape-off-layer flows and the boundary conditions imposed at the magnetic separatrix in a tokamak plasma. *Nuclear Fusion*, 44(10):1047, 2004. URL http://stacks.iop.org/0029-5515/44/i=10/a=001.

L. Landau. On the vibrations of the electronic plasma. *Zhurnal Eksperimentalnoi i Teoreticheskoi Fisiki*, 16(7):574–586, 1946. ISSN 0044-4510.

X. Lapillonne, S. Brunner, T. Dannert, S. Jolliet, A. Marinoni, L. Villard, T. Goerler, F. Jenko, and F. Merz. Clarifications to the limitations of the s-alpha equilibrium model for gyrokinetic computations of turbulence. *Physics of Plasmas*, 16(3), Mar 2009. ISSN 1070-664X. doi: 10.1063/1.3096710.

W. D. Lee, J. E. Rice, E. S. Marmar, M. J. Greenwald, I. H. Hutchinson, and J. A. Snipes. Observation of anomalous momentum transport in tokamak plasmas with no momentum input. *Physical Review Letters*, 91:205003, Nov 2003. doi: 10.1103/PhysRevLett.91.205003. URL http://link.aps.org/doi/10.1103/PhysRevLett.91.205003.

R.G. Littlejohn. Hamiltonian-formulation of guiding center motion. *Physics of Fluids*, 24 (9):1730–1749, 1981. ISSN 1070-6631. doi: 10.1063/1.863594.

Robert E. Jr Lucas. *Lectures on Economic Growth*. Harvard University Press, 2004. ISBN 978-0-674-01601-9.

N. Mattor and P.H. Diamond. Momentum and thermal transport in neutral-beam-heated tokamaks. *Physics of Fluids*, 31(5):1180–1189, May 1988. ISSN 1070-6631. doi: 10.1063/1.866747.

G.R. McKee, C.C. Petty, R.E. Waltz, C. Fenzi, R.J. Fonck, J.E. Kinsey, T.C. Luce, K.H. Burrell, D.R. Baker, E.J. Doyle, X. Garbet, R.A. Moyer, C.L. Rettig, T.L. Rhodes, D.W. Ross, G.M. Staebler, R. Sydora, and M.R. Wade. Non-dimensional scaling of turbulence

characteristics and turbulent diffusivity. *Nuclear Fusion*, 41(9):1235–1242, SEP 2001. ISSN 0029-5515. doi: {10.1088/0029-5515/41/9/312}.

N.D. Mermin. Thermal Properties of Inhomogeneous electron gas. *Physical Review*, 137 (5A):1441–&, 1965. ISSN 0031-899X.

F. Merz and F. Jenko. Nonlinear interplay of TEM and ITG turbulence and its effect on transport. *Nuclear Fusion*, 50(5, SI), MAY 2010. ISSN 0029-5515. doi: {10.1088/0029-5515/50/5/054005}. 4th IAEA Technical Meeting on the Theory of Plasma Instabilities, Kyoto, JAPAN, MAY 18-20, 2009.

R.L. Miller and R.E. Waltz. On the nature of rotational shear stabilization in toroidal geometry and its numerical representation. *Physics of Plasmas*, 1(9):2835–2842, SEP 1994. ISSN 1070-664X. doi: {10.1063/1.870522}.

Richard Monastersky. Global carbon dioxide levels near worrisome milestone. *Nature*, 497 (7447):13–14, MAY 2 2013. ISSN 0028-0836.

Ph. Moreau, F. Clairet, J. M. Chareau, M. Paume, and C. Laviron. Ultrafast frequency sweep heterodyne reflectometer on the Tore Supra tokamak. *Review of Scientific Instruments*, 71(1):74–81, 2000. doi: 10.1063/1.1150164. URL http://link.aip.org/link/?RSI/71/74/1.

Jürgen Moser. On invariant curves of area-preserving mappings of an annulus. *Nachrichten der Akademie der Wissenschaften in Göttingen. II. Mathematische-Physikalische Klasse*, 1962.

K. Nagashima, Y. Koide, and H. Shirai. Experimental determination of non-diffusive toroidal momentum flux in jt-60u. *Nuclear Fusion*, 34(3):449, 1994. URL http://stacks.iop.org/0029-5515/34/i=3/a=I12.

National Oceanic & Atmospheric Administration, Global Monitoring Division. Time history of atmospheric carbon dioxide from 800,000 years ago until january, 2012, JUL 2013. URL http://www.esrl.noaa.gov/gmd/ccgg/trends/history.html.

W.M. Nevins. A review of confinement requirements for advanced fuels. *Journal of Fusion Energy*, 17(1):25–32, MAR 1998. ISSN 0164-0313. doi: {10.1023/A:1022513215080}.

S. L. Newton, S. C. Cowley, and N. F. Loureiro. Understanding the effect of sheared flow on microinstabilities. *Plasma Physics and Controlled Fusion*, 52(12, 1), DEC 2010. ISSN 0741-3335. doi: {10.1088/0741-3335/52/12/125001}.

S.A. Orszag and R.H. Kraichna. Model equations for strong turbulence in a vlasov plasma. *Physics of Fluids*, 10(8):1720–&, 1967. ISSN 1070-6631. doi: {10.1063/1.1762351}.

A. G. Peeters, C. Angioni, and D. Strintzi. Toroidal momentum pinch velocity due to the coriolis drift effect on small scale instabilities in a toroidal plasma. *Physical Review*

Letters, 98:265003, Jun 2007. doi: 10.1103/PhysRevLett.98.265003. URL http://link.aps.org/doi/10.1103/PhysRevLett.98.265003.

A. G. Peeters, C. Angioni, Y. Camenen, F. J. Casson, W. A. Hornsby, A. P. Snodin, and D. Strintzi. The influence of the self-consistent mode structure on the coriolis pinch effect. *Physics of Plasmas*, 16(6), Jun 2009a. ISSN 1070-664X. doi: 10.1063/1.3124133.

A. G. Peeters, Y. Camenen, F. J. Casson, W. A. Hornsby, A. P. Snodin, D. Strintzi, and G. Szepesi. The nonlinear gyro-kinetic flux tube code GKW. *Computer Physics Communications*, 180(12):2650–2672, Dec 2009b. ISSN 0010-4655. doi: 10.1016/j.cpc.2009.07.001.

A. G. Peeters, C. Angioni, A. Bortolon, Y. Camenen, F. J. Casson, B. Duval, L. Fiederspiel, W. A. Hornsby, Y. Idomura, T. Hein, N. Kluy, P. Mantica, F. I. Parra, A. P. Snodin, G. Szepesi, D. Strintzi, T. Tala, G. Tardini, P. de Vries, and J. Weiland. Overview of toroidal momentum transport. *Nuclear Fusion*, 51(9, SI), Sep 2011. ISSN 0029-5515. doi: 10.1088/0029-5515/51/9/094027.

A.G. Peeters and C. Angioni. Linear gyrokinetic calculations of toroidal momentum transport in a tokamak due to the ion temperature gradient mode. *Physics of Plasmas*, 12(7), Jul 2005. ISSN 1070-664X. doi: 10.1063/1.1949608.

Arthur G. Peeters, Clemente Angioni, and Giovanni Tardini. Transport modelling. *Comptes Rendus Physique*, 7(6):592 – 605, 2006. ISSN 1631-0705. doi: {http://dx.doi.org/10.1016/j.crhy.2006.07.01}. URL http://www.sciencedirect.com/science/article/pii/S1631070506001575.

F. Pegoraro and T.J. Schep. Low-frequency modes with high toroidal mode numbers - a general formulation. *Physics of Fluids*, 24(3):478–497, 1981. ISSN 1070-6631. doi: 10.1063/1.863395.

M. J. Pueschel. *Electromagnetic Effects in Gyrokinetic Simulations of Plasma Turbulence*. PhD thesis, Westfälischen Wilhelms-Universität Münster, 2009.

C. Reux. *Etude d'une méthode d'amortissement des disruptions d'un plasma de tokamak*. PhD thesis, Ecole doctorale de l'Ecole Polytechnique, 2010.

J. E. Rice, A. Ince-Cushman, J. S. deGrassie, L. G. Eriksson, Y. Sakamoto, A. Scarabosio, A. Bortolon, K. H. Burrell, B. P. Duval, C. Fenzi-Bonizec, M. J. Greenwald, R. J. Groebner, G. T. Hoang, Y. Koide, E. S. Marmar, A. Pochelon, and Y. Podpaly. Inter-machine comparison of intrinsic toroidal rotation in tokamaks. *Nuclear Fusion*, 47(11):1618–1624, NOV 2007. ISSN 0029-5515. doi: {10.1088/0029-5515/47/11/025}.

J.E. Rice, W.D. Lee, E.S. Marmar, N.P. Basse, P.T. Bonoli, M.J. Greenwald, A.E. Hubbard, J.W. Hughes, I.H. Hutchinson, A. Ince-Cushman, J.H. Irby, Y. Lin, D. Mossessian, J.A. Snipes, S.M. Wolfe, S.J. Wukitch, and K. Zhurovich. Toroidal rotation and momentum transport in alcator c-mod plasmas with no momentum input. *Physics of Plasmas*, 11(5):

2427–2432, May 2004. ISSN 1070-664X. doi: 10.1063/1.1646157. 45th Annual Meeting of the Division of Plasma Physics of the American-Physical-Society, Albuquerque, Nm, Nov, 2003.

T.H. Rider. Fundamental limitations on plasma fusion systems not in thermodynamic equilibrium. *Physics of Plasmas*, 4(4):1039–1046, APR 1997. ISSN 1070-664X. doi: {10.1063/1.872556}.

C. M. Roach, I. G. Abel, R. J. Akers, W. Arter, M. Barnes, Y. Camenen, F. J. Casson, G. Colyer, J. W. Connor, S. C. Cowley, D. Dickinson, W. Dorland, A. R. Field, W. Guttenfelder, G. W. Hammett, R. J. Hastie, E. Highcock, N. F. Loureiro, A. G. Peeters, M. Reshko, S. Saarelma, A. A. Schekochihin, M. Valovic, and H. R. Wilson. Gyrokinetic simulations of spherical tokamaks. *Plasma Physics And Controlled Fusion*, 51(12), Dec 2009. ISSN 0741-3335. doi: 10.1088/0741-3335/51/12/124020. 36th European-Physical-Society Conference on Plasma Physics, Natl Palace Culture, Sofia, Bulgaria, Jun 29-Jul 03, 2009.

F. Romanelli, P. Barabaschi, D. Borba, G. Federici, L. Horton, R. Neu, D. Strok, and H. Zohm. Fusion electricity, a roadmap to the realisation of fusion energy. Technical report, EFDA, November 2012. URL http://www.efda.org/2013/01/bringing-fusion-electricity-to-the-grid/.

M. Romanelli, G. Regnoli, and C. Bourdelle. Numerical study of linear dissipative drift electrostatic modes in tokamaks. *Physics of Plasmas*, 14(8), Aug 2007. ISSN 1070-664X. doi: 10.1063/1.2755981.

R. Sabot, A. Sirinelli, J. M. Chareau, and J. C. Giaccalone. A dual source D-band reflectometer for density profile and fluctuations measurements in Tore-Supra. *Nuclear Fusion*, 46(9):S685–S692, SEP 2006. ISSN 0029-5515. doi: {10.1088/0029-5515/46/9/S04}. 7th International Reflectometry Workshop for Fusion Plasma Diagnostics (IRW7), Max Plank Inst Plasmaphys, Garching, GERMANY, MAY 09-12, 2005.

B. Saoutic, J. Abiteboul, L. Allegretti, S. Allfrey, J.M. Ané, T. Aniel, A. Argouarch, J.F. Artaud, M.H. Aumenier, S. Balme, V. Basiuk, O. Baulaigue, P. Bayetti, A. Bécoulet, M. BÃľcoulet, M.S. Benkadda, F. Benoit, G. Berger-by, J.M. Bernard, B. Bertrand, P. Beyer, A. Bigand, J. Blum, D. Boilson, G. Bonhomme, H. Bottollier-Curtet, C. Bouchand, F. Bouquey, C. Bourdelle, S. Bourmaud, C. Brault, S. BrÃľmond, C. Brosset, J. Bucalossi, Y. Buravand, P. Cara, V. Catherine-Dumont, A. Casati, M. Chantant, M. Chatelier, G. Chevet, D. Ciazynski, G. Ciraolo, F. Clairet, M. Coatanea-Gouachet, L. Colas, L. Commin, E. Corbel, Y. Corre, X. Courtois, R. Dachicourt, M. Dapena Febrer, M. Davi Joanny, R. Daviot, H. De Esch, J. Decker, P. Decool, P. Delaporte, E. Delchambre, E. Delmas, L. Delpech, C. Desgranges, P. Devynck, T. Dittmar, L. Doceul, D. Douai, H. Dougnac, J.L. Duchateau, B. Dugué, N. Dumas, R. Dumont, A. Durocher, F.X. Duthoit, A. Ekedahl, D. Elbeze, M. El Khaldi, F. Escourbiac, F. Faisse, G. Falchetto, M. Farge, J.L. Farjon,

M. Faury, N. Fedorczak, C. Fenzi-Bonizec, M. Firdaouss, Y. Frauel, X. Garbet, J. Garcia, J.L. Gardarein, L. Gargiulo, P. Garibaldi, E. Gauthier, O. Gaye, A. Géraud, M. Geynet, P. Ghendrih, I. Giacalone, S. Gibert, C. Gil, G. Giruzzi, M. Goniche, V. Grandgirard, C. Grisolia, G. Gros, A. Grosman, R. Guigon, D. Guilhem, B. Guillerminet, R. Guirlet, J. Gunn, O. Gurcan, S. Hacquin, J.C. Hatchressian, P. Hennequin, C. Hernandez, P. Hertout, S. Heuraux, J. Hillairet, G.T. Hoang, C. Honore, M. Houry, T. Hutter, P. Huynh, G. Huysmans, F. Imbeaux, E. Joffrin, J. Johner, L. Jourd'Heuil, Y.S. Katharria, D. Keller, S.H. Kim, M. Kocan, M. Kubic, B. Lacroix, V. Lamaison, G. Latu, Y. Lausenaz, C. Laviron, F. Leroux, L. Letellier, M. Lipa, X. Litaudon, T. Loarer, P. Lotte, S. Madeleine, P. Magaud, P. Maget, R. Magne, L. Manenc, Y. Marandet, G. Marbach, J.L. Maréchal, L. Marfisi, C. Martin, G. Martin, V. Martin, A. Martinez, J.P. Martins, R. Masset, D. Mazon, N. Mellet, L. Mercadier, A. Merle, D. Meshcheriakov, O. Meyer, L. Million, M. Missirlian, P. Mollard, V. Moncada, P. Monier-Garbet, D. Moreau, P. Moreau, L. Morini, M. Nannini, M. Naiim Habib, E. Nardon, H. Nehme, C. Nguyen, S. Nicollet, R. Nouilletas, T. Ohsako, M. Ottaviani, S. Pamela, H. Parrat, P. Pastor, A.L. Pecquet, B. Pégourié, Y. Peysson, I. Porchy, C. Portafaix, M. Preynas, M. Prou, J.M. Raharijaona, N. Ravenel, C. Reux, P. Reynaud, M. Richou, H. Roche, P. Roubin, R. Sabot, F. Saint-Laurent, S. Salasca, F. Samaille, A. Santagiustina, Y. Sarazin, A. Semerok, J. Schlosser, M. Schneider, M. Schubert, F. Schwander, J.L. Ségui, G. Selig, P. Sharma, J. Signoret, A. Simonin, S. Song, E. Sonnendruker, F. Sourbier, P. Spuig, P. Tamain, M. Tena, J.M. Theis, D. Thouvenin, A. Torre, J.M. Travère, E. Tsitrone, J.C. Vallet, E. Van Der Plas, A. Vatry, J.M. Verger, L. Vermare, F. Villecroze, D. Villegas, R. Volpe, K. Vulliez, J. Wagrez, T. Wauters, L. Zani, D. Zarzoso, and X.L. Zou. Contribution of tore supra in preparation of iter. *Nuclear Fusion*, 51(9):094014, 2011. URL http://stacks.iop.org/0029-5515/51/i=9/a=094014.

Y. Sarazin. Turbulence, Transport and Heating. Cours de Master 2 Sciences de la Fusion, FCM, 2008.

S.D. Scott, P.H. Diamond, R.J. Fonck, R.J. Goldston, R.B. Howell, K.P. Jaehnig, G. Schilling, E.J. Synakowski, M.C. Zarnstorff, C.E. Bush, E. Fredrickson, K.W. Hill, A.C. Janos, D.K. Mansfield, D.K. Owens, H. Park, G. Pautasso, A.T. Ramsey, J. Schivell, G.D. Tait, W.M. Tang, and G. Taylor. Local measurements of correlated momentum and heat-transport in the TFTR tokamak. *Physical Review Letters*, 64(5):531–534, Jan 29 1990. ISSN 0031-9007. doi: 10.1103/PhysRevLett.64.531.

P.B. Snyder and G.W. Hammett. Electromagnetic effects on plasma microturbulence and transport. *Physics of Plasmas*, 8(3), MAR 2001.

W. M. Solomon, K. H. Burrell, A. M. Garofalo, S. M. Kaye, R. E. Bell, A. J. Cole, J. S. deGrassie, P. H. Diamond, T. S. Hahm, G. L. Jackson, M. J. Lanctot, C. C. Petty, H. Reimerdes, S. A. Sabbagh, E. J. Strait, T. Tala, and R. E. Waltz. Mechanisms for generating toroidal rotation in tokamaks without external momentum input. *Physics*

of Plasmas, 17(5):056108, 2010. doi: 10.1063/1.3328521. URL http://link.aip.org/link/?PHP/17/056108/1.

W. M. Solomon, K. H. Burrell, J. S. deGrassie, R. Budny, R. J. Groebner, J. E. Kinsey, G. J. Kramer, T. C. Luce, M. A. Makowski, D. Mikkelsen, R. Nazikian, C. C. Petty, P. A. Politzer, S. D. Scott, M. A. Van Zeeland, and M. C. Zarnstorff. Momentum confinement at low torque. *Plasma Physics and Controlled Fusion*, 49(12B):B313–B324, DEC 2007. ISSN 0741-3335. doi: {10.1088/0741-3335/49/12B/S29}. 34th European-Physical-Society Conference on Plasma Physics, Palace Culture & Sci, Warsaw, POLAND, JUL 02-06, 2007.

W.M. Solomon, K.H. Burrell, A.M. Garofalo, A.J. Cole, R.V. Budny, J.S. deGrassie, W.W. Heidbrink, G.L. Jackson, M.J. Lanctot, R. Nazikian, H. Reimerdes, E.J. Strait, M.A. Van Zeeland, and the DIII-D Rotation Physics Task Force. Advances in understanding the generation and evolution of the toroidal rotation profile on diii-d. *Nuclear Fusion*, 49 (8):085005, 2009. URL http://stacks.iop.org/0029-5515/49/i=8/a=085005.

S. Son and N.J. Fisch. Aneutronic fusion in a degenerate plasma. *Physics Letters A*, 329 (1-2):76–82, AUG 16 2004. ISSN 0375-9601. doi: {10.1016/j.phys;eta.2004.06.054}.

G. M. Staebler, R. E. Waltz, J. Candy, and J. E. Kinsey. New paradigm for suppression of gyrokinetic turbulence by velocity shear. *Physical Review Letters*, 110(5), Jan 30 2013. ISSN 0031-9007. doi: 10.1103/PhysRevLett.110.055003.

G.M. Staebler, J.E. Kinsey, and R.E. Waltz. Gyro-Landau fluid equations for trapped and passing particles. *Physics of Plasmas*, 12(10), OCT 2005. ISSN 1070-664X. doi: {10.1063/1.2044587}.

G.M. Staebler, L.L. Lao, B.A. Grierson, C. Chrystal, and J.E. Kinsey. Predicting Internal Transport Barriers with the TGLF model. In *40th EPS Conference on Plasma Physics*, volume O4, page 105. European Physical Society, JUL 2013.

S. Suckewer, H.P. Eubank, R.J. Goldston, J. McEnerney, N.R. Sauthoff, and H.H. Towner. Toroidal plasma rotation in the plt tokamak with neutral-beam injection. *Nuclear Fusion*, 21(10):1301, 1981. URL http://stacks.iop.org/0029-5515/21/i=10/a=009.

T. Tala, K. Crombé, P.C. de Vries, J. Ferreira, P. Mantica, A.G. Peeters, Y. Andrew, R. Budny, G. Corrigan, A. Eriksson, X. Garbet, C. Giroud, M.-D. Hua, H. Nordman, V. Naulin, M.F.F. Nave, V. Parail, K. Rantamäki, B. D. Scott, P. Strand, G. Tardini, A. Thyagaraja, J. Weiland, K.-D. Zastrow, and JET-EFDA Contributors. Toroidal and poloidal momentum transport studies in tokamaks. *Plasma Physics and Controlled Fusion*, 49(12B):B291, 2007. URL http://stacks.iop.org/0741-3335/49/i=12B/a=S27.

T. Tala, K.-D. Zastrow, J. Ferreira, P. Mantica, V. Naulin, A. G. Peeters, G. Tardini, M. Brix, G. Corrigan, C. Giroud, and D. Strintzi. Evidence of inward toroidal momentum convection in the JET tokamak. *Physical Review Letters*, 102:075001, Feb

2009. doi: 10.1103/PhysRevLett.102.075001. URL http://link.aps.org/doi/10.1103/PhysRevLett.102.075001.

T. Tala, A. Salmi, C. Angioni, F. J. Casson, G. Corrigan, J. Ferreira, C. Giroud, P. Mantica, V. Naulin, A. G. Peeters, W. M. Solomon, D. Strintzi, M. Tsalas, T. W. Versloot, P. C. de Vries, K. D. Zastrow, and JET-EFDA Contributors. Parametric dependences of momentum pinch and Prandtl number in JET. *Nuclear Fusion*, 51(12), Dec 2011. doi: 10.1088/0029-5515/51/12/123002.

T. Tala, I. Imbeaux, V.V. Parail, C. Bourdelle, G. Corrigan, X. Garbet, D.J. Heading, X. Litaudon, P.L. Strand, J. Weiland, and JET-EFDA Contributors. Fully predictive time-dependent transport simulations of ITB plasmas in JET, JT-60U and DIII-D. *Nuclear Fusion*, 46(5):548–561, MAY 2006. ISSN 0029-5515. doi: {10.1088/0029-5515/46/5/007}.

Teller, E. Peaceful Uses of Fusion. In *Proceedings of the Second International United Nations Conference on the Peaceful Uses of Atomic Energy*, volume 31, page 2410, Geneva, 1958. United Nations.

A. Truc, A. Quemeneur, P. Hennequin, D. Gresillon, F. Gervais, C. Laviron, J. Olivain, S.K. Saha, and P. Devynck. ALTAIR - An infrared-LASER scattering diagnostic on the Tore-Supra tokamak. *Review of Scientific Instruments*, 63(7):3716–3724, JUL 1992. ISSN 0034-6748. doi: {10.1063/1.1143603}.

D. van Houtte, G. Martin, A. Bécoulet, J. Bucalossi, G. Giruzzi, G.T. Hoang, Th. Loarer, B. Saoutic, and the Tore Supra Team. Recent fully non-inductive operation results in Tore Supra with 6 min, 1 GJ plasma discharges. *Nuclear Fusion*, 44(5):L11, 2004. URL http://stacks.iop.org/0029-5515/44/i=5/a=L01.

A. A. Vedenov, E. P. Velikhov, and R. Z. Sadgeev. Quasi-linear theory of plasma oscillations. *Nuclear Fusion*, (2):465–475, 1962. ISSN 0029-5515.

L. Vermare, Ö.D. Gürcan, P. Hennequin, C. Honoré, X. Garbet, J.C. Giacalone, R. Sabot, and F. Clairet. Wavenumber spectrum of micro-turbulence in tokamak plasmas. *Comptes Rendus Physique*, 12(2):115 – 122, 2011. ISSN 1631-0705. doi: {http://dx.doi.org/10.1016/j.crhy.2010.11.003}. URL http://www.sciencedirect.com/science/article/pii/S1631070510001556.

E. Viezzer, T. Putterich, R. Dux, R. M. McDermott, and the ASDEX Upgrade Team. High-resolution charge exchange measurements at asdex upgrade. *Review of Scientific Instruments*, 83(10):103501, 2012. doi: 10.1063/1.4755810. URL http://link.aip.org/link/?RSI/83/103501/1.

E. Viezzer, T. Pütterich, G.D. Conway, R. Dux, T. Happel, J.C. Fuchs, R.M. McDermott, F. Ryter, B. Sieglin, W. Suttrop, M. Willensdorfer, E. Wolfrum, and the ASDEX Upgrade Team. High-accuracy characterization of the edge radial electric field at asdex upgrade. *Nuclear Fusion*, 53(5):053005, 2013. URL http://stacks.iop.org/0029-5515/53/i=5/a=053005.

D. Villegas, R. Guirlet, C. Bourdelle, G. T. Hoang, X. Garbet, and R. Sabot. Experimental Electron Temperature Gradient Dependence of Heavy Impurity Transport in Fusion Devices. *PHYSICAL REVIEW LETTERS*, 105(3), JUL 13 2010. ISSN 0031-9007. doi: {10.1103/PhysRevLett.105.035002}.

M.G. von Hellermann, G. Bertschinger, W. Biel, C. Giroud, R. Jaspers, C. Jupen, O. Marchuk, M. O'Mullane, H.P. Summers, A. Whiteford, and K.-D. Zastrow. Complex spectra in fusion plasmas. *Physica Scripta*, 2005(T120):19, 2005. URL http://stacks.iop.org/1402-4896/2005/i=T120/a=003.

R. E. Waltz, G. M. Staebler, W. Dorland, G. W. Hammett, M. Kotschenreuther, and J. A. Konings. A gyro-Landau-fluid transport model. *Physics of Plasmas*, 4(7):2482–2496, JUL 1997. ISSN 1070-664X. doi: {10.1063/1.872228}.

R.E. Waltz, G.D. Kerbel, and J. Milovich. Toroidal gyro-landau fluid model turbulence simulations in a nonlinear ballooning mode representation with radial modes. *Physics of Plasmas*, 1(7):2229–2244, Jul 1994. ISSN 1070-664X. doi: 10.1063/1.870934.

R.E. Waltz, R.L. Dewar, and X. Garbet. Theory and simulation of rotational shear stabilization of turbulence. *Physics of Plasmas*, 5(5, Part 2, SI):1784–1792, May 1998. ISSN 1070-664X. doi: 10.1063/1.872847. 39th Annual Meeting of the Division-of-Plasma-Physics of the American-Physical-Society, Pittsburgh, Pennsylvania, Nov 17-21, 1997.

Baonian Wan and International Collaborators. Recent experiments in the east and ht-7 superconducting tokamaks. *Nuclear Fusion*, 49(10):104011, 2009. URL http://stacks.iop.org/0029-5515/49/i=10/a=104011.

J. Weiland, A.B. Jarmen, and H. Nordman. Diffusive particle and heat pinch effects in toroidal plasmas. *Nuclear Fusion*, 29(10):1810–1814, OCT 1989. ISSN 0029-5515. doi: {10.1088/0029-5515/29/10/015}.

H. Weisen, M. von Hellermann, A. Boileau, L.D. Horton, W. Mandl, and H.P. Summers. Charge exchange spectroscopy measurements of ion temperature and toroidal rotation in jet. *Nuclear Fusion*, 29(12):2187, 1989. URL http://stacks.iop.org/0029-5515/29/i=12/a=011.

H. Weisen, Y. Camenen, A. Salmi, T. W. Versloot, P. C. deVries, M. Maslov, T. Tala, M. Beurskens, C. Giroud, and JET-EFDA Contributors. Ubiquity of non-diffusive momentum transport in JET H-modes. *Nuclear Fusion*, 52(11, SI), NOV 2012. ISSN 0029-5515. doi: {10.1088/0029-5515/52/11/114024}. 13th International Workshop on H-Mode Physics and Transport Barriers, Lady Margaret Hall Coll, Oxford, ENGLAND, OCT, 2011.

Wesson, J. *Tokamaks*. Oxford University Press, second edition, 1997.

Z. Yan, M. Xu, P. H. Diamond, C. Holland, S. H. Müller, G. R. Tynan, and J. H. Yu. Intrinsic rotation from a residual stress at the boundary of a cylindrical laboratory plasma. *Physical Review Letters*, 104:065002, Feb 2010. doi: 10.1103/PhysRevLett.104.065002. URL http://link.aps.org/doi/10.1103/PhysRevLett.104.065002.

M. Yoshida, Y. Koide, H. Takenaga, H. Urano, N. Oyama, K. Kamiya, Y. Sakamoto, G. Matsunaga, Y. Kamada, and the JT-60 Team. Momentum transport and plasma rotation profile in toroidal direction in jt-60u l-mode plasmas. *Nuclear Fusion*, 47(8):856, 2007. URL http://stacks.iop.org/0029-5515/47/i=8/a=017.

Résumé

Le confinement magnétique dans les tokamaks est à l'heure actuelle la voie la plus avancée pour produire de l'énergie par fusion thermonucléaire. Des études théoriques et expérimentales ont montré que la génération de rotation permet d'en augmenter les performances par la réduction du transport turbulent à l'IJuvre dans les plasmas de tokamaks. L'influence de la rotation sur les flux turbulents de chaleur et de particules ainsi que le transport du moment angulaire sont étudiés par simulation numérique dans le cadre du code gyro-cinétique, quasi-linéaire QuaLiKiz. A cette occasion, le code QuaLiKiz est modifié pour prendre en compte la rotation du plasma et calculer le flux de moment angulaire. Il est montré que le cadre de travail de QuaLiKiz permet de calculer le flux de moment angulaire y compris le stress résiduel induit par le cisaillement du champ électrique radial ainsi que l'effet de la rotation sur les flux de chaleur et de particules. Les approximations majeures du formalisme utilisé, en particulier la représentation de ballonnement à son ordre le plus bas et l'utilisation de fonctions propres analytiques calculées dans la limite hydrodynamiques, sont analysées en détail et leur validité vérifiée. La construction des flux quasi-linéaires est ensuite détaillée et le flux quasi-linéaire de moment angulaire dérivé. Les différentes contributions au flux turbulent de moment angulaire sont étudiées et comparées avec succès à la fois aux données de simulations gyro-cinétiques non-linéaires ainsi qu'aux données expérimentales.

Summary

The magnetic confinement in tokamaks is for now the most advanced way towards energy production by nuclear fusion. Both theoretical and experimental studies showed that rotation generation can increase its performance by reducing the turbulent transport in tokamak plasmas. The rotation influence on the heat and particle fluxes is studied along with the angular momentum transport with the quasi-linear gyro-kinetic eigenvalue code QuaLiKiz. For this purpose, the QuaLiKiz code is modified in order to take the plasma rotation into account and compute the angular momentum flux. It is shown that QuaLiKiz framework is able to correctly predict the angular momentum flux including the $\mathbf{E} \times \mathbf{B}$ shear induced residual stress as well as the influence of rotation on the heat and particle fluxes. The major approximations of QuaLiKiz formalisms are reviewed, in particular the ballooning representation at its lowest order and the eigenfunctions calculated in the hydrodynamic limit. The construction of the quasi-linear fluxes is also reviewed in details and the quasi-linear angular momentum flux is derived. The different contributions to the turbulent momentum flux are studied and successfully compared both against non-linear gyro-kinetic simulations and experimental data.